

DEVELOPMENT OF ADVANCED OPTICS AND HIGH RESOLUTION
INSTRUMENTATION FOR MASS SPECTROMETRY BASED PROTEOMICS

A Dissertation

by

STACY DAWN SHERROD

Submitted to the Office of Graduate Studies of
Texas A&M University
in partial fulfillment of the requirements for the degree of

DOCTOR OF PHILOSOPHY

December 2008

Major Subject: Chemistry

DEVELOPMENT OF ADVANCED OPTICS AND HIGH RESOLUTION
INSTRUMENTATION FOR MASS SPECTROMETRY BASED PROTEOMICS

A Dissertation

by

STACY DAWN SHERROD

Submitted to the Office of Graduate Studies of
Texas A&M University
in partial fulfillment of the requirements for the degree of

DOCTOR OF PHILOSOPHY

Approved by:

Chair of Committee,	David H. Russell
Committee Members,	Emile A. Schweikert
	Robert Burghardt
	Gyula Vigh
Head of Department,	David H. Russell

December 2008

Major Subject: Chemistry

ABSTRACT

Development of Advanced Optics and High Resolution Instrumentation for Mass Spectrometry Based Proteomics. (December 2008)

Stacy Dawn Sherrod, B.S., Sam Houston State University

Chair of Advisory Committee: Dr. David H. Russell

Imaging mass spectrometry (MS) analysis allows scientists the ability to obtain spatial and chemical information of analytes on a wide variety of surfaces. The ability to image biological analytes is an important tool in many areas of life science research, including: the ability to map pharmaceutical drugs in targeted tissue, to spatially determine the expression profile of specific proteins in healthy vs. diseased tissue states, and to rapidly interrogate biomolecular microarrays. However, there are several avenues for improving the imaging MS experiment for biological samples. Three significant directions this work addresses include: (1) reducing chemical noise and increasing analyte identification by developing sample preparation methodologies, (2) improving the analytical figures of merit (*i.e.*, spatial resolution, analysis time) by implementing a spatially dynamic optical system, and (3) increasing both mass spectral resolution and ion detection sensitivity by modifying a commercial time-of-flight (TOF) MS.

Firstly, sample methodology schemes presented in these studies consist of obtaining both “top-down” and “bottom-up” information. In that, both intact mass and peptide mass fingerprinting data can be obtained to increase protein identification. This

sample methodology was optimized on protein microarrays in preparation for bio tissue analysis. Other work consists of optimizing novel sample preparation strategies for hydrated solid-supported lipid bilayer studies. Sample methods incorporating nanomaterials for laser desorption/ionization illustrate the ability to perform selective ionization of specific analytes. Specifically, our results suggest that silver nanoparticles facilitate the selective ionization of olefin containing species (*e.g.*, steroids, vitamins).

Secondly, an advanced optical design incorporating a spatially dynamic optical scheme allows for laser beam expansion, homogenization, collimation, shaping, and imaging. This spatially dynamic optical system allows user defined beam shapes, decreases analysis times associated with mechanical movement of the sample stage, and is capable of increasing the MS limits of detection by simultaneously irradiating multiple spots.

Lastly, new data acquisition strategies (multiple anode detection schemes) were incorporated into a commercial time-of-flight mass spectrometer to increase both sensitivity and resolution in a matrix assisted laser desorption/ionization mass spectrometer. The utility of this technique can be applied to many different samples, where high mass spectral resolution allows for increased mass measurement accuracy.

DEDICATION

This dissertation is dedicated to my family, David and Stephanie Sherrod and Nicholas and Krystal Castle, for their love, discipline, and steadfast encouragement in the pursuit of my education.

“I have fought the good fight, I have finished the race, I have kept the faith.”

2 Timothy 4:7

ACKNOWLEDGEMENTS

I would like to thank Dr. David H. Russell for providing me the opportunity to discover the beauty of scientific research. Not only did he allow me to explore my own research interests and encourage independent thinking, he also offered me many opportunities to attend and present my research at several conferences.

I would like to thank the members of the Russell Research Group both past and present for their friendship and scientific criticism. I would especially like to acknowledge Dr. John McLean for being a great mentor during my first three years of graduate school at Texas A&M University. I would also like to thank Mr. Greg Matthijetz for teaching me a little bit about electronics, but more importantly, fixing all the things that I accidentally broke in the laboratory. I would like to thank Ms. Stephanie Cologna for being an honest friend and always willing to engage in scientific conversation.

I am very grateful to Mr. Jody May who has been a great support in my life for the past five years. His patience and outlook on life have taught me “more than he will ever know”.

And last but not least I would like to thank my high school chemistry teacher, Mary Yarbray. She taught me basic principles of chemistry and encouraged me to pursue an advanced education in science.

TABLE OF CONTENTS

	Page
ABSTRACT	iii
DEDICATION	v
ACKNOWLEDGEMENTS	vi
TABLE OF CONTENTS	vii
LIST OF FIGURES	x
LIST OF TABLES	xiii
CHAPTER	
I INTRODUCTION: IMAGING MASS SPECTROMETRY	1
Sample Preparation for Imaging Mass Spectrometry	5
Analyte Identification in Imaging Mass Spectrometry	7
Spatial Resolution in Imaging Mass Spectrometry	10
II EXPERIMENTAL	15
Instrumental Apparatus	15
Data Validation	17
Traditional Mass Spectrometry Sample Preparation	18
Imaging Mass Spectrometry Sample Preparation	19
III IMAGING MASS SPECTROMETRY: A SIMULTANEOUS TOP DOWN/ BOTTOM UP APPROACH	21
Introduction	21
Bottom-Up Mass Spectrometry	24
Top-Down Mass Spectrometry	29
Conclusion	32

CHAPTER		Page
IV	SPATIALLY DYNAMIC LASER PATTERNING FOR IMAGING MASS SPECTROMETRY STUDIES	33
	Introduction	34
	Experimental Section	37
	Results and Discussion	42
	Laser Beam Distortion Considerations	52
	Conclusion	55
V	IMAGING MASS SPECTROMETRY OF LIPID BILAYERS	57
	Introduction	58
	Experimental Section	60
	Results and Discussion	66
	Conclusion	77
VI	SILVER NANOPARTICLES AS SELECTIVE IONIZATION PROBES FOR MASS SPECTROMETRY	78
	Introduction	79
	Experimental Section	81
	Results and Discussion	83
	Conclusion	92
VII	A MULTI-ANODE DETECTION SCHEME FOR INCREASED RESOLUTION AND SENSIVITITY IN TOFMS	93
	Instrumental and Experimental Design	94
	Resolution	96
	Position Sensitive Ion Detection	98
	Results and Discussion	104
	Conclusion	106
VIII	CONCLUSIONS	107
	Spatially Dynamic Optical System	107
	Sample Preparation Strategies and Methodologies	108
	Multi-anode Detection	110

	Page
REFERENCES.....	111
APPENDIX A	124
APPENDIX B	133
APPENDIX C	136
VITA	152

LIST OF FIGURES

	Page
Figure 1 Optical microscopy image of crystal violet and janus green B deposited onto nitrocellulose in the shape of a microarray.	4
Figure 2 Optical microscopy image of a calf kidney tissue section stained using toluidine blue.	8
Figure 3 Mass spectrometry ion image by LDI-TOFMS of crystal violet deposited onto nitrocellulose in the shape of an ampersand "&."	13
Figure 4 Matrix-Assisted Laser Desorption/Ionization Time-of-Flight Mass Spectrometer (MALDI TOF-MS)	16
Figure 5 Mass spectra of honey bee melittin $[M + H]^+$ ions using linear mode and reflected mode.	18
Figure 6 Schematic diagram of the manual electrospray deposition apparatus used in our experiments.	20
Figure 7 Representative information obtained in a simultaneous top-down/bottom up approach for imaging protein microarrays via MALDI-TOF MS.	23
Figure 8 Optical microscopy images of slices of the protein microarray imaged, where colored circles represent chymotrypsin, trypsin and endoproteinase lys c addition to a model protein mixture, respectively.	26
Figure 9 Peptide fragments observed for chymotrypsin, endoproteinase lys c and trypsin of cytochrome c, ubiquitin, and melittin using the optimized on-plate digestion method.	28
Figure 10 Typical mass spectrum obtained at top-down wells on 4 x 3 microarray using CHCA in the mass range of 500-14,000	30
Figure 11 Mass spectrometry ion images of melittin, ubiquitin and cytochrome c, respectively. Orange circles represent mass spectra with a signal-to-noise ratio greater than 5000.	31

	Page
Figure 12 Diagram of the optical imaging system used in these studies. The laser beam is split into two directions, the imaging path and non-imaging beam path.	40
Figure 13 Calculations for the imaging system used in these studies.	41
Figure 14 Ion image of crystal violet deposited onto nitrocellulose.	43
Figure 15 Schematic diagram of the MALDI optics used for spatially dynamic optical imaging mass spectrometry.	45
Figure 16 Laser beam output profiles illustrating beam profiles at several different regions of the optical setup.	47
Figure 17 Mass spectra obtained by using the optical imaging system with the non-imaging beam path only and with both beam paths open. ...	49
Figure 18 Optical microscopy image of a 2 x 2 peptide microarray deposited on a MALDI plate, where colored boxes represent areas containing angiotensin I and II, respectively.	51
Figure 19 Illustration of a typical arrangement of oblique ionization and camera imaging of the target.	53
Figure 20 Solid-supported lipid bilayers are formed by placing a vesicle solution onto a glass substrate.	62
Figure 21 FRAP experiments were performed using an inverted epifluorescence microscope.	64
Figure 22 Schematic diagram of the sample preparation protocol used for MS analysis.	66
Figure 23 MALDI-TOF mass spectrum obtained from the analysis of a lipid bilayer sample in the TR-DHPE region.	69
Figure 24 Schematic representation of the method used in the TR-DHPE separation studies.	70

	Page
Figure 25 Schematic representation of the method used in the G_{M1} separation studies.....	72
Figure 26 MS ion-specific images for G_{M1} (18:0/d18:1), (middle) G_{M1} (20:0/d18:1) or G_{M1} (18:0/d20:1) and DLPC.....	75
Figure 27 MS ion-specific images for $[\text{Melittin} + \text{H}]^+$ of two bilayer strips of 3 mol % melittin formed by vesicle fusion on a bare portion of substrate in a DOPC matrix.....	76
Figure 28 UV-Vis solution-phase absorption spectrum of 20nm AgNPs.	83
Figure 29 MALDI time-of-flight mass spectra of the 12 component mixture obtained using DHB with 120 μM AgNO_3 and 20nm AgNPs.....	86
Figure 30 MALDI time-of-flight mass spectrum of freshly squeezed carrot juice obtained using DHB.	89
Figure 31 20 nm AgNP LDI time-of-flight mass spectra of folic acid, β -carotene, and amphotericin B.....	90
Figure 32 MS ion-specific images for Ag_3^+ (m/z 320.7), and $[\text{cholesterol} + \text{Ag}]^+$ (m/z 493.3).....	91
Figure 33 Schematic diagram of instrumentation used for position sensitive detection studies.....	95
Figure 34 Potential energy diagram for the Voyager elite XL instrument which contains a two-stage source and single-stage reflectron.....	98
Figure 35 Typical ion detection scheme for TOFMS utilizing a single anode..	99
Figure 36 An image of the 8 anode detector used in these studies, where individual anodes have dimensions of 0.566" x 0.076".....	102
Figure 37 Representation of increased mass spectral resolution and sensitivity after time correction.....	103
Figure 38 Mass spectrum illustrating time shifts across 8 anode position sensitive detector, upon summing each anode a resolution value can be calculated.	105

LIST OF TABLES

	Page
Table 1 Amino acid coverage (%) for cytochrome c using different enzyme to analyte ratio volumes and solvent systems using endoproteinase lys c.	25
Table 2 List of proteins and m/z values for labeled numbers in the top-down microarray wells.....	30
Table 3 List of peptides, lipid and sterol in the 12 component mixture.....	87

CHAPTER I

INTRODUCTION: IMAGING MASS SPECTROMETRY

The ability to completely sequence a genome has opened many new research opportunities in the field of proteomics. Since it is proteins that perform the majority of life functions, the ability to analyze proteins in their native environment is very important. One research area that has advanced the field of biological mass spectrometry in recent years is imaging mass spectrometry. Imaging mass spectrometry (MS) offers the ability to obtain chemical specificity of analytes on a surface in a spatially resolved mode and allows for the ability to analyze proteins/peptides *in situ*. Early imaging MS studies were typically performed using secondary ion mass spectrometry (SIMS) and laser microprobe mass spectrometry (LMMS).¹ SIMS irradiates the sample surface with a tightly focused, highly energetic primary ion beam (typically Ga^+ , Cs^+ , etc.); resulting in the desorption of analyte ions from the surface. Imaging SIMS has been used primarily to probe inorganics, such as metals, minerals, and ceramics; however, the imaging of biological tissues has also been reported.² Recent advances in biological SIMS has focused on using polyatomic ion beams such as C_{60} (fullerene) or gold-clusters to generate higher mass secondary ions than those formed with conventional primary ion beams.³ In LMMS, an ultraviolet (UV) laser is

This dissertation follows the style and format of *Analytical Chemistry*.

focused onto the sample, facilitating ion formation. The primary limitation of both SIMS and LMMS techniques is the limited ability to form intact ions of large (>1000 Da) biomolecules. Some success has been reported using matrix enhanced (ME) SIMS, where a homogenous layer of matrix (small organic acid) is applied to the sample surface prior to mass analysis. Imaging ME-SIMS was used to obtain subcellular resolution of nervous tissue sections (spatial resolution $\sim 3\mu\text{m}$),⁴ where the upper mass range of ionizable analytes (~ 2500 Da) was also increased. Maarten Altelaar and coworkers have shown that by applying a thin (Au) metal layer to the matrix-coated SIMS sample surface prior to analysis results in increased image quality and signal enhancement.⁵ It has also been reported that polymer ion signals are enhanced when nanoparticles (Au or Ag) are incorporated into the sample prior to analysis.⁶

The first successful application of imaging mass spectrometry towards analyzing high mass biomolecules dates back to the late 1990's, when Caprioli and colleagues reported the ability to directly image peptides and proteins in thin ($\sim 10\text{-}20\ \mu\text{m}$) tissue sections based on matrix assisted laser desorption/ionization-time-of-flight mass spectrometry (MALDI-TOF MS).⁷ They demonstrated that by carefully applying a homogenous layer of matrix (using a glass spray nebulizer) to a tissue section the intact ion yield increases. After obtaining a mass spectrum at each x-y position, each spectrum is interrogated to determine the abundance, type and spatial location of specifically chosen biomolecules/biomarkers.⁸ The general principle of imaging mass spectrometry via MALDI-TOF MS is illustrated in Figure 1. Two organic dyes (crystal violet and janus green B) were patterned onto a nitrocellulose membrane using a computer

controlled microspotter. The microarray pattern was subsequently interrogated by rastering the sample with respect to the laser spot in 50 μm increments resulting in 25,600 individual mass spectra which are interrogated providing a mass-specific ion image (Figure 1A). The multidimensional information contained in each “pixel” is shown in Figure 1B which illustrates typical mass spectra at each spatial location. That is, different images are obtained by analyzing the data for individual target analytes (m/z) in the mass spectra which reveal analyte abundance distribution as a function of spatial position.

Caprioli and coworkers have been able to use imaging MS and class prediction models to distinguish between normal and non-small-cell lung cancer.⁹ In addition, the same group was able to distinguish between primary and metastatic lung cancer, yielding a prognosis (poor or good, corresponding to the patient’s survival rate).¹⁰ Combining histopathological and MS techniques allows for the characterization of cell morphology as well as molecular information about the tissue of interest.^{9, 10} Since its inception, Caprioli *et. al.* have analyzed locations of breast cancer biomarkers in human tissue sections¹¹, drug and metabolites in whole body rat tissue sections,¹² and proteins that may be indicative of cell-specific lung cancer.¹³

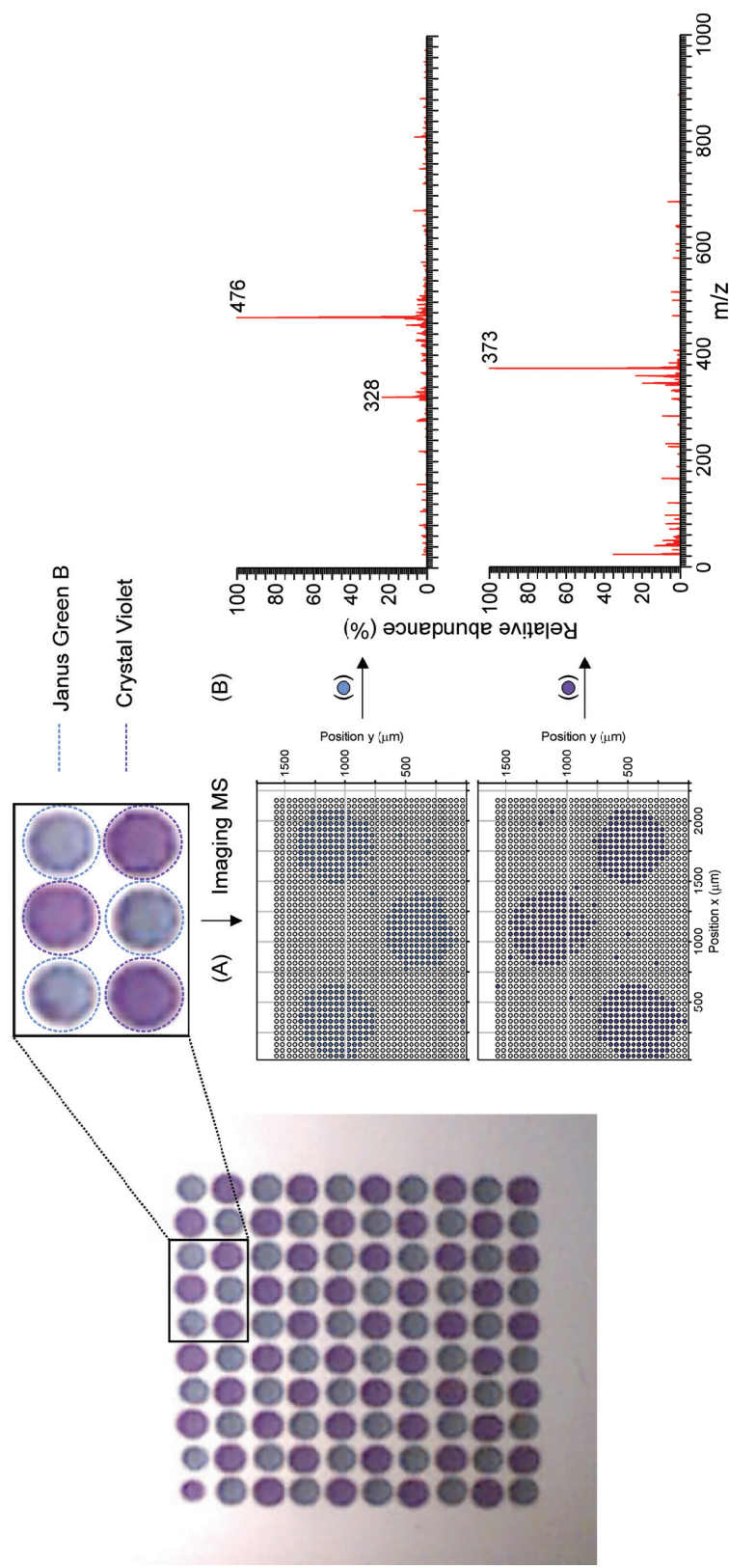


Figure 1. (left) Optical microscopy image of crystal violet and Janus Green B ($m/z = 372$ and $476/328$, respectively) deposited onto nitrocellulose in the shape of a microarray. (A) Expanded mass-specific ion images for crystal violet and Janus Green B. (B) Mass spectra representative of 2 pixels in the images shown in (A). Each mass spectrum represents the average of 25 laser shots and the laser spot ($50 \mu\text{m}$ diameter) was translated in $50 \mu\text{m}$ increments.

Sample Preparation for Imaging Mass Spectrometry

The general procedure for preparing biological tissue samples for analysis is to snap-freeze fresh tissue, followed by sectioning using a cryostat (*ca.* 10-20 μm thickness). Upon fixation of the tissue section to the MALDI plate, a MALDI matrix is applied to the section. The matrix application is dependent upon the type of information that is desired. For imaging experiments, the matrix is applied homogeneously across the entire sample. For profiling experiments (*i.e.*, determination and characterization of differential protein expression), a matrix is applied in discrete spots on the sample for comparison of analyte present in distinct pathological regions.

Typical matrix applications for imaging MS applications consist of applying a homogenous matrix across the entire sample via electrospray deposition, pneumatic nebulization, or dried droplet techniques.¹⁴ To address issues of sample preparation and analyte delocalization/translocation owing to matrix application, alternative matrix applications have been employed. Specifically, Novolkov and coworkers implant massive gold clusters (Au_{400}^{4+}) into the sample prior to analysis.¹⁵ It has been demonstrated that using implanted gold clusters as the MALDI matrix (also known as matrix implanted laser desorption/ionization (MILDI)), large molecular weight analyte ions (up to 35 kDa) can be generated.¹⁶ Other recent work suggests that the deposition of a thin gold layer on non-conductive surfaces prevents surface charge effects in MALDI-TOF MS experiments resulting in increased spectral resolution/ion yields.¹⁷ Currently, researchers have utilized automatic robotic and acoustic matrix spotting techniques,^{18, 19} electrospray deposition,²⁰ matrix sublimation,²¹ solvent-free matrix dry-coating using a

stainless steel sieve,²² spray-coating using an airbrush,²³ and inkjet printing²⁴ for matrix applications. Any of these matrix deposition techniques can be utilized for imaging MS experiments; however a single matrix deposition technique may provide better results for specific experiments. Alternative matrices such as nanoparticles have also been utilized by Taira *et. al.* to image peptides and lipids in mammalian tissue.²⁵

Recent advances in atmospheric pressure ionization techniques such as desorption electrospray ionization (DESI),²⁶⁻³¹ surface sampling probes,³²⁻³⁴ and laser-assisted electrospray ionization (LAESI)³⁵ have also been utilized in imaging MS studies. Vertes and Dreisewerd also used atmospheric pressure infrared (IR)-MALDI to image plant tissues.^{36, 37} These ionization techniques offer the ability to ionize analytes without addition of a MALDI matrix in imaging MS mode, however liquid ionization techniques such as DESI and surface sampling probes provide low spatial resolutions (>100's μm compared to typical 25 μm using MALDI).²⁷

Analyte Identification in Imaging Mass Spectrometry

The challenges of characterizing analytes of interest become more difficult as the complexity of the sample increases. Current MS approaches to identify individual proteins in complex protein mixtures consist of protein isolation (1D- or 2D-polyacrylamide gel electrophoresis) followed by in-gel proteolytic, or proteolytic digestion of the protein mixture followed by multidimensional separation techniques. Peptide fragments are then analyzed using MALDI-TOF MS followed by database searching to identify the protein of interest.³⁸ Owing to the nature of imaging MS experiments, scientists have relied on intact protein data for protein identification. However, as the complexity of the sample increases, the challenges of characterizing analytes in congested mass spectra become more difficult owing to peak overlap by concomitant species of different molecular class (*e.g.*, derived from salts, detergents, tissue fixing agents, lipids, oligonucleotides, glycoconjugates, etc.). Figure 2 illustrates the complexity of mass spectra obtained from a 10 μm thick tissue section from a fresh, frozen calf kidney.

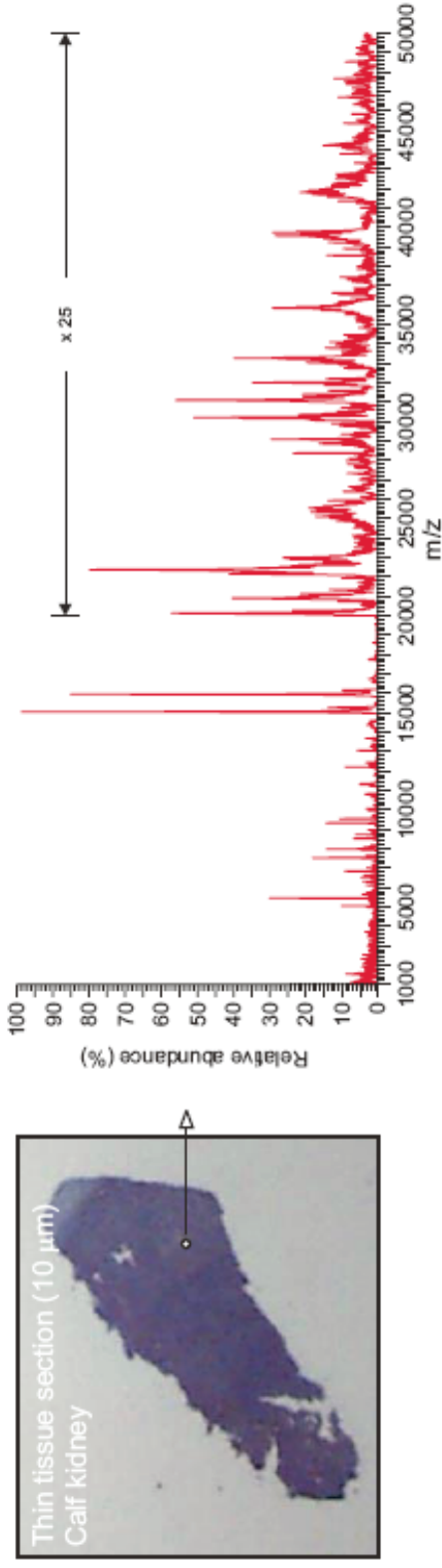


Figure 2. (left) Optical microscopy image of a calf kidney tissue section stained using toluidine blue. (right) MALDI-TOF MS mass spectrum obtained from a 25 μm spot on a 10 μm thick section after applying sinapinic acid (20 mg/mL in 50% acetonitrile/ H_2O , 0.1% trifluoroacetic acid) in the mass range of 1000 to 50000 m/z.

To address analyte identification issues, researchers have used on-plate digestion methods, ion mobility mass spectrometry and high resolution mass spectrometry for accurate analyte assignments. Groseclose *et. al.* robotically spotted small volumes of a protease (trypsin) onto the sample to carry out on-target protease digestion. After digestion, a matrix solution is directly applied to the spots and analyzed by imaging MS to obtain the x-y spatial distribution of peptides. Peptide sequences were also determined by performing MALDI MS/MS directly from the digested areas. By using on-plate digestion, proteins were confidently identified while preserving their spatial distributions.¹⁸ Another digestion protocol that preserves spatial distributions of proteins, known as the molecular scanner approach, utilizes an immobilized trypsin membrane that is sandwiched in between a capturing membrane and the sample of interest (*i.e.*, tissue, gel, etc.).³⁹ The capturing membrane, which now contains peptides, can be imaged and analyzed.⁴⁰

Other researchers have utilized multidimensional post-ionization analyte separation based on gas-phase ion mobility-mass spectrometry to reduce spectral complexity and provide accurate analyte assignments.^{41, 42} Briefly, ion mobility provides a means for separating analytes based on their molecular class (*e.g.*, lipids, oligonucleotides, glycoconjugates, etc.), because each molecular class exhibits a different, but characteristic, trend in mobility as a function of mass.⁴³ Combining post-ionization ion mobility separation with MALDI imaging mass spectrometry provides a second dimension of information (molecular class) to more accurately assign analyte signals.^{41, 42} An additional dimension of analyte information, *i.e.*, characteristic analyte

fragment ions, can be obtained by adding an ion activation step between ion mobility separation and mass analysis without loss of the spatial coordinates on the sample.^{44, 45}

Fourier transform ion cyclotron resonance mass spectrometry (FTICR-MS) has also been used for high mass spectral resolution and mass measurement accuracy to validate analyte assignments for imaging MS applications.⁴⁶ However, the high cost (operation and magnet costs), long analysis times (ms), and low sensitivity of FT-MS need to be taken into consideration when doing these types of experiments.

Spatial Resolution in Imaging Mass Spectrometry

Conventional optical arrangements in imaging MALDI-TOF MS experiments use an aperture followed by a lens to focus the laser beam onto the sample surface, whereby the spatial resolution is dictated by the diffraction limit of the optical system (the laser spot size, $\sim 25 \mu\text{m}$ for conventional imaging MALDI-TOF MS applications). The diffraction limit can be described by:

$$D = \frac{1.22\lambda}{NA} \quad (1)$$

where D is the diffraction limit, λ is the wavelength of light and NA is the numerical aperture of the lens.⁴⁷ The laser spot size and precision of the micropositioners is generally used to determine the maximum spatial resolution obtainable for a particular system.

One strategy for increasing spatial resolution by decreasing the laser spot size consist of scanning microprobe matrix assisted laser desorption/ionization (SMALDI). In these studies, Spengler and Hubert used a confocal cylindrical lens system to focus the laser spot size down to ~ 450 nm.⁴⁸ Scanning near field optical microscopy (SNOM) coupled to MALDI has also been used to increase the spatial resolution in imaging MS experiments, specifically, a near field optical fiber probe is placed very close to the sample surface (within a few nm) which allows the laser spot size to reach sizes smaller than the diffraction limit.^{49, 50} Both techniques have been used for imaging MS experiments, however the ability to detect large biomolecular ions has been unsuccessful possibly owing to sensitivity issues. Other imaging MS laboratories have placed a static aperture in front of the focusing lens system to decrease the laser spot size.^{51, 52}

The challenges associated with mechanical rastering (*i.e.*, via micropositioners) are two-fold. One, wear of the micropositioners causes imprecision and hysteresis (see Figure 3) in translating the sample stage relative to the ionizing beam. Two, mechanical positioning leads to long analysis times when many spatial locations are interrogated owing to slow translation velocities. Figure 3B illustrates the mechanical hysteresis associated with mechanical micropositioners. Specifically, when the sample is rastered in a bidirectional manner, mechanical imprecision's are evident in the mass spectrometry ion image.

One current innovation reported by Luxembourg *et al.* used a triple focusing time of flight mass spectrometer (TRIFT II) in microscope mode to obtain high spatial resolution images of analytes on a surface (in a microarray format).⁵³ In these

experiments, a large diameter ($\sim 200\ \mu\text{m}$) laser beam (single shot) is used for desorption/ionization. Following ion generation, ions are separated according to their m/z ; however, owing to ion optics, ions maintain the same relative spatial orientation from ion generation to detection. The ions are detected as an image on a position sensitive detector, producing a high spatial resolution image of a single analyte.

Two techniques reported by the Sweedler laboratory use oversampling or a bead array to image features smaller than the size of the laser beam. The oversampling technique consists of obtaining MS data in mechanical step sizes smaller than the size of the laser beam (sample probe), however without complete sample ablation at each spot it would be impractical to obtain spatial information in increments smaller than the laser spot size.⁵⁴ The glass stretched bead array technique utilizes a bead array attached to a stretchable membrane. After the tissue section is allowed to dry to the bead array, the membrane is stretched and individual tissue fragments analyzed via MALDI MS.⁵⁵

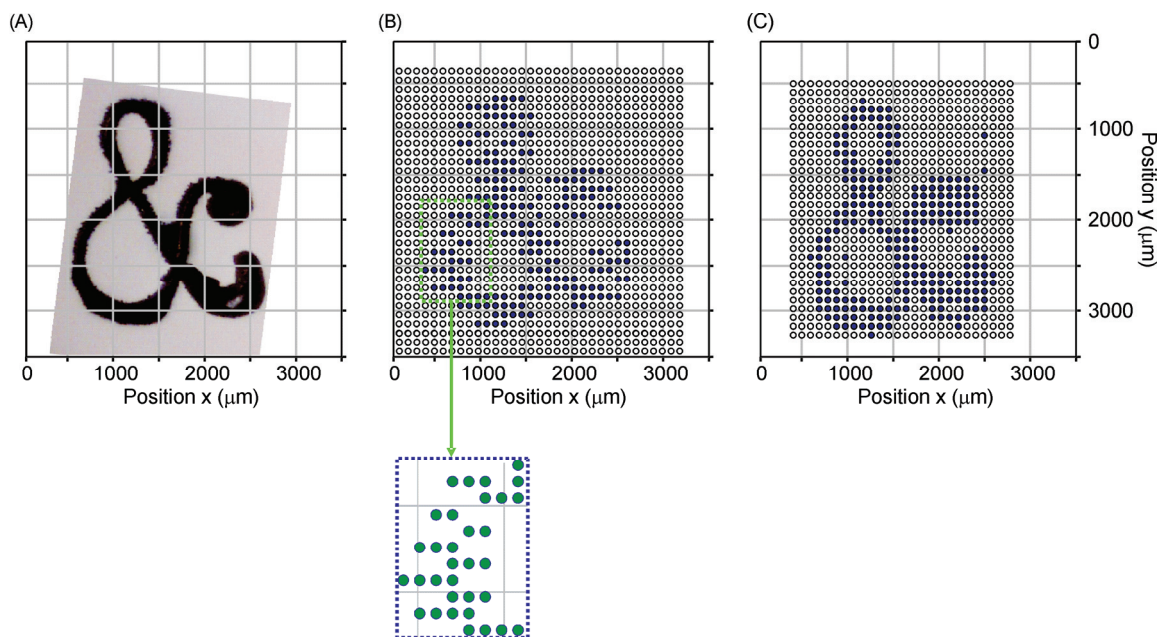


Figure 3. Mass spectrometry ion image by LDI-TOFMS of crystal violet (hexamethyl-pararosaniline, $m/z = 372$) deposited onto nitrocellulose in the shape of an ampersand "&." (A) Optical microscopy image of the deposited material. (B and C) Corresponding images obtained by LDI-TOF MS by rastering the sample with respect to the laser spot in a bidirectional (B) and unidirectional (C) manner, where white and black circles represent mass spectra with a signal-to-noise ratio of less than and greater than 10 at m/z 372, respectively. Each mass spectrum represents the average of 10 laser shots and the laser spot (ellipse, *ca.* 50 x 90 μm) was translated in 95 μm increments to produce the resulting 1056 and 780 pixel images in (B) and (C), respectively.

The objectives of the studies presented here are three fold, these include: (1) develop sample preparation methodologies for spatially resolved mass spectrometry, (2) implement an advanced optical system for imaging MS applications, and (3) modify a commercial TOF mass spectrometer to increase both mass resolution and ion detection sensitivity for MALDI imaging MS. The new optical arrangement is aimed to address three challenges in conventional imaging optics: (i) imprecise mechanical rastering, (ii) static beam shape and dimensions, and (iii) perspective image foreshortening by viewing and irradiating the target at oblique angles. Imaging mass spectrometry utilizing the advanced optics scheme and increased mass spectral resolution detailed in this work will allow more challenging experiments to be performed. Wherein, advanced optics allows increased spatial/lateral resolution and tailored beam dimensions coupled with high-resolution/mass-measurement accuracy allows for increased confidence in mass spectral peak assignments in smaller spatial locations.

CHAPTER II

EXPERIMENTAL

Instrumental Apparatus

A schematic diagram of the experimental apparatus used for the imaging mass spectrometry research is shown in Figure 4. The matrix assisted laser desorption/ionization time-of-flight mass spectrometer (MALDI-TOF MS) is an Applied Biosystems Voyager DE STR equipped with a N₂ laser (337 nm), delayed extraction and is capable of obtaining data in both linear and reflected (single stage) mode. Ions are first generated by irradiating the sample surface with the laser, followed by a delayed extraction event, which consist of accelerating the ions to a constant kinetic energy. After a short delay time, the ions are then separated based on their mass/charge (m/z) ratio in a time-of-flight (TOF) mass analyzer. In linear mode, ions are spatially focused at the linear detector. In reflected mode, the ions are spatially focused at the reflectron entrance and energetically focused in the reflectron (ion mirror). The ion mirror allows faster ions to reach the detector at the same time as the slower ions of the same m/z . A more detailed explanation of ion focusing is discussed in Chapter VII.

The ability to spatially and energetically focus the ion beam allows an overall increase in mass spectral resolution.⁵⁶ Following separation, the ions are detected by a pair of microchannel plates which rely on signal amplification and current detection. Figure 5 illustrates different mass spectral resolution obtained for honey bee melittin $[M + H]^+$ ions that are spatially focused (linear mode) vs. spatially and energetically focused (reflected mode). The top mass spectrum was collected in linear mode and the isotopes are not resolved. Conversely, on the bottom spectrum, using reflected mode, the isotopes are baseline resolved with a resolution of 8,000 for the monoisotopic peak. Unless otherwise noted, all data presented throughout this manuscript was collected in reflected mode under optimized conditions at laser threshold fluences.

Data Validation

All mass assignments were validated using tandem mass spectrometry. Specifically, a MALDI TOF/TOF MS (4800 Proteomics Analyzer, Applied Biosystems, Foster City, CA) was used to obtain collision-induced dissociation tandem MS data. Tandem spectra were acquired using 10-20% greater laser power than the MS spectra acquisition using air as the collision gas with 1 kV of collision energy. All MS and MS/MS data were manually interpreted.

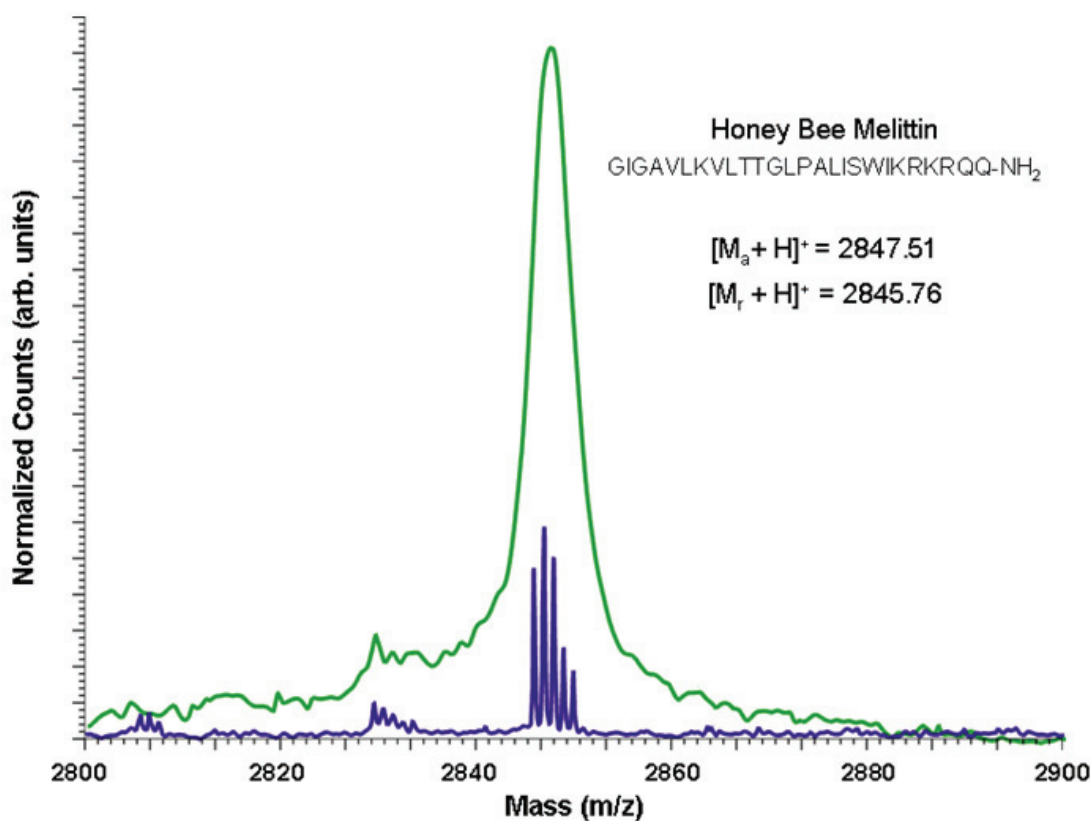


Figure 5. Mass spectra of honey bee melittin $[M + H]^+$ ions using linear mode (green/top) and reflected mode (blue/bottom). The increased mass resolution using reflected mode is apparent by the isotopic baseline resolution of the peptide in the bottom spectrum.

Traditional Mass Spectrometry Sample Preparation

For traditional mass spectrometry experiments, the “dried droplet” sample preparation protocol is utilized. Specifically, a matrix solution, generally α -cyano-4-hydroxycinnamic acid (~10 mg/mL) in 60% acetonitrile, 40% H₂O and 0.1% TFA, is mixed 1/1 (v/v) with the analyte of interest. The matrix concentration will vary

depending on the concentration of the analyte of interest. Matrix to analyte ratios were kept between 1,000-10,000 : 1. After mixing, the solution was spotted directly on the MALDI plate and allowed to dry in air at room temperature prior to analysis.

Imaging Mass Spectrometry Sample Preparation

Sample preparation in imaging MALDI MS can affect analyte localization, therefore it is important that the matrix be applied with care.⁵⁷ Conventional imaging MS matrix applications consist of depositing small drops of the matrix solution (generally sinapinic acid 20 mg/mL in 50% acetonitrile/H₂O, 0.1% trifluoroacetic acid) directly on a dehydrated tissue section. However, owing to the solutions used, a potential challenge is translocation of the soluble proteins within the tissue sample. To reduce this effect, pneumatic nebulization, electrospray deposition and even robotic spotting of the matrix in discrete locations is preferred as the matrix deposition application.¹⁴ In all imaging MS experiments described in this manuscript either pneumatic nebulization or electrospray deposition was utilized. The electrospray deposition is preferred because it provides smaller matrix droplets, and more homogeneous sample matrix deposition compared to pneumatic nebulization.

A schematic of the homebuilt electrospray deposition apparatus is shown in Figure 6. Briefly, a syringe pump is used to push the matrix solution through the capillary and stainless steel needle at a constant flow rate (2-6 μ L/min). The syringe is held at 5,000 V, while the MALDI (stainless steel) plate is grounded. The solution at the end of the needle forms an aerosol of small droplets; this aerosol strikes the surface and

forms a thin layer of matrix once the solvent has evaporated. For these studies, concentrated α -cyano-4-hydroxycinnamic acid (20 mg/mL) in volatile solvents (80% methanol and 20% acetone) provides a thin matrix layer on the sample of interest without analyte delocalization. It is important to note that the flow rate needs to be optimized for particular experiments/solvents, etc.

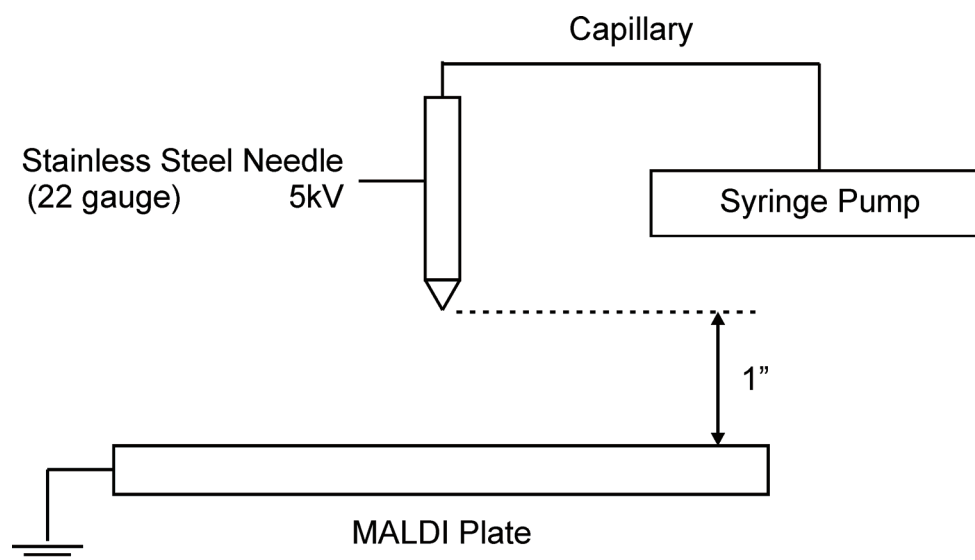


Figure 6. Schematic diagram of the manual electrospray deposition apparatus used in our experiments.

CHAPTER III

IMAGING MASS SPECTROMETRY: A SIMULTANEOUS TOP DOWN/ BOTTOM UP APPROACH

Introduction

The identification of biomolecules using imaging mass spectrometry (MS) has advanced rapidly over the past decade owing to progress in clinical applications and technology. In particular, the application of imaging and profiling experiments in MS is dominated by techniques for the analysis of intact proteins in thin tissue sections (*ca.* 10 μm). Such experiments are performed using MALDI-TOF MS where it is possible to obtain mass spectra at discrete positions (x-y coordinates). Experiments have been performed correlating both histopathology (cell morphology) and MS (molecular information) data at specific target regions. These techniques may ultimately lead to assessing disease diagnosis, prognosis, and determining clinical biomarkers.⁹ We describe a new methodology for obtaining protein profiles by correlating both complementary intact protein (*i.e.* “top-down” MS) and peptide mass fingerprint (PMF, *i.e.* “bottom-up” MS) information using protein microarrays.

As mentioned previously, current approaches to identify individual proteins in complex protein mixtures consist of protein isolation followed by in-gel proteolytic digestion, or proteolytic digestion of the protein mixture followed by multidimensional separation techniques. Separated peptide fragments are then analyzed using MALDI-TOF MS followed by database searching to identify the protein of interest.^{38, 58} Although

intact protein information is lost following proteolytic digestion, smaller and more easily detectable peptides characteristic of the protein are gained. However, the use of one digestion protocol (*e.g.*, trypsin, CNBr, etc.) often leads to peptide fragments which fail to provide 100% sequence coverage, which is desirable in cases such as the determination of sites of post-translational modification. Alternatively, intact protein information and subsequent fragmentation of intact proteins *in vacuo*, provides highly specific information about individual proteins, but fragmentation efficiency is not comprehensive of the protein.⁵⁹ Ideally, both intact protein information and PMF data would be obtained simultaneously particularly for the analysis of complex samples, because it provides higher confidence level assignments owing to the complementary intact protein and digest peptide data. This work has focused on assembling protein microarrays to obtain both intact mass and PMF data to increase protein identification. Figure 7 illustrates the two different approaches (top-down and bottom-up) taken in this study. Microarrays are arranged so that regular patterns of spots containing different proteases (chymotrypsin, trypsin, and endoproteinase lys c) are interlaced with regular patterns of spots containing only MALDI matrix and protein mixture. Figure 7A shows an optical microscopy image of the protein microarray used for MALDI-TOF MS imaging. Figure 7B shows a typical top-down mass spectrum obtained from this array. Figure 7C illustrates the bottom-up approach utilizing the three proteases, yielding three different PMF mass spectra. Multiple proteases were used to increase the sequence coverage obtained in the bottom-up wells, where each spot corresponds to a single protease digestion region.

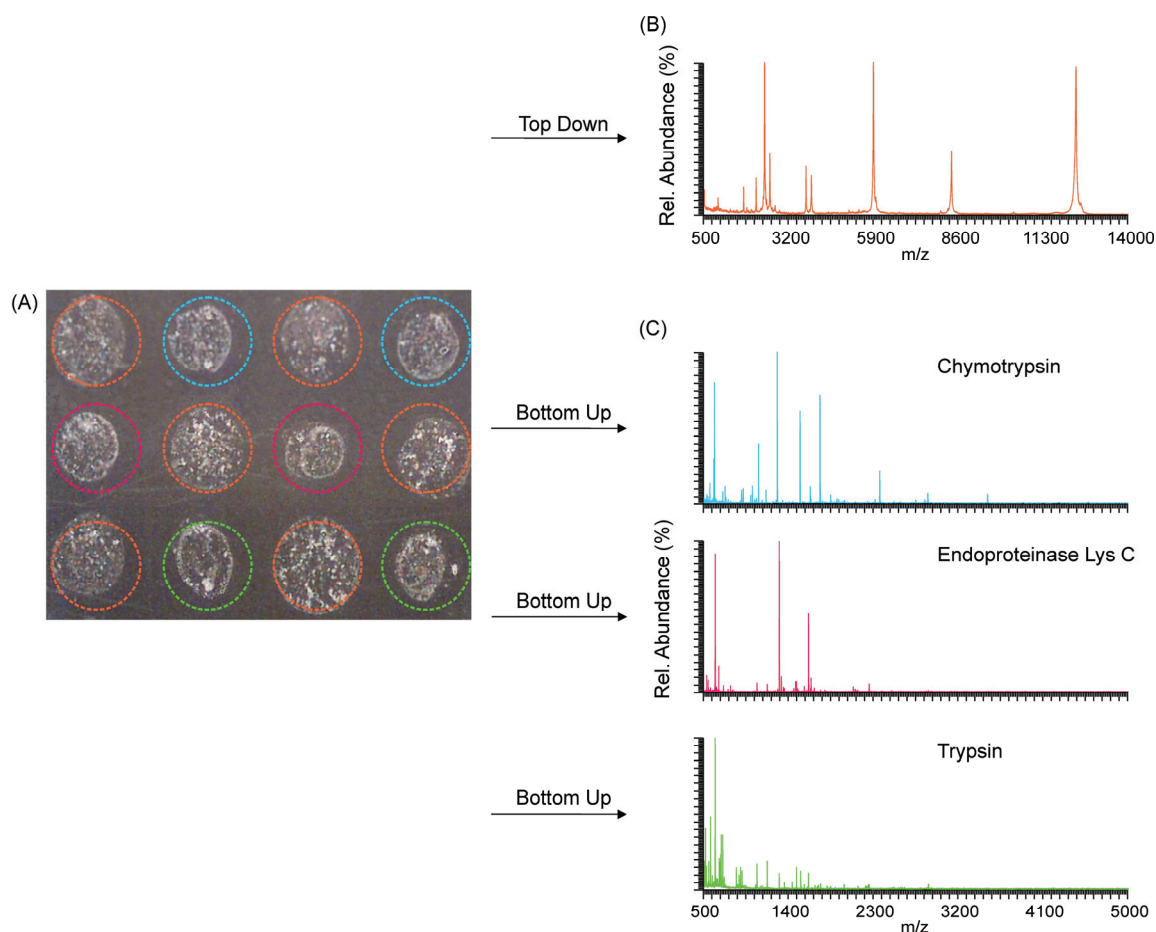


Figure 7. Representative information obtained in a simultaneous top-down/bottom up approach for imaging protein microarrays via MALDI-TOF MS. (A) Optical microscopy image of a protein mixture (consisting of melittin, ubiquitin and cytochrome c) deposited directly on a MALDI plate in a microarray format (B) mass spectrum representing the intact protein masses (top-down approach) obtained from a “top-down” spot and (C) mass spectra illustrating three different PMFs obtained after direct on-plate digestion of three different proteases at specific discrete sample wells.

Bottom-Up Mass Spectrometry

Our initial experiments for obtaining PMF data consist of optimizing protease digestion efficiencies directly on the MALDI plate. A mixed organic-aqueous solvent system (30% Acetonitrile-H₂O) and 1:1 (protease: analyte, w: w) ratios were found to reduce digestion time (< 5 minutes) and maximize sequence coverage. Table 1 shows sequence coverage obtained for three different analyte solvents and protease: analyte ratios using cytochrome c (analyte) and endoproteinase lys c (protease). Subsequent experiments were performed using the optimized method (30% Acetonitrile-H₂O and 1:1 weight ratios of protease and analyte). Time course experiments were also performed to ensure enhanced proteolytic digestion efficiency at 1, 5, 10, 30 and 60 minutes. PMFs obtained between 1-10 minutes were nearly identical, so all experiments were carried out between these times. After optimization, a protein mixture, honeybee melittin ($M_a = 2.8$ kDa), bovine ubiquitin ($M_a = 8$ kDa) and horse cytochrome c ($M_a = 12$ kDa) were interrogated in a microarray format. Protein microarrays were spotted directly on a MALDI plate using a computer controlled microspotter (ProBot, LC Packings, Sunnyville, CA).

Table 1. Amino acid coverage (%) for cytochrome c using different enzyme to analyte ratio volumes and solvent systems using endoproteinase lys c.

Solvent	enzyme: analyte (w:w)	
	1:1	1:10
30% Acetonitrile - Water	77%	60%
50% Methanol - Water	63%	58%
Water	28%	25%

Three proteases were used to increase the sequence coverage obtained in the bottom-up wells, where each spot corresponds to a single protease digestion region (Figure 7). After imaging the microarray using MALDI-TOF MS (Voyager DE STR, Applied Biosystems), digestion efficiency maps of the bottom-up spots were constructed for numerous cytochrome c digestion fragments to determine the efficiency of each protease at different sample spots and within each sample spot. Figure 8 contains four digestion efficiency maps for chymotrypsin and one digestion efficiency map each for trypsin and endoproteinase lys c.

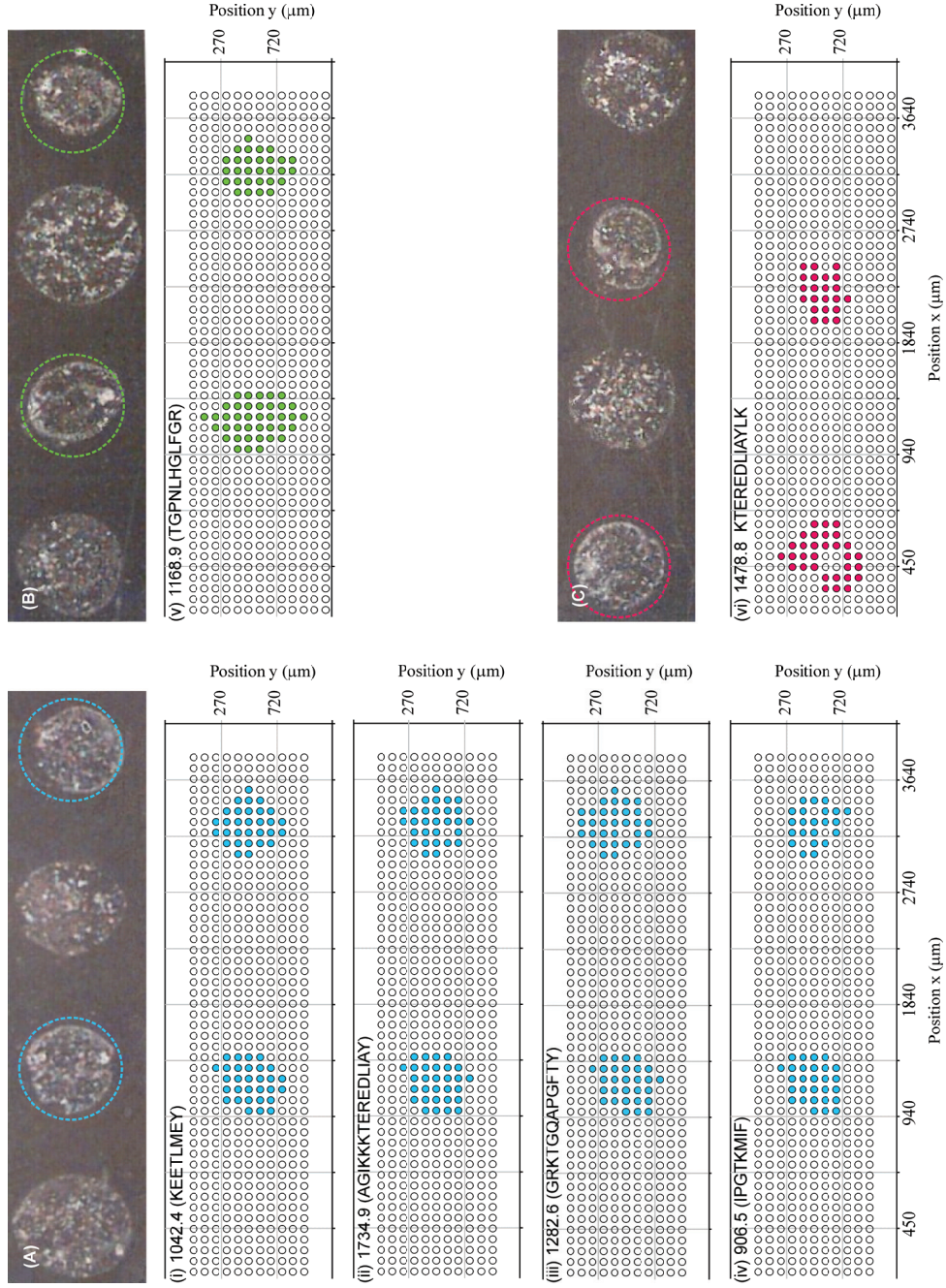


Figure 8. (A-C) Optical microscopy images of slices of the protein microarray imaged, where colored circles (blue, green, red) represent chymotrypsin, trypsin and endoproteinase lys c addition to a model protein mixture (bovine ubiquitin, horse cytochrome c and honeybee melittin), respectively. (i-vi) digestion efficiency maps for each digestion spot for peaks corresponding to m/z 1042.4, 1734.9, 1282.6, 906.5, 1168.9 and 1478.8, respectively. Each m/z corresponds to a unique digest fragment for cytochrome c.

The differences in the efficiency maps is minimal (average variability within spots is $74\% \pm 5.1\%$) for each proteolysis spot and consistent (average spot to spot reproducibility of $72.9\% \pm 6.35\%$) between spots. That is, most digestion efficiency maps (for individual proteases) are nearly identical (Figure 7). Efficiency is measured by comparing the variability within a sample spot and the consistency between spots is measured by spot to spot reproducibility. A comparison of the peptides observed for chymotryptic, endoproteinase lys c and tryptic digests of cytochrome c, ubiquitin, and melittin using all three proteases is presented in Figure 9. The peptides observed by the three proteases overlap significantly. However, by using three different proteases higher protein sequence coverage is obtained. For example, by pooling peptides observed using chymotryptic, endoproteinase lys c and tryptic proteases, protein sequence coverage's of 96.2, 63.2, and 100% are obtained, whereas for tryptic digest only coverage's of 11.3, 42.1, and 0% are found for cytochrome c, ubiquitin, and melittin, respectively.

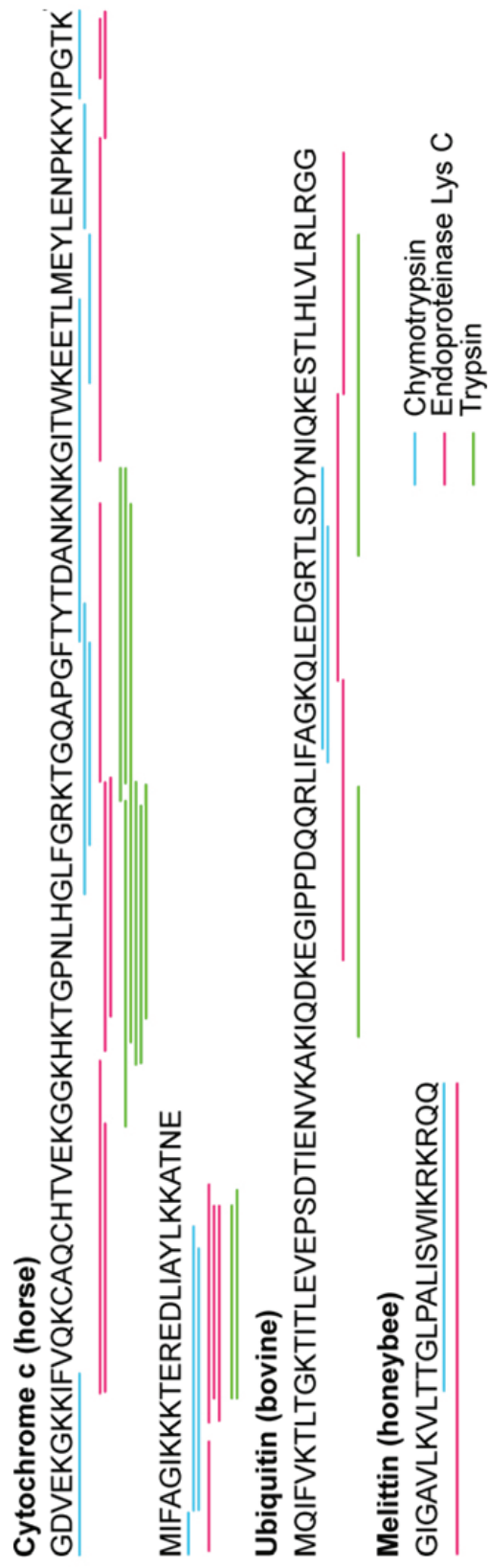


Figure 9. Peptide fragments observed for chymotrypsin, endoproteinase Lys C and trypsin of cytochrome c, ubiquitin, and melittin using the optimized on-plate digestion method.

Top-Down Mass Spectrometry

Initial “top-down” MS experiments consist of optimizing the matrix to analyte ratio (2500:1) and matrix composition (α -cyano-4-hydroxycinnamic acid, CHCA, 5mg/mL in 50% acetonitrile/H₂O, 0.1% trifluoroacetic acid) to obtain intact protein mass data over a large mass range. A mass spectrum taken from the microarray is shown in Figure 10. Observed protonated and doubly protonated species are labeled and summarized in Table 2. All proteins in the mixture show strong signals for both singly and doubly protonated ions, an observation frequently observed in MALDI-TOF MS.⁶⁰ Multiply protonated ions offer another dimension of top-down MS information. Figure 11 illustrates mass spectrometry ion images of melittin, ubiquitin and cytochrome c which were constructed from the top-down spots in Figure 7. All intact proteins were detected at each top-down spot providing a reliable map of overall protein coverage. In all three ion images there is a distorted spot profile appearing at the far right, this has been attributed to the non-uniform spotting using the microspotter. The positive identification in all three mass-specific ion images indicates that there is indeed sample present (no analyte discrimination). While the technological (spotting technique) methodology may need to be improved, the overall utility of the top-down imaging method has been demonstrated.

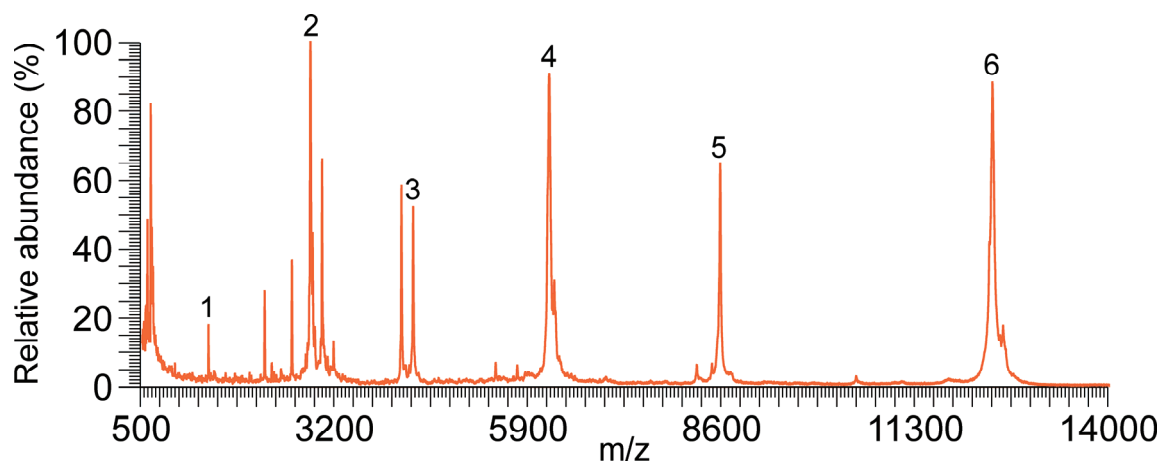


Figure 10. Typical mass spectrum obtained at top-down wells on 4 x 3 microarray (see Figure 7) using CHCA (5 mg/mL in 50% acetonitrile/H₂O, 0.1% trifluoroacetic acid) in the mass range of 500-14,000.

Table 2. List of proteins and m/z values for labeled numbers in the top-down microarray wells.

	Protein	m/z
1	melittin (+2)	1425.9
2	melittin (+1)	2848.7
3	ubiquitin (+2)	4280.9
4	cytochrome c (+2)	6176.9
5	ubiquitin (+1)	8563.5
6	cytochrome c (+1)	12362.1

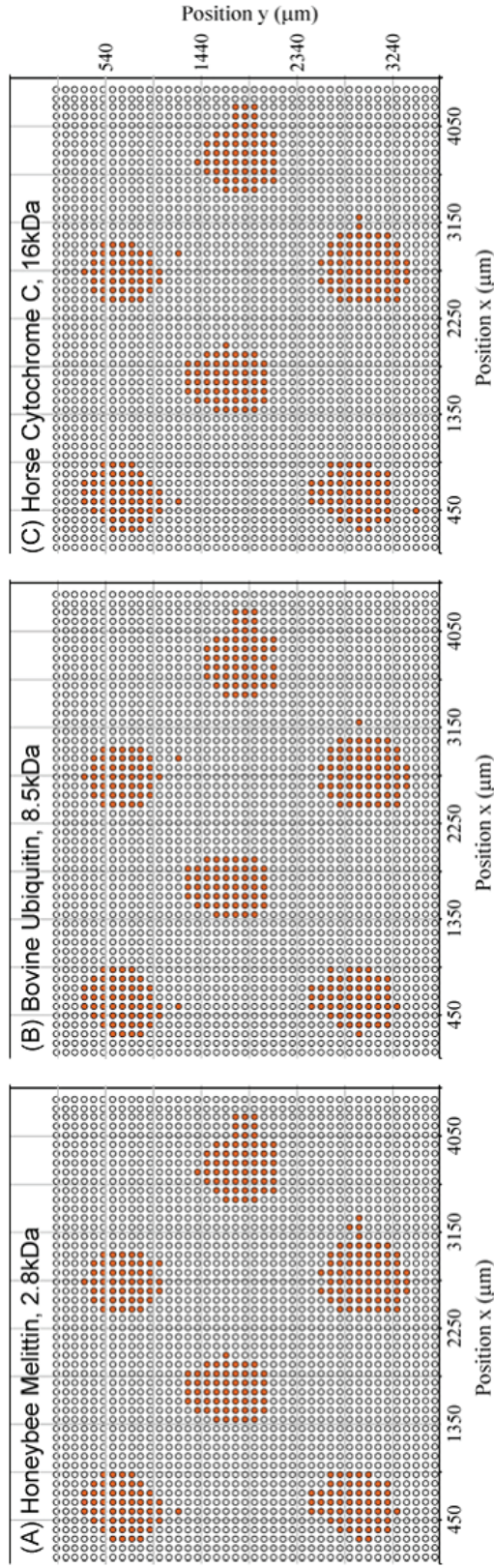


Figure 11. (A-C) mass spectrometry ion images of melittin, ubiquitin and cytochrome c, respectively. Orange circles represent mass spectra with a signal-to-noise ratio greater than 5000. Each mass spectrum represents the average of 50 laser shots and the laser spot was translated in 90 μm increments.

Conclusion

In principle, it is possible to obtain PMF data with high sequence coverage while also providing intact protein mass information. To study the digestion efficiency of proteases for bottom-up spots, digestion efficiency maps were constructed to show minimal spot variability and high spot-to-spot reproducibility. Additionally, we have shown that by using three proteases the overall amino acid sequence coverage is significantly increased. These experiments also provided intact protein mass information, resulting in the ability to correlate proteolytic fragments to intact protein mass. The utility of this methodology is directly applicable to imaging MS of tissue sections, which would allow both intact protein and PMF information to be obtained. There is great utility for this technique with applications ranging from protein profiling, disease diagnosis and prognosis, and increased confidence level in biomarker determinations.

CHAPTER IV

SPATIALLY DYNAMIC LASER PATTERNING FOR IMAGING MASS SPECTROMETRY STUDIES*

Beam homogenization and spatially dynamic beam patterning optics have been combined to improve the imaging matrix assisted laser desorption/ionization time of flight mass spectrometry (MALDI-TOF MS) experiment. The optical design was developed to improve the spatial resolution of the laser beam profile ($\sim 25\text{-}50\text{ }\mu\text{m}$) and to decrease the long analysis times associated with mechanical translation of the MALDI sample stage. This arrangement consists of: laser beam conditioning optics, laser beam shaping optics via a digital micromirror device (DMD), and an imaging lens system. Experimental results comparing traditional imaging MALDI-TOF MS and spatially dynamic imaging MALDI-TOF MS are discussed. The optical system has proven useful for patterning the MALDI laser beam into user defined beam shapes, can potentially decrease analysis times associated with mechanical movement of the sample stage, and may be capable of increasing the limits of detection by simultaneously irradiating multiple spots.

*Parts of this chapter are reprinted from the International Journal of Mass Spectrometry, Volume 262, Stacy D. Sherrod, Edward T. Castellana, John A. McLean, and David H. Russell, *Spatially Dynamic Laser Patterning using Advanced Optics for Imaging Matrix Assisted Laser Desorption/Ionization (MALDI) Mass Spectrometry*, pages 256-262, 2007, with permission from Elsevier Science.

Introduction

Imaging mass spectrometry (MS) utilizing secondary ion mass spectrometry (SIMS)^{61, 62}, laser microprobe mass spectrometry (LMMS)^{1, 63}, matrix assisted laser desorption/ionization (MALDI),^{51, 53, 64} and desorption electrospray ionization (DESI)²⁸ offers the ability to simultaneously obtain spatial and chemical information of analytes on a wide variety of surfaces, such as inorganic, organic and biologically relevant substrates. Recent reports underscore the importance of imaging MS for the spatial profiling of biomolecules (*e.g.*, proteins, peptides) in pathologically relevant tissue.⁶⁵⁻⁶⁸ Also, the ability to combine histopathology with spatial expression profiles of disease specific biomarkers^{9, 69} has the potential for disease diagnosis, prognosis, and to assist in selecting patient specific treatment strategies.⁹

Early imaging MS experiments were performed using SIMS^{61, 62} and LMMS^{1, 63}. Whereas SIMS offers near unparallel spatial resolution, its application to bioimaging is limited by the low ionization efficiencies for high mass ions (molecular weights >1000 Da). Although some progress has been made to enhance signal for high mass ions using matrix enhanced (ME) SIMS⁷⁰, nanoparticle (Au or Ag) incorporated SIMS⁷¹, and thin metal (Au) layer ME-SIMS⁷², large biomolecules (*i.e.*, proteins) cannot be ionized as intact species. The first successful application of imaging mass spectrometry for analyzing high mass proteins dates back to the late 1990's, when Caprioli and colleagues reported the ability to directly image peptides and proteins in thin (~10-20 μm) tissue sections using MALDI-TOF MS.⁵¹ After obtaining mass spectra for peptides/proteins

(mass range of 500 to ~25000 Da)⁷³ at each spatial location, individual spectra were reconstructed to generate molecular ion images of specifically chosen biomolecules.

Although significant advances in sample preparation and data processing have been made, the instrumental arrangement used for imaging MALDI-TOF MS applications has not changed significantly. For example, conventional optics consist of an aperture and a single focusing lens, thus the spatial resolution (size of laser beam at sample surface) is dictated by the diffraction limit of the optical system as well as the shape of the laser beam. The diffraction limit of an optical system can be estimated by (1). Under our current instrumental constraints (NA of 0.05) the diffraction limit of a N₂ laser (337 nm) is about 8 μ m. The maximum spatial resolution obtainable for a particular imaging MALDI-TOF MS system is determined by the laser spot size (diffraction limited) and the precision of the sample plate micropositioners; typical spatial resolutions range between 25-50 μ m. Several strategies have been investigated to increase spatial resolution in imaging MS.^{48-54, 74, 75} Specifically, placing a static aperture in front of the focusing lens system has been successfully employed to decrease the laser spot size in imaging MALDI-TOF MS.^{51, 52} Scanning microprobe MALDI⁴⁸ and near-field scanning optical microscopy coupled with MALDI^{49, 50} have also been used to further decrease the laser spot size to the sub-micron range. All of these techniques suffer from a decreased sensitivity for high mass ions since fewer analytes are sampled in a smaller area⁷⁵ and fragmentation increases owing to the high laser fluences that are required.^{76, 77} In practice, however, the maximum achievable spatial resolution is limited by the overall amount of sample present in individual irradiation

volumes. As irradiation volumes become infinitely small the sample concentration approaches zero. Thus, limits in spatial resolution ultimately arise from instrumental constraints such as ionization efficiency and limits of detection. Other investigators have improved the spatial resolution in imaging MS by using techniques such as oversampling⁵⁴, a parallel sample preparation using glass beads⁵⁵, or special ion optics incorporating a position-sensitive detector (known as the ion microscope).^{53, 75}

Even with these recent advances, current imaging MALDI-TOF MS techniques suffer from static beam shape and long analysis times (minutes to hours) due to the slow mechanical movement of the MALDI plate and low repetition rate lasers typically used in MALDI experiments (*e.g.*, 3-30 Hz). Furthermore, ion image quality should be improved by using square pixels (square beam dimensions) rather than conventional circular pixels (circular beam dimensions). The spatially dynamic optical system described herein provides significant improvements for the imaging MS experiment and consists of: (i) the primary MALDI laser beam, (ii) beam conditioning optics, (iii) a digital micromirror device (DMD), and (iv) an imaging lens system.^{78, 79} DMD devices have found widespread application in video imaging, projection, and telecommunications, but analytical chemistry applications of these devices are limited.⁸⁰ Winefordner described linear DMD arrays (2 x 420 mirror array) to construct a flat-field visible wavelength spectrometer⁸¹, and Fateley described the use of DMDs for constructing Hadamard transform masks for multiplexed Raman imaging^{82, 83} and multiplexed near-infrared flat-field spectroscopy.⁸⁴ Recently, DMDs have also been used to generate oligonucleotide microarrays or so-called "DNA Chips".^{85, 86} By using a

DMD to pattern the UV light onto the DNA chip for photolithography, Sussman and colleagues were able to synthesize microarrays containing greater than 76,000 features having spatial dimensions of an individual DMD mirror element ($16 \times 16 \mu\text{m}$).⁸⁵

Experimental Section

Imaging MALDI-TOF MS experiments were performed on a Voyager DE-STR (Applied Biosystems, Foster City, CA) instrument under optimized conditions in linear mode. This instrument utilizes a nitrogen laser (337 nm), where the laser spot is elliptical, with dimensions of $\sim 50 \times 90 \mu\text{m}$. Crystal violet, hexamethyl-pararosaniline (Sigma-Aldrich, St. Louis, MO), was deposited onto a nitrocellulose membrane sheet (Bio-Rad Laboratories, Hercules, CA) in the shape of an ampersand “&.” The crystal violet solution was prepared at 20 mg/mL in methanol/H₂O (95/5 v/v). The nitrocellulose membrane was then attached directly to a stainless steel MALDI plate using double sided conducting tape (SPI supplies, West Chester, PA).

Peptides (human angiotensin I and II, DRVYIHPFHL ($M_r = 1295.68$) and DRVYIHPF ($M_r = 1045.54$), respectively) were used without further purification (American Peptide, Vista, CA). The peptide solutions were prepared at 1 mg/mL in H₂O. α -cyano-4-hydroxycinnamic acid (CHCA) (Sigma Aldrich, St. Louis, MO) was recrystallized in ethanol and washed with diethyl ether prior to use. A 10 mg/mL solution of CHCA was prepared in 60/40 acetonitrile/water containing 0.1% trifluoroacetic acid, v/v. Samples were prepared by mixing both peptide/matrix 1/1 v/v, followed by spotting a 1 μL mixture onto the MALDI plate. For peptide microarray studies, peptides were

spotted onto a MALDI plate using a computer controlled microspotter (ProBot, LC Packings, Sunnyville, CA).

The beam conditioning optics were evaluated using a nitrogen laser (337 nm, Spectra Physics, Inc., Mountain View, CA) and a CCD camera (Spiricon, Inc., Logan, UT). Images were captured from a screen placed after various components in the optical path. Data were acquired for the unconditioned, expanded, and expanded and homogenized beam.

Spatially dynamic imaging experiments were also performed on a Voyager DE-STR instrument under optimized conditions in both linear and reflected mode utilizing a Nd:YAG laser (355 nm, Tempest-20, New Wave Research, Inc., Fremont, CA). Figure 12 shows a diagram of the optical imaging setup. The laser beam is first split into two distinct paths using a 355 nm beamsplitter (CVI laser, Inc., Albuquerque, NM). 70% of the original beam (imaging beam path) follows the spatially dynamic optical imaging route, while the remaining 30% follows the non-imaging route. The imaging beam path was expanded 3x using a beam expander (CVI laser, Inc., Albuquerque, NM) coated with an antireflective coating for 355 nm. Following expansion, beam homogenization was performed using two microlens arrays (Süss MicroOptics, Neuchâtel, Switzerland) in series, and beam shaping is achieved using a digital micromirror device (DMD) (Tyrex Services Group, Ltd., Austin, Texas). Each microlens array consists of two crossed-cylindrical lens arrays of 300 μm pitch. The DMD consists of 1024 x 768 ($\sim 1 \times 10^6$) individual mirror elements having dimensions of 13 μm per side. Light reflecting from the DMD was focused onto the sample plate using an imaging lens system which

consists of two different lenses (UV grade fused silica, Optosigma, Santa Ana, CA). The focal lengths of both lens 1 and 2 were 39.3" and 6.0", respectively. The imaging lens system components (imaging lens 1 and 2) were chosen to (i) collect all light that is reflected from the digital micromirror device and (ii) demagnify and focus the final image onto the MALDI plate. The thin lens equation (shown in Figure 13) can be used to calculate the overall focal length and demagnification using a two lens system. There is a required amount of energy needed to laser desorb and ionize analytes from the surface known as threshold fluence (energy per unit area), therefore the imaging lens system is chosen so that the highest demagnification is achieved. Owing to physical instrument constraints, the closest the second lens can get to the MALDI plate is 8", thus our calculations take this constraint into consideration. The imaging lens configuration we chose allowed our light to be demagnified by a factor of two when focal length lens 1 and 2 were 39.3" and 6.0", respectively. The distance between object (digital micromirror device) and lens #1 is 10.0", distance between lens #1 and lens #2 is 9.0", and the distance between lens #2 and image (located at the MALDI plate) is 8.0". The ability to demagnify the image increases both spatial resolution and fluence, therefore Appendix A also shows calculations when the distance between lens #2 and image is 2.0". The data illustrates the ability to demagnify your image by a factor of 10 just by placing lens #2 closer to the final image plane (MALDI plate).

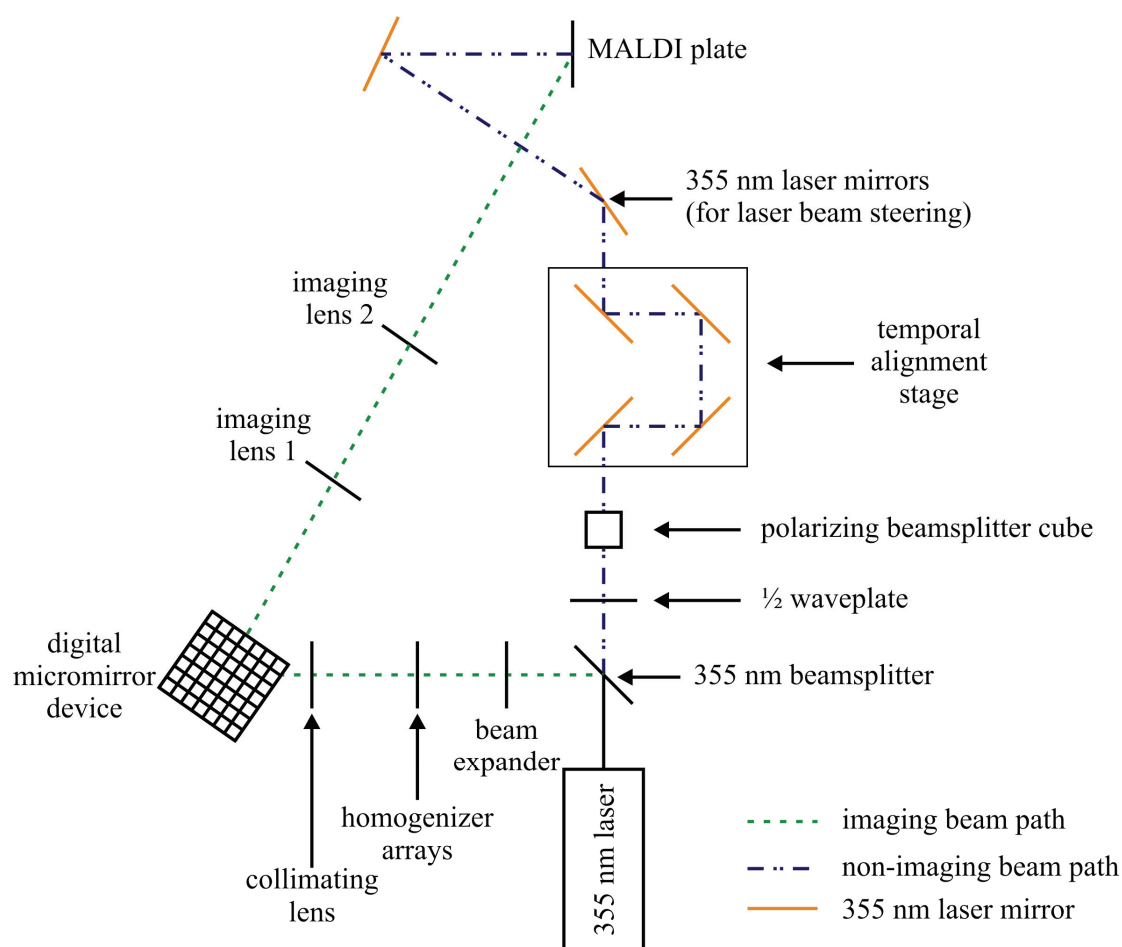
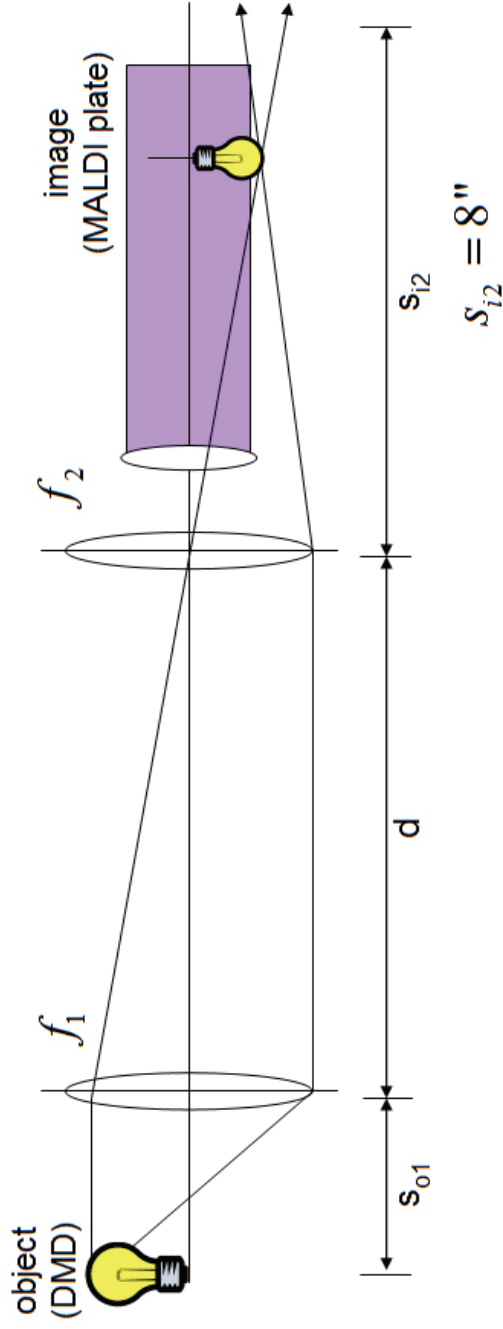


Figure 12. Diagram of the optical imaging system used in these studies. The laser beam is split into two directions, the imaging path (blue dotted line) and non-imaging beam path (green dotted-dashed line).



$$s_{i2} = \frac{f_2 d - f_2 s_{o1} f_1 / (s_{o1} - f_1)}{d - f_2 - s_{o1} f_1 (s_{o1} - f_1)}$$

$$M_T = M_{T1} M_{T2}$$

$$M_T = \frac{f_1 s_{i2}}{d(s_{o1} - f_1) - s_{o1} f_1}$$

s_{i2} (inches)	s_{o1} (inches)	f_1 (inches)	f_2 (inches)	d (inches)	M_T	s_{i2} (inches)	M_T
8	10	19.6	6	9	-0.56	2	-0.14
8	10	19.6	6	18	-0.43	2	-0.11
8	20	19.6	6	18	-0.41	2	-0.10
8	10	39.3	6	9	-0.48	2	-0.12
8	10	39.3	6	18	-0.34	2	-0.09
8	20	39.3	6	18	-0.28	2	-0.07
8	10	1	6	9	0.11	2	0.03
8	10	1	6	18	0.05	2	0.01
8	20	1	6	18	0.02	2	0.01
8	3	1	6	9	0.53	2	0.13
8	3	1	6	3	2.67	2	0.67

Figure 13. Calculations for the imaging system used in these studies. The thin lens equation is shown and numerous calculations illustrating the ability to change the focal length of lens #1, lens #2 and also distances to change the overall demagnification of the final image.

The intensity of the non-imaging beam was attenuated by a $\frac{1}{2}$ waveplate and polarizing beamsplitter cube (CVI laser, Inc., Albuquerque, NM). The beam is temporally aligned using a variable beam path stage and four 355 nm mirrors (CVI laser, Inc., Albuquerque, NM). Following temporal alignment, two additional 355 nm mirrors were used to direct the beam to the MALDI plate.

Results and Discussion

There are several significant instrumental challenges associated with acquiring imaging data using the static beam positioning scheme: (i) poor spatial resolution owing to the MALDI laser spot size (*ca.* 25-50 μm), (ii) fixed laser shape, (iii) inability to probe the spacing between neighboring laser irradiations, (iv) current mechanical repositioning schemes, which are slow and have limited spatial precision, and (v) analysis times directly proportional to the number of spatial elements (x-y coordinates). The spatially dynamic laser patterning optical arrangement described herein has the potential to address each of these challenges.

The general principle of imaging MALDI-TOF MS is illustrated in Figure 14. The spatial distribution for an organic dye (m/z 372) was obtained by rastering the laser spot across the sample while recording a TOF mass spectrum at each coordinate. The information contained at each coordinate is shown in Figure 14C. If multiple analytes are present in the sample, different ion images can be acquired by interrogating the data set for each analytes corresponding mass-to-charge ratio (m/z).

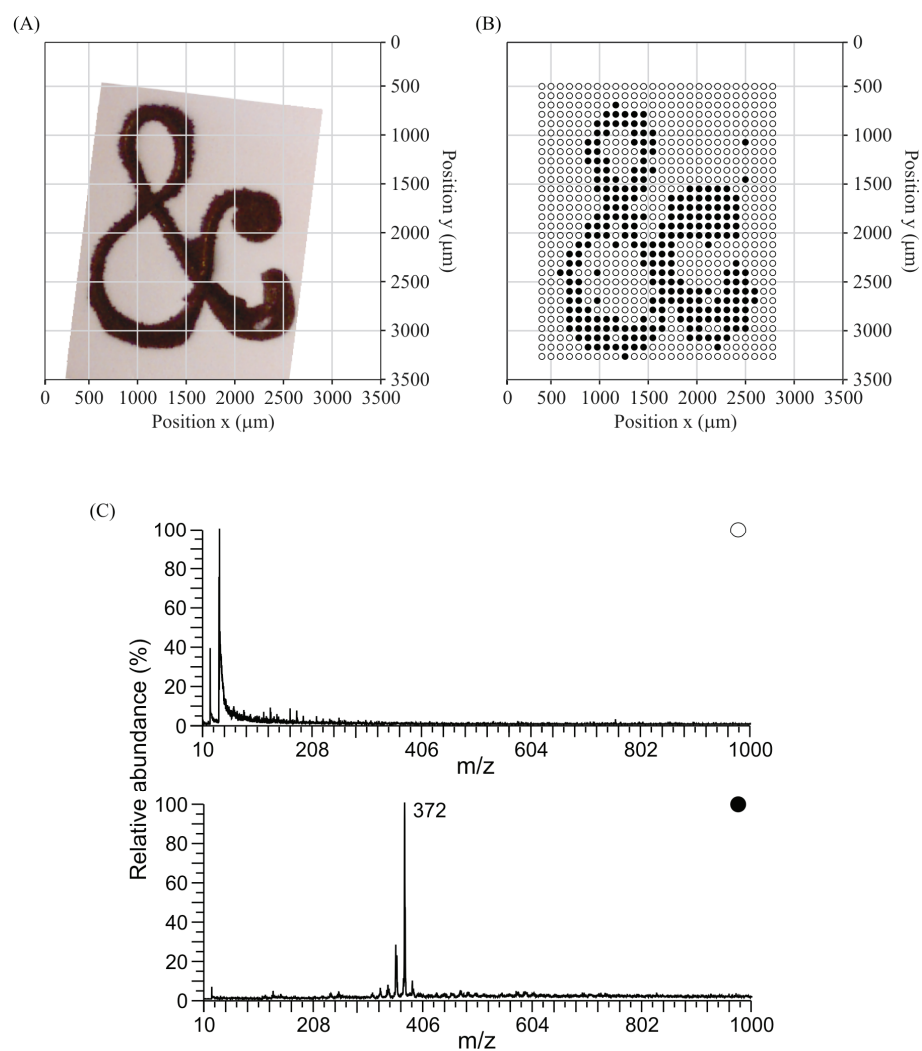


Figure 14. Ion image of crystal violet (m/z 372) deposited onto nitrocellulose. (A) Optical microscopy image of the deposited material. (B) Corresponding image obtained by LDI-TOFMS where open and closed circles represent mass spectra with a signal-to-noise ratio less than and greater than 10 at m/z 372, respectively. (C) Representative mass spectra for open (top) and closed circles (bottom) in the ion image shown in (A). Each mass spectrum represents the average of 10 laser shots and the laser spot (ellipse, ca. $50 \times 90 \mu\text{m}$) was translated in $95 \mu\text{m}$ increments to produce the resulting 780 pixel image.

We have designed a spatially dynamic optical arrangement to improve imaging MALDI-TOF MS experiments (Figure 15A). This optical arrangement allows for beam expansion, homogenization, collimation, shaping, and imaging. First, the primary MALDI laser beam (Figure 15B, i) is expanded and directed through two cross-cylindrical homogenizer arrays. The purpose of these homogenizer arrays is to produce a flat-top beam profile (uniform intensity distribution, Figure 15B, ii). This flat-top beam profile is accomplished by splitting the primary laser beam into wavelets that diverge, overlap, and mix with one another. By using two homogenizer arrays in series, the beam is divided into $\sim 8.1 \times 10^5$ wavelets, which when superimposed produce a flat-top wavefront. Beam homogenization minimizes differences in laser fluence at the sample target which translates to increased reproducibility of MS ion signals.⁸⁷ Homogenization also insures that the data acquired in a spatially resolved format is obtained under comparable conditions. In that, all coordinates in an image will be analyzed at the same fluence (absence of laser hot spots).

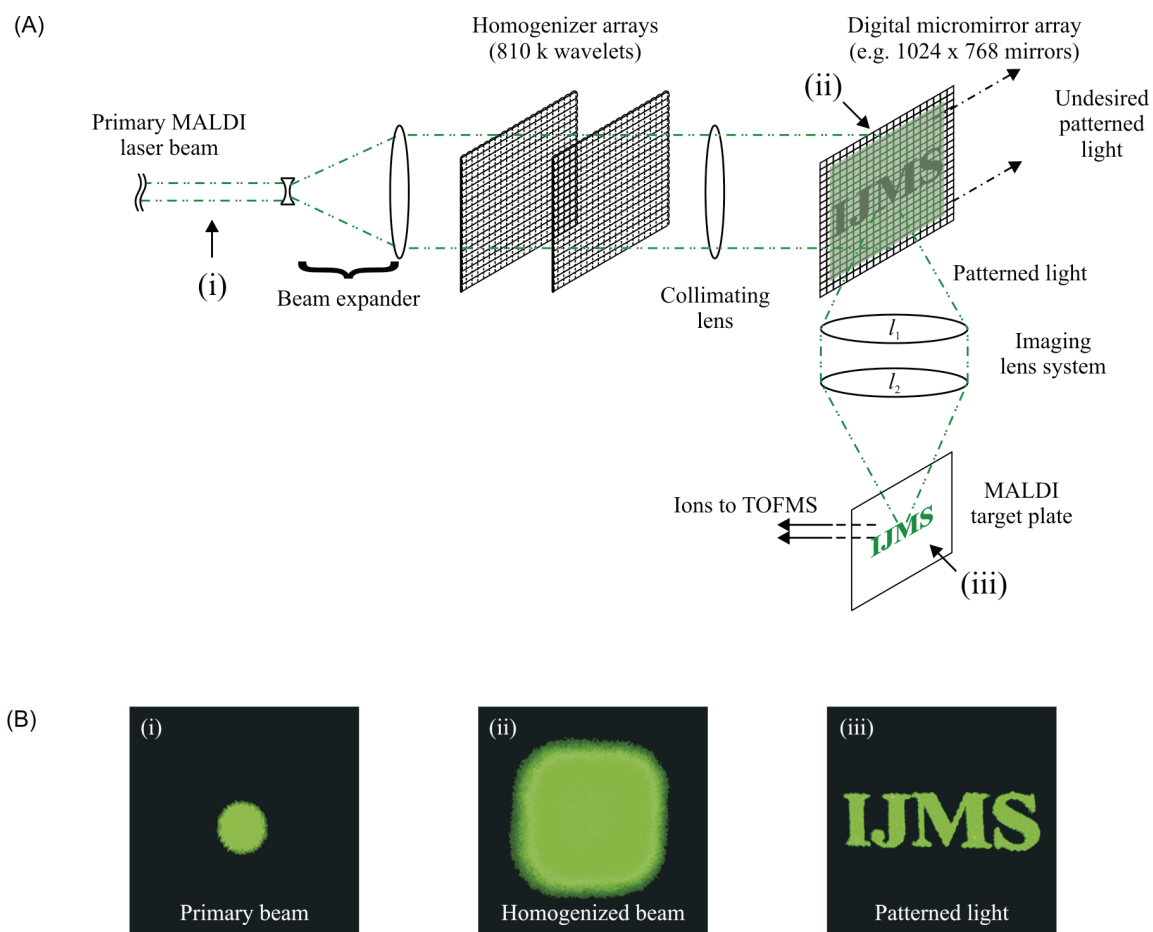


Figure 15. (A) Schematic diagram of the MALDI optics used for spatially dynamic optical imaging mass spectrometry. (B) Digital photographs illustrating the light profile obtained in different regions of the optical arrangement in (A). Photographs of the (i) primary beam, (ii) expanded and homogenized beam and (iii) pattern beam imaged onto the target stage.

Laser beam profiles obtained at three different regions in the optical train (unconditioned, expanded, and expanded and homogenized) are illustrated in Figure 16. Note that the primary and expanded laser beam profiles (Figure 16A, B) contain hot spots, which are observable as distinct peaks in the line profiles. The laser beam profile following beam expansion and homogenization illustrates the reduction of hot spots (Figure 16C), because the line profiles (in both the x and y dimension) are approaching a flat-top profile. The beam conditioning optics (specifically the homogenizers) are very efficient for conditioning Gaussian profile beams into flat-top profile beams. Because the Nd:YAG used in our experiments has a Gaussian profile beam we decided to demonstrate a worse case condition, *i.e.*, nitrogen laser (irregular profile beam) to illustrate the effects of beam conditioning. Even though the homogenizers may not produce a true flat-top profile it is possible to select certain portions of the line profiles to be used in the experiment owing to downstream optical components. For example, only the flat-top portion (and not the wings) of the beam can be selected to be imaged onto the MALDI plate.

After beam homogenization, the laser beam is collimated with a lens and projected onto a digital micromirror device (DMD) (Figure 15A). Each mirror in the DMD is individually addressed by loading a pattern onto on-board memory, which can be quickly changed (up to 5 kHz) in a predetermined and/or dynamic sequence. Based on the bi-stable state of each mirror, the projected MALDI irradiation is the pattern of reflected light from the DMD. An example of light patterning is shown in Figure 15B, iii, which contains digital photographs of light patterned as the letters "IJMS".

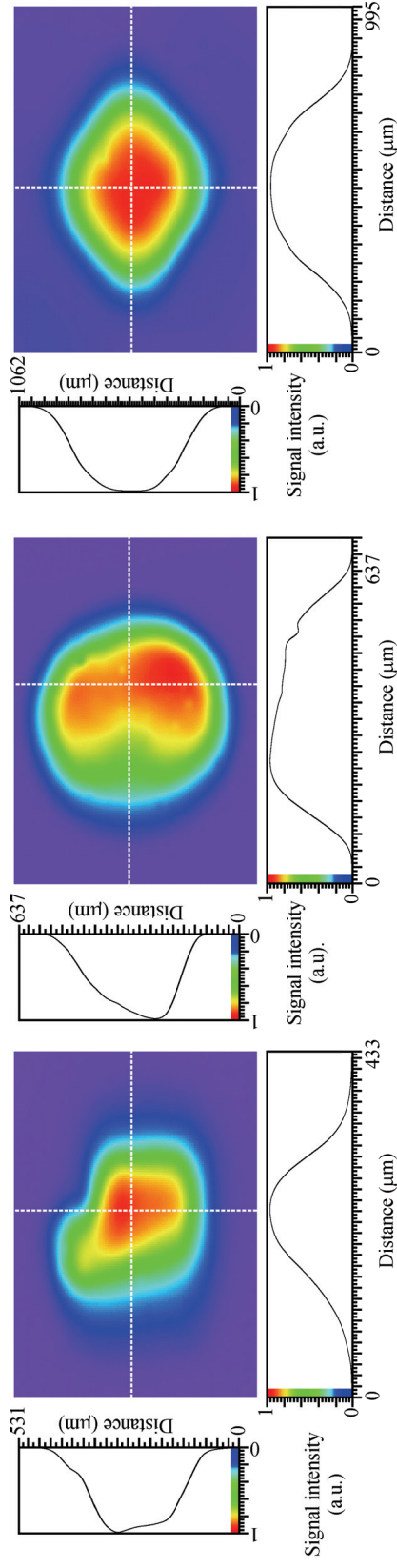


Figure 16. Laser beam output profiles illustrating beam profiles at several different regions of the optical setup. (A) Hot spots in the output beam intensity profile of a primary N_2 laser are evident (beam dimensions of $\sim 300 \times 400 \mu\text{m}$). (B) Laser beam profile following beam expansion also shows hot spots within the laser and increases the beam dimensions to $\sim 600 \times 425 \mu\text{m}$. (C) Laser beam profile following beam expansion and homogenization (beam dimensions of $\sim 800 \times 800 \mu\text{m}$). The primary N_2 laser beam has been transformed into a more flat-top profile beam. (Left and Bottom) The white dotted lines represent signal intensity beam profiles in the y and x dimension, respectively. Each plot is an average of 16 laser shots.

Figure 15 illustrates our ability to easily pattern the MALDI laser into regular shapes (*e.g.*, round, square, rectangular, etc.) or into complex shapes with variable dimensions. Furthermore, the ability to irradiate multiple mirrors at the same time on the DMD allows tailored non-congruent targeted spatial regions to be irradiated simultaneously.

The imaging lens system is used to form a demagnified image of patterned light onto the sample stage. This lens design utilizes a pair of UV lenses in series, where the lens spacing and focal lengths are chosen to optimize both demagnification and numerical aperture given the instrumental constraints (Figure 15A). That is, the MALDI instrument source housing used in these experiments limits the patterned light to be demagnified by 0.44, this demagnification does not supply the necessary energy (fluence $< 1 \mu\text{J}/\text{cm}^2$) needed to generate ions by MALDI.

Proof-of-concept experiments were performed using a split laser beam set-up, whereby the laser beam is split into two different paths (see Figure 12). A portion (70%) of the laser beam is directed toward the imaging optical train which allows beam conditioning and shaping, and another portion (30%) of the beam is directed toward the MALDI plate by a series of mirrors (see Experiment methods for specific details). Both beams were temporally aligned so that both irradiate the MALDI plate at the same time. The non-imaging beam irradiates the entire viewable area of the MALDI plate, and is attenuated just below threshold fluence for MALDI. Figure 17A contains a mass spectrum obtained by irradiating the sample with light from the non-imaging beam path. A similar spectrum (*i.e.*, no ion signal) is obtained if the sample is irradiated by only the imaging beam path. However, when the sample is irradiated by light from both beam

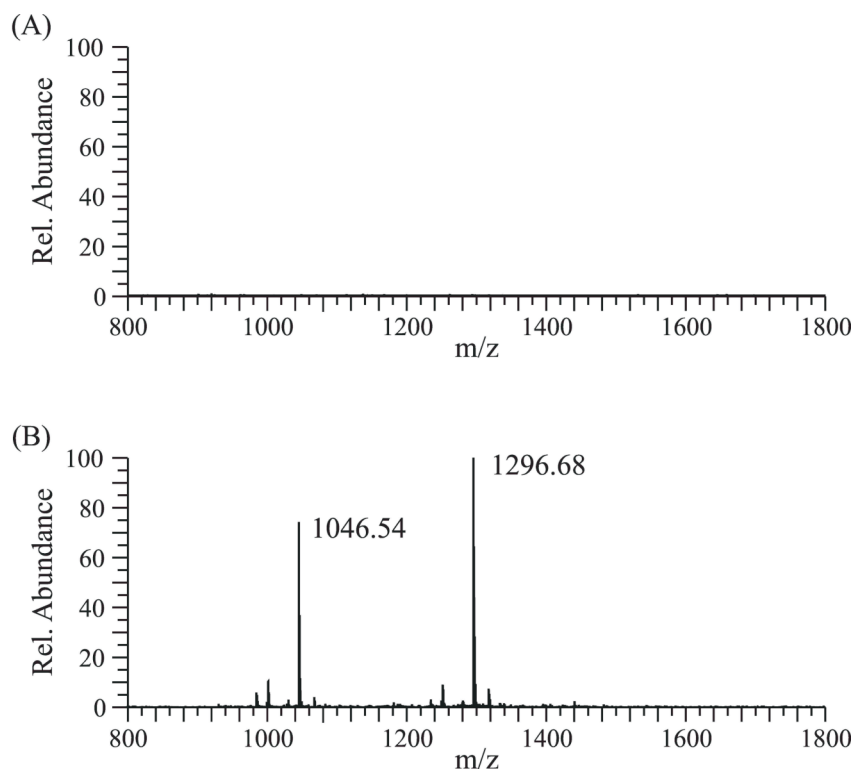


Figure 17. Mass spectra obtained by using the optical imaging system (A) with the non-imaging beam path only and (B) with both beam paths open. Each mass spectrum represents the average of 500 laser shots (reflected mode) and the uploaded image on the DMD is chosen to be a square of 90 x 90 mirrors where the position of light is in the center of the viewable area.

paths, strong signal for the two analytes angiotensin I and II ($[M + H]^+$) are observed (Figure 17B).

Imaging MS is illustrated by using the split laser beam setup to interrogate a 2 x 2 peptide microarray of angiotensin I and II (Figure 18). For these experiments, the laser beam was patterned using the DMD to irradiate individual spots in the array, without mechanically moving the MALDI sample stage. Figure 18A contains the mass spectra for angiotensin II from spots irradiated by the non-imaging beam (top) and with both imaging and non-imaging beams (bottom). When both imaging and non-imaging beam paths are open, signals for the $[M + H]^+$ ion (m/z 1047.2) are observed. The same results are illustrated in Figure 18B for angiotensin I (m/z 1297.5). Operating the instrument in reflected mode was investigated as a means of obtaining high resolution spectra, however laser position proved to be important; laser sampling significantly off the TOF axis yielded little to no ion detection. Subsequently, all spectra in these experiments were acquired in linear mode to decrease dependence on laser position.

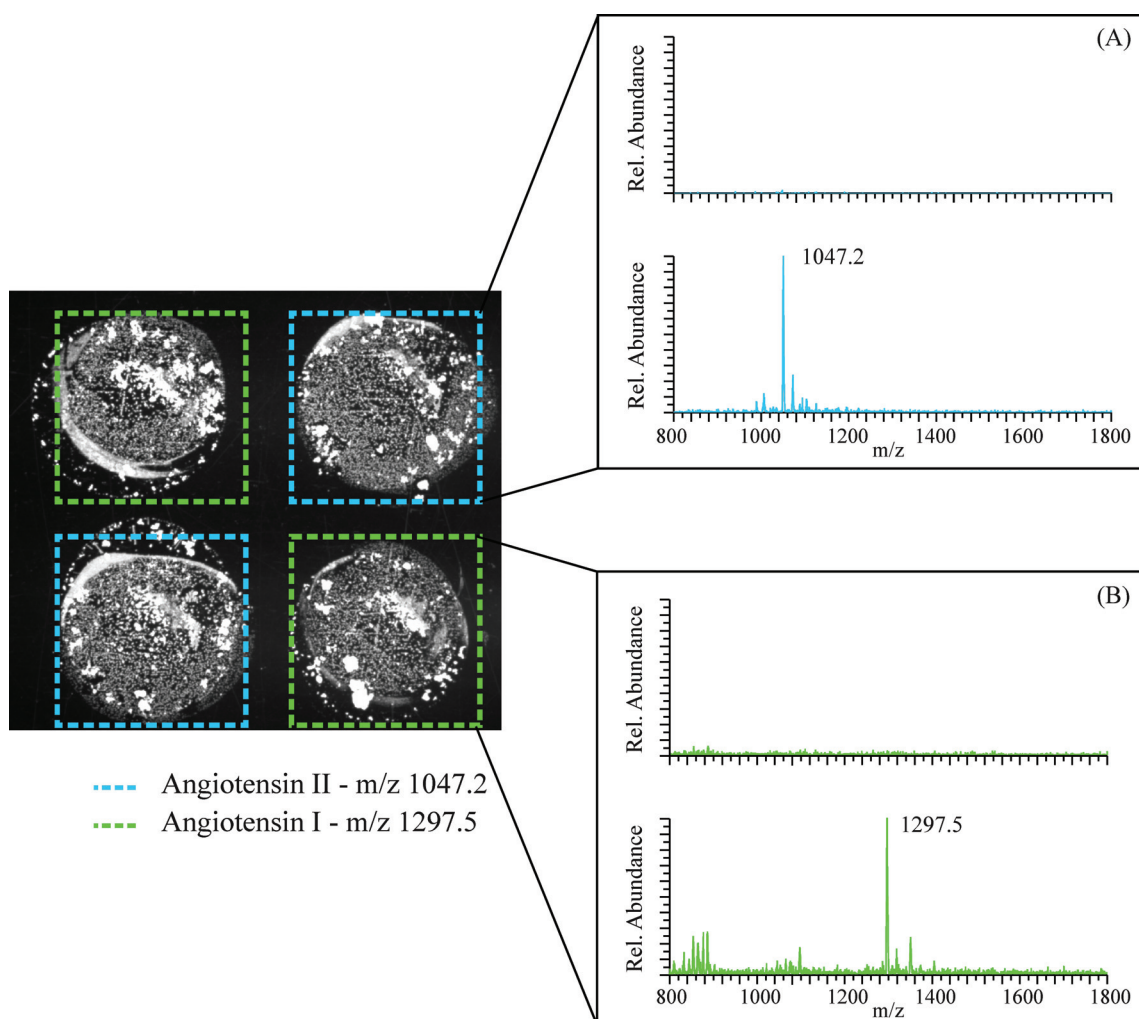


Figure 18. Optical microscopy image of a 2 x 2 peptide microarray deposited on a MALDI plate, where colored boxes (green and blue, corresponding to 750 μm x 750 μm) represent areas containing angiotensin I and II, respectively. (A and B) Mass spectra obtained by using the spatially dynamic optical imaging system (A and B, top) with the non-imaging beam only and (A and B, bottom) with both imaging and non-imaging beams. Each mass spectrum represents the average of 250 laser shots (linear mode), where the uploaded image (90 x 90 mirrors) on the DMD is changed to irradiate the desired spot.

Laser Beam Distortion Considerations

Another challenge in imaging mass spectrometry techniques includes laser beam distortion resulting from the laser beam irradiating the MALDI plate at angles not normal to the sample plate (oblique angles). Figure 19A illustrates the situation where the laser radiation and the imaging optics (*e.g.*, CCD) are focused to the MALDI target at $+30^\circ$ and -30° relative to normal. Figure 19B shows the images projected by both the laser radiation and imaging optics when viewed from these angles. If a square target spot is viewed orthogonal to the MALDI stage it would appear as in Figure 19B, left. However, owing to the oblique angle used for irradiation and viewing, a square projected onto the stage would appear as a trapezoid (Figure 19B, center), and the “true” square sample spot to be irradiated would appear from the imaging optics to be an inverted trapezoid relative to the irradiation (Figure 19B, right).

This imaging distortion can be described algebraically based on geometrical optics, as performed in optical patternation imaging techniques.⁸⁸ Briefly, the trigonometric relation between the DMA and the MALDI target (or MALDI target and CCD array) can be described by (go to page 54):

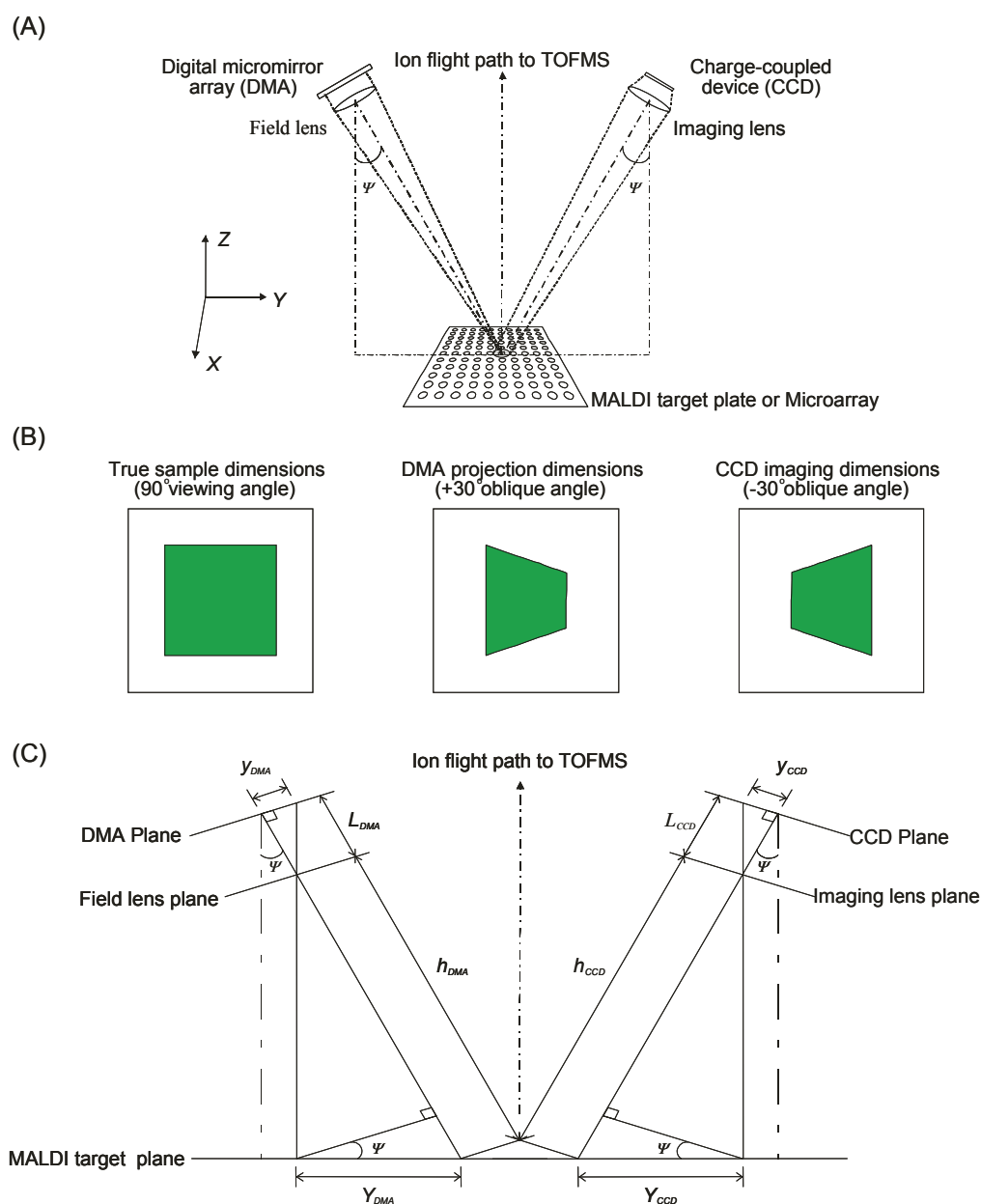


Figure 19. (A) Illustration of a typical arrangement of oblique ionization and camera imaging of the target. (B) Hypothetical shape of a square on the sample stage when viewed normal to the target, and the projected or viewed images obtained at oblique angles. (C) Trigonometric relationships used to correct for oblique perspective distortion in the projected ionizing radiation and the imaging optics.

$$x_{DMA} = \frac{X_{DMA} L_{DMA}}{h_{DMA}} \frac{1}{1 - (Y_{DMA} \sin \psi_{DMA}) / h_{DMA}}$$

and

$$y_{DMA} = \frac{Y_{DMA} L_{DMA} \cos \psi_{DMA}}{h_{DMA}} \frac{1}{1 - (Y_{DMA} \sin \psi_{DMA}) / h_{DMA}}$$

The definition of each variable is illustrated in Figure 19C. Although the equations describing the perspective distortion from the MALDI target to the CCD image plane are similar (*i.e.*, projection or imaging), a distinction is made owing to potential differences in the experimental arrangements for oblique angle (y_{DMA} vs. y_{CCD}), lens-to-projection distance (L_{DMA} vs. L_{CCD}), and image-to-lens distance (h_{DMA} vs. h_{CCD}). In both cases, the magnitude of $(Y \sin \psi)/h$ for practical experimental arrangements is $\ll 1$ and thus a MacLaurin binomial series expansion can be performed:

$$x = \frac{XL}{h} \left(1 + \frac{\sin \psi}{h} Y + \frac{\sin^2 \psi}{h^2} Y^2 + \frac{\sin^3 \psi}{h^3} Y^3 + \dots \right)$$

and

$$y = \frac{YL \cos \psi}{h} \left(1 + \frac{\sin \psi}{h} Y + \frac{\sin^2 \psi}{h^2} Y^2 + \frac{\sin^3 \psi}{h^3} Y^3 + \dots \right)$$

By using the dynamic correction for image distortion afforded by the DMA, a distorted image can be projected from the DMA so that the “true” sample dimensions are irradiated on the MALDI target plate.

Conclusion

In this study, we demonstrate the ability to perform imaging MS using a spatially dynamic optical arrangement. The imaging experiments described differ from traditional imaging MS experiments in that user defined laser beam shape and dimension can be chosen to improve image quality. Patterning light also alleviates the inability to probe the areas between laser irradiations (spaces between laser spots). In principle, it is feasible to increase throughput using this optical arrangement because the DMD allows for faster laser spot relocation relative to sample stage movement.

Clearly, numerous molecular imaging applications are amenable to laser patterning optics. For example, this technique could be used for MALDI-TOF MS imaging of tissue samples, where the advantage of this approach is that imaging could be performed by irradiating single or multiple cells simultaneously. Advanced algorithms could then be implemented for rapid data analysis to compare differences in the mass spectra for the identification of differential expressions. This type of experiment is analogous to a molecular specific, on-line laser capture microdissection imaging experiment in that it allows for an intelligent interrogation of cells.

We are currently developing an imaging lens system to increase demagnification and numerical aperture of the imaging beam in an effort to eliminate the need for split beam experiments and to increase the spatial resolution to the sub-micron range (100's of nm regime). Also, the limitation imposed by probing samples approaching infinitely small volumes may be addressed by implementing congruent imaging, which allows the simultaneous irradiation of multiple spots at various locations on the sample. Irradiation

of visually identical regions (*i.e.*, diseased regions of a tissue sample) which are too small to allow interrogation individually can be simultaneously analyzed. In addition, we plan to incorporate high repetition rate lasers to perform faster analysis and increase sample throughput.

CHAPTER V

IMAGING MASS SPECTROMETRY OF LIPID BILAYERS

Important cellular processes such as cell-cell signaling, peptide/protein interactions and virus attacks against the cell involve the anchoring or immersion of proteins, peptides, and/or small molecules to the selectively permeable lipid bilayer, commonly called the cell membrane. Within the last decade, researchers have moved towards simplifying the analysis of cell membrane species and processes by using solid-supported lipid bilayers (SLBs) as cell membrane models to investigate the chemistry that occurs at the cell surface. Light-based optical imaging techniques are currently used to detect SLBs and require the use of extrinsic molecular tags (*e.g.*, fluorophores) which are sensitive to optical imaging, but introduce complexity within the model and can cause species of interest to deviate from their native states. In contrast, analysis by mass spectrometry (MS) provides native state (tagless) analyte identification owing to the intrinsic measurement of molecular mass. In order to pursue the utility of MS analysis for characterizing model systems of cellular membranes and related processes, supported lipid bilayers are constructed and spatially imaged via matrix-assisted laser desorption/ionization time-of-flight (MALDI-TOF) MS. Membrane incorporated components are separated on the basis of their electrophoretic mobilities across the lipid membrane which is facilitated by a longitudinally applied electric field. After species are electrophoretically separated based on both charge state and interaction with the bilayer, the bilayers are appropriately prepared and imaged using MALDI-TOF MS to determine

both the identities (via MS mass measurement) and spatial locations of components within the SLBs.

Introduction

Cell membranes are complex arrays that incorporate numerous different types of molecules (*e.g.*, lipids, proteins, cholesterol), as well as facilitate many important physiological and pharmacological processes. The motivation to express, purify and determine the structure of membrane proteins is necessitated by drug discovery, since up to 70% of drug targets are membrane species. Recently, many research initiatives have focused on studying the structural biology of membrane proteins; these include: (i) protein expression, (ii) purification and (iii) structure determination.⁸⁹ Membrane species, in particular, membrane proteins have low solubility in water, therefore the ability to separate, purify and detect them is difficult since our current state of separation and analysis technologies were developed in aqueous systems. Additionally, current purification techniques are typically performed under relatively harsh conditions (*e.g.*, detergents) which can alter the native structure, stability, and yield of species of interest, or in some cases can result in complete loss of analyte.⁹⁰ These detergents can also interfere with analytical results using x-ray crystallography, mass spectrometry and NMR.⁸⁹ Therefore, there is strong impetus to design and implement new techniques for separation, detection, and characterization of transmembrane species.

The use of model cell membrane mimics such as solid-supported lipid bilayers (SLBs), have allowed scientists to probe specific chemistries that occur on the cell

surface that would otherwise be impossible to investigate *in situ*. Recently, Cremer and coworkers have demonstrated the ability to rapidly separate membrane bound components without exposing the system to detergents that would otherwise complicate the experiment and disrupt the native interaction of these chemical species with the membrane. In this work, a solid-supported lipid bilayer was employed as the separation medium to laterally separate membrane-bound species. Initial results demonstrate the separation of fluorescently labeled structural isomers from each other within the lipid bilayer. While light-based optical imaging is an effective analytical tool for detecting and monitoring the mobility of these membrane bound species across the bilayer, the use of extrinsic molecular tags (*e.g.*, fluorophores), imposes a significant limitation on the experiment, since these chemical modifications can alter the native structure and activity of the analytes. An emerging technique that has promise for spatially resolving and characterizing native membrane bound species is imaging MS. Imaging MS is an inherently "tagless" technique, which provides spatial information of either the intact ionized analyte or a characteristic fragment ion signal derived from, and representative of, the analyte. Numerous research efforts by Boxer, Winograd, Ewing, and Sjövall have utilized secondary ion mass spectrometry (SIMS) imaging to study the phase separation of membranes,^{91, 92} locate sphingomyelin and cholesterol in domains,^{93, 94} quantify the distribution of cholesterol in cell membranes,⁹⁵ and probe the differences in ion signals for varying types of lipid membrane assemblies.⁹⁶ While SIMS imaging offers very high spatial resolution (~ 1 nm to $3\text{ }\mu\text{m}$), its ability to ionize intact molecules larger than 1,000 Da is challenging. Thus, studies presented here utilize MALDI

imaging MS since MALDI can ionize large intact biomolecules while compromising a modest tradeoff in spatial resolution (25-50 μm) as compared to SIMS imaging. In particular, this work investigates the chemical composition and location of intact membrane-bound species after electrophoretic migration in a SLB.

Experimental Section

Materials. Melittin peptide was purchased from American Peptide (Sunnyvale, CA) and used without further purification. Lipids, cholesterol (chol), 1-Palmitoyl-2-Oleoyl-*sn*-Glycerol-3-Phosphocholine (POPC), 1,2-Dioleoyl-*sn*-Glycerol-3-Phosphocholine (DOPC), 1,2-Dilauroyl-*sn*-Glycerol-3-Phosphocholine (DLPC), and Ganglioside G_{M1} were acquired from Avanti Polar Lipids (Alabaster, AL). The fluorescently labeled lipid, Texas Red 1,2-dihexadecanoyl-*sn*-glycerol-3-phosphoethanolamine (TR-DHPE) was purchased from Invitrogen (Carlsbad, California). Other chemicals and substrates used in these studies were from the following commercial sources: glass coverslips (VWR International, LLC., West Chester, PA), MALDI matrices, 2,5-dihydroxybenzoic acid (DHB) and *p*-cyano-4-hydroxycinnamic acid (CHCA) (Aldrich Chemicals, Milwaukee, WI) and 7X cleaning solution (MP Biomedicals, Aurora, OH).

Sample Preparation. Small unilamellar vesicles (SUVs) were prepared by mixing the appropriate components (TR-DHPE, POPC, DOPC, DLPC, melittin, chol, or G_{M1}) in chloroform (or methanol), followed by drying under a stream of dry nitrogen and desiccating under vacuum (10^{-3} Torr) overnight.⁹⁷ After desiccation, the components are

rehydrated in phosphate buffer saline (PBS) solution at pH 7.4 and subjected to ten freeze/thaw cycles by alternating between freezing in liquid nitrogen followed by thawing in a 30°C water bath. The small unilamellar vesicle solution was then extruded 5 times through a polycarbonate filter (Whatman, Florham Park, NJ) containing 50 nm pores to produce vesicles of uniform size.

Glass supports (coverslips) were cleaned in 7X solution using previously described procedures.⁹⁸ Briefly, the glass supports were boiled in a 7X solution that was diluted seven fold by volume using purified water. After cleaning, the glass coverslips were annealed in an oven at 500° C for 5 hours and stored until further use.

Solid-supported lipid bilayers were formed on a planar substrate (glass) using the vesicle fusion method (Figure 20).⁹⁹ Briefly, a small unilamellar vesicles solution (~150 μ L) was placed on a clean hydrophilic glass coverslip confined by a polydimethyl siloxane (PDMS) hydrophobic well. The small unilamellar vesicles adsorb, fuse and spontaneously assemble on the glass surface to form a lipid bilayer. After incubating for 5 minutes, the sample was rinsed with DI water to remove any excess, unfused vesicles. Strips in the bilayer were prepared by removing a thin strip of the previous formed bilayer (referred to as the lipid matrix bed) using Teflon coated tweezers or glass slides. After a second rinsing of the sample, ~150 μ L of vesicle solution containing the appropriate peptide (melittin), glycolipid (G_{M1}), or dye labeled lipids (TR-DHPE) were added to the PDMS well. After incubating for 5 minutes, excess vesicles were removed from the samples using DI water.

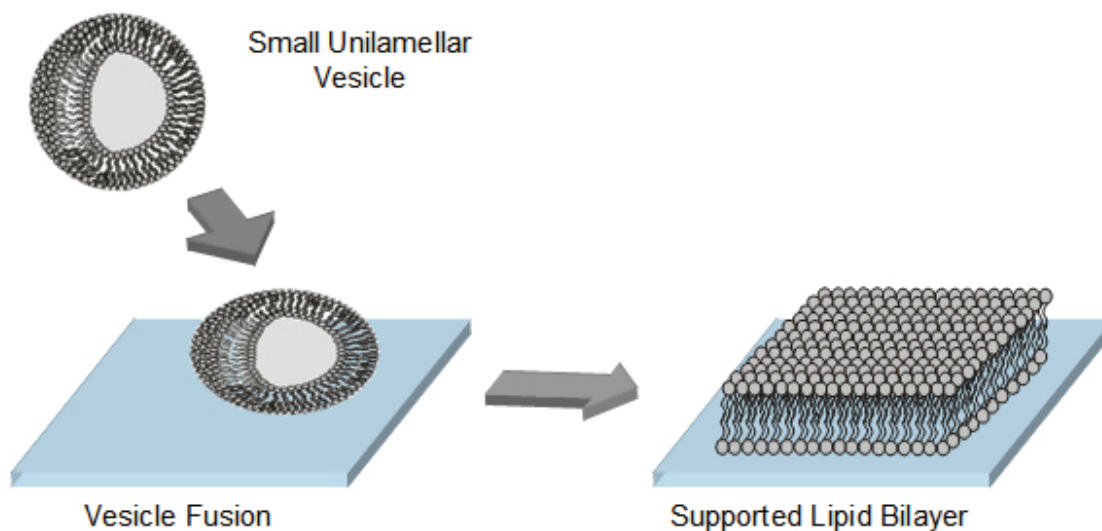


Figure 20. Solid-supported lipid bilayers are formed by placing a vesicle solution onto a glass substrate. The vesicles adsorb, fuse and spontaneously assemble at the surface to form lipid bilayers.

Solid-supported lipid bilayers were characterized using fluorescent recovery after photobleaching (FRAP) to measure the diffusion coefficients and mobile fractions of TR-DHPE. FRAP experiments consist of photobleaching a small area of the fluorescently labeled lipid bilayer using a 568.2 nm line from a mixed gas Ar^+/Kr^+ laser beam (Stabilite 2018, Spectra-Physics, Mountain View, CA) and measuring fluorescence recovery time. Since the components of a properly formed membrane are free to laterally diffuse across the plane of the membrane, the fluorescent recovery should be above 90%. However, if the lipid bilayer did not form properly (*i.e.*, absence of vesicle fusion and rupture) the fluorophores cannot properly diffuse across the membrane, resulting in no

fluorescent recovery being observed. The diffusion constant (D) can be calculated by the following equation,¹⁰⁰

$$D = \frac{w^2}{4\tau_{1/2}} \gamma_D \quad (2)$$

where $\tau_{1/2}$ is the half life of the fluorescent recovery, γ_D (1.2) is a correction factor that depends on the geometry of the laser beam and bleach time, and w (17.7 μm) is the full width at half maximum of the Gaussian profile beam. The data in Figure 21 depicts the measured values for the fluorescence recovery for 5 mol % TR-DHPE, 95 mol % POPC as a function of time. The data was fit to a single exponential equation, and half life fluorescent recovery ($\tau_{1/2} = 23$ s) obtained. The diffusion coefficient was then calculated using (2). The value of the diffusion coefficient for 5 mol % TR-DHPE, 95 mol % POPC is $2.7 \pm 0.4 \times 10^{-8} \text{ cm}^2/\text{s}$ with 94 ± 4 % recovery. This data agrees well (within experimental error) with previous 0.1 mol % TR-DHPE, 99.9 mol % POPC lipid bilayer studies.¹⁰¹

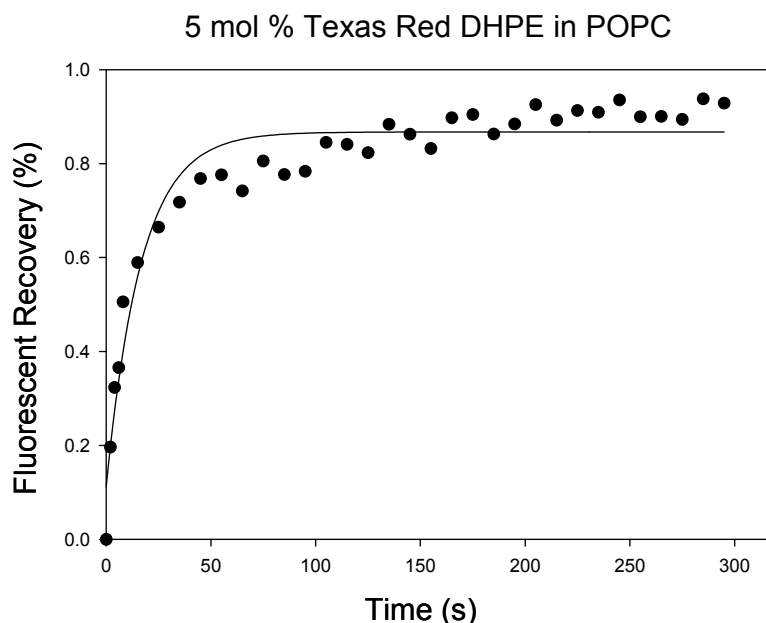


Figure 21. FRAP experiments were performed using an inverted epifluorescence microscope. FRAP curves are used to characterize the lateral mobility of the lipid bilayers to ensure that a lipid bilayer is formed. This fluorescent recovery curve illustrates the fluorescence recovery for a membrane containing 5 mol % TR-DHPE in POPC.

Electrophoretic separations were performed by applying a potential (100 V - 200 V) laterally across the lipid bilayer via two platinum wire electrodes placed at each end of the PDMS well. A voltage regulated power supply (Lamdbd Electronics Corp., Long Island, NY) was used to maintain a constant potential across the bilayer while the current was monitored with a digital multimeter to ensure currents remained below two microamps. The movements of the fluorescent bands (when used) were monitored using time lapse photography at five minute intervals using a Nikon Eclipse TE2000-U

equipped with a Sensys CCD camera (Photometrics, Roper Scientific, Pleasanton, CA) supported by the Metamorph Software (Universal Imaging, Downingtown, PA).

Figure 22 outlines the protocol used to prepare lipid bilayers for imaging MS. After electrophoretic separation of the analytes, the hydrated samples were rapidly frozen by immersion in liquid nitrogen cooled ethane. Following flash freezing, samples were transferred to liquid nitrogen, and allowed to dry frozen. The freeze drying procedure was utilized to remove water from the sample without disrupting the lateral organization of the species within the membrane. During freeze drying, the samples were kept at -20°C under vacuum (10^{-3} Torr) until all ice has sublimed away (3-5 hours). Following freeze drying, the solid support of the lipid bilayer was adhered to a MALDI plate using double-sided copper conducting tape followed by applying a matrix (20 mg/mL CHCA in 80% acetone and 20% methanol) via aerosol deposition. A wire mesh is applied across the top of the sample to minimize surface charge buildup effects during the MS experiment, and the sample is introduced into the mass spectrometer.

All imaging MS experiments were performed on a 4800 Proteomics Analyzer MALDI TOF/TOF (Applied Biosystems, Foster City, CA) mass spectrometer under optimized conditions in reflected mode utilizing a frequency tripled Nd:YAG laser at 355 nm as the ionization laser. Imaging samples were translated in 60 μm increments due to the observation that the laser spot size was projected onto the sample as an ellipse, *ca.* 60 x 100 μm , when projected onto the sample surface. Individual mass spectra represent the average of 250 laser shots. Mass assignments were validated using tandem MS

experiments. Collision-induced dissociation tandem MS spectra were acquired using air as the collision gas (medium pressure (4.0×10^{-7} Torr)) at a collision energy of 1 kV.

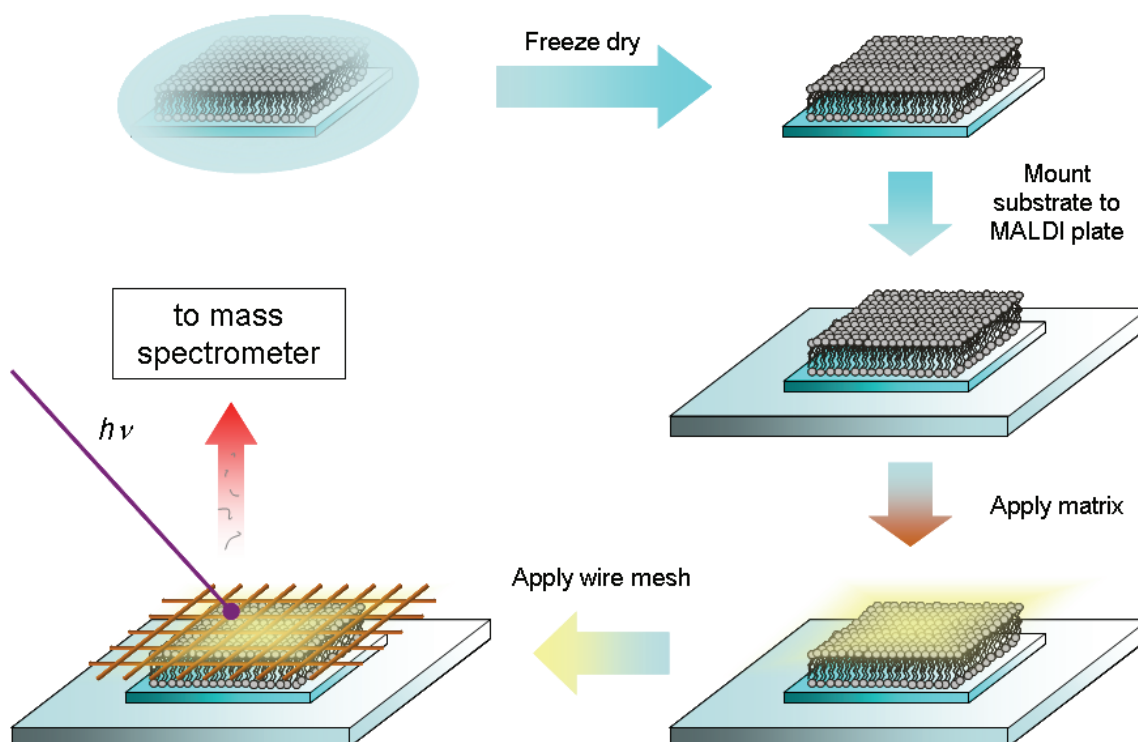


Figure 22. Schematic diagram of the sample preparation protocol used for MS analysis.

Samples were freeze dried, adhered to the MALDI plate, and a matrix aerosol was deposited on the samples. The samples were then analyzed via MALDI-TOF MS following the application of a wire mesh.

Results and Discussion

Initial imaging MS experiments were performed using 5 mol % TR-DHPE (compared to typical 0.1 mol % TR-DHPE), owing to detection limits in the mass spectrometry experiments. Briefly, 5 mol % TR-DHPE corresponds to 3.6×10^8

molecules/ laser spots size, whereas 0.1 mol % TR-DHPE contains 7.1×10^6 molecules/laser spot size. A conservative estimate for the detection limit of the mass spectrometer is $\sim 1.2 \times 10^8$ molecules/laser spot size, therefore the concentration of TR-DHPE needs to be increased for adequate detection by MS. If one considers the sample being analyzed in these experiments, a lipid bilayer, which consists of two monolayers, it is intuitively obvious even for a casual observer that the sample has little depth associated with it; therefore increasing the concentration of the analyte of interest in the bilayer is necessary for mass spectrometry detection.

Initial imaging experiments were aimed at investigating the sample preparation protocol. A lipid matrix bed of POPC was made by the methods described previously followed by the formation of two strips of 5 mol % TR-DHPE, 95 mol % POPC. After freeze drying, the samples were prepared for MALDI and imaged using MS analysis. The data contained in Figure 23B shows a mass specific ion image at m/z 1324.6, which corresponds to $[\text{TR-DHPE} + 2 \text{ Na}]^+$. Two distinct strips of the lipid bilayer contain TR-DHPE. Figure 23A shows a high resolution mass spectrum obtained in the 5 mol % TR-DHPE regions in the bilayer which were identified by the imaging experiment. These experiments confirm that the sample preparation procedure (freeze drying and matrix application) generates analytically informative mass spectral imaging data and does not disrupt (to the extent of our imaging MS spatial resolution) the spatial location of our analytes.

Figure 24A depicts a scheme of the TR-DHPE lipid bilayer electrophoresis experiment. Briefly, a single initial strip of lipid bilayer composed of 5 mol % TR-

DHPE, 95 mol % POPC was formed in a lipid matrix bed of 75 mol % DLPC, 25 mol % cholesterol. Following application of the electric field, two fluorescent bands (TR-DHPE) were observed (see Figure 24A) and attributed to the electrophoretic mobility of the initial bilayer strip across the lipid matrix bed. Earlier work utilizing this separation technique demonstrated that the two isomers of TR-DHPE can be separated into two distinct bands.¹⁰¹ Briefly, there are two possible sulfonyl chloride groups (outlined in blue in Figure 24B) on Texas Red sulfonyl chloride (2, ortho or 4, para) that the lipid molecule can react with during synthesis of TR-DHPE. The separation of these two bands during the electrophoresis experiment can be attributed to the differences in the membrane mobilities of the two isomers. Figure 24B contains two mass specific ion images at m/z 782.5 and m/z 1324.6, corresponding to the ions $[\text{POPC} + \text{Na}]^+$ and $[\text{TR-DHPE} + 2 \text{Na}]^+$, respectively. The MS specific ion image for $[\text{POPC} + \text{Na}]^+$, Figure 24B, top, corresponds to the initial starting position (prior to electrophoresis) of the 95 mol % POPC and 5 mol % TR-DHPE mixture. Since POPC has an overall net neutral charge, it will have no net directional mobility as a result of the applied voltage; however non direction specific diffusion does occur over time and attributes to the observed increase in thickness of the initial starting strip.

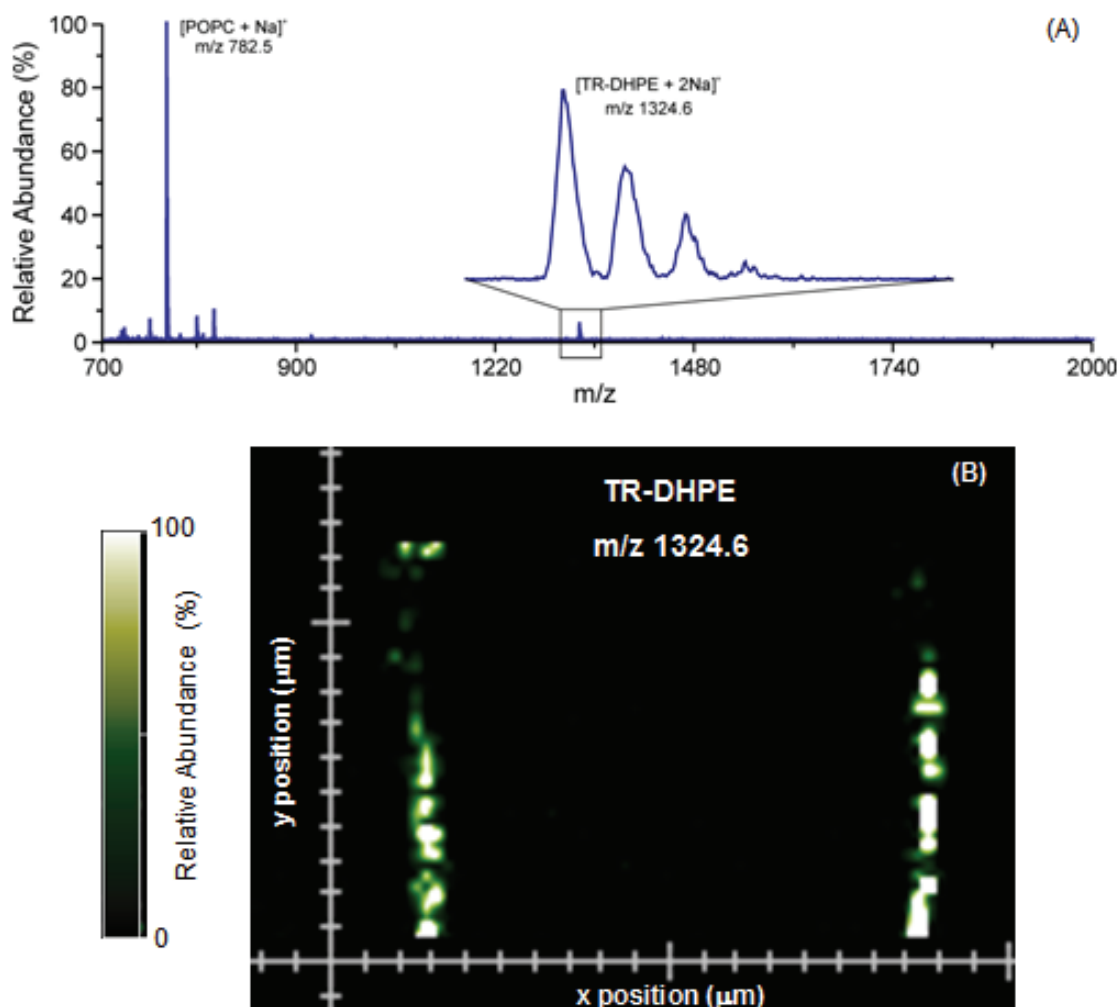


Figure 23. (A) MALDI-TOF mass spectrum obtained from the analysis of a lipid bilayer sample in the TR-DHPE region. (B) MS ion-specific image of m/z 1324.6 for two bilayer strips ($\sim 100 \mu\text{m}$ thick) composed of 5 mol % TR-DHPE lipid bilayer formed by vesicle fusion on a bare portion of substrate in a DLPC lipid matrix. The ion $[\text{TR-DHPE} + 2 \text{Na}]^+$ (m/z 1324.6) is observed in two specific regions in the lipid bilayer.

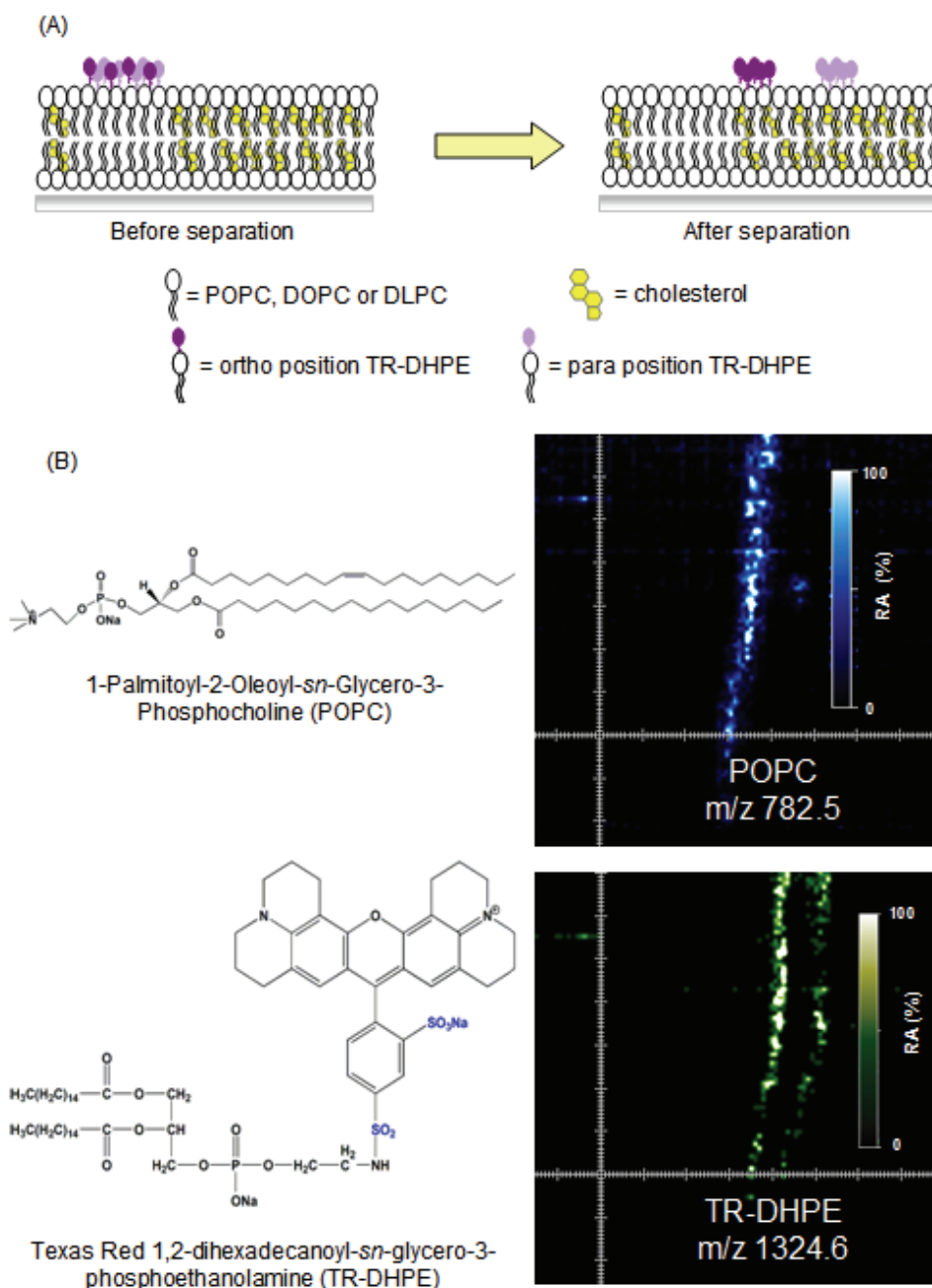


Figure 24. (A) Schematic representation of the method used in the TR-DHPE separation studies. A bilayer strip of 5 mol % TR-DHPE was formed by vesicle fusion on a bare portion of substrate in a DLPC/chol matrix. (B) mass specific ion images at m/z 782.5 ($[POPC + Na]^+$), representing the starting position of TR-DHPE and an ion image of m/z 1324.6 ($[TR-DHPE + 2 Na]^+$), following electrophoresis shows baseline separation of the two TR-DHPE isomers. Structures for both POPC and TR-DHPE are provided to the left of their corresponding MS ion images. TR-DHPE can exist as two stable structural isomers corresponding to ortho and para position.

Figure 24B, bottom corresponds to the location of the structural isomers of TR-DHPE after separation. The TR-DHPE molecules have moved toward the positive electrode away from the initial starting position. The TR-DHPE structural isomers are baseline separated from each other using imaging MS detection. These results illustrate the ability to separate membrane bound species in their native environment following detection by mass spectrometry. Unlike light based imaging techniques, imaging mass spectrometry provides the distribution of multiple analytes across the dimensions of the sample by taking a measurement that is unique for individual target analytes, specifically the analyte's mass-to-charge ratio (m/z) (see Figure 24B). As a result of this type of analysis, multiple images which reveal analyte abundance distributions as a function of spatial position can be obtained in a single experiment. The principle advantage that MS imaging offers over light-based optical imaging techniques is that mass analysis does not require the use of a tag such as a fluorophore. Thus, mass spectrometry provides native state analyte identification on the basis of m/z . Furthermore, imaging MS does not compromise the activity of the analyte of interest because it is an inherent "tagless" technique.¹⁰²

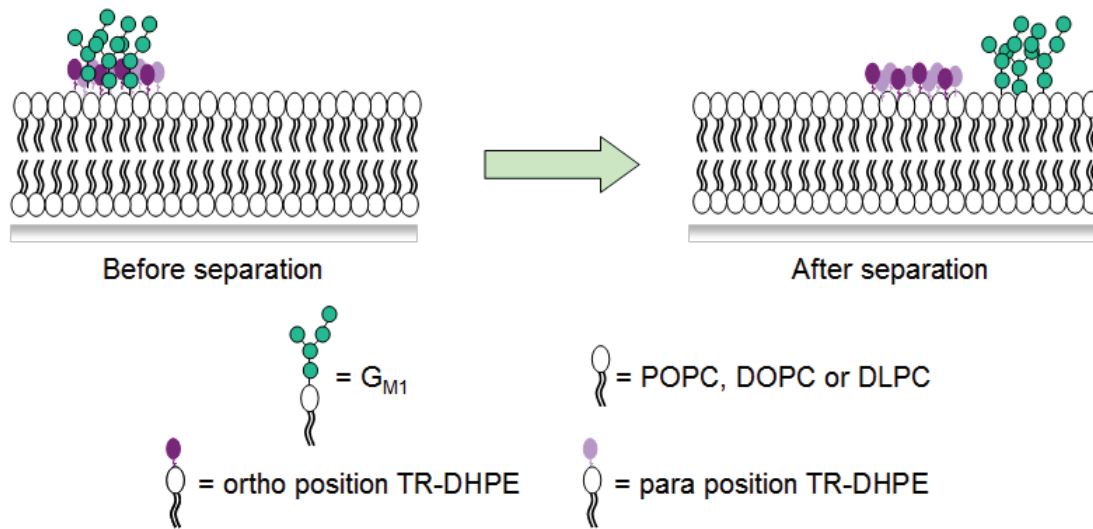


Figure 25. (A) Schematic representation of the method used in the G_{M1} separation studies. A bilayer strip of 5 mol % G_{M1} was formed by vesicle fusion on a bare portion of substrate in a DLPC matrix. An electric potential (100V) was applied longitudinally across the bilayer for ~1 hour. Both glycolipids (G_{M1}) and TR-DHPE migrate toward the positive electrode, due to the net negative charge of each species.

Important biological processes such as receptor-ligand interactions occur on the cell membrane, and the ability to probe these receptors without compromising the receptor-ligand interactions (no labeling interferences) is a key step in understanding these biological processes experimentally in the laboratory. In the following experiments, a receptor (glycolipid) that is not fluorescently tagged is induced to migrate in a lipid bilayer via an applied electric field and detected by imaging MS after migration. In addition to Ganglioside G_{M1} facilitating physiological processes (*e.g.*, facilitates neuron growth) in the brain, this glycolipid also acts as a binding site for

cholera toxin on cell membranes. Cholera toxin is a cytotoxin excreted by *Vibrio Cholerae* and is composed of an A subunit and a pentameric B subunit. Cholera toxin disrupts an organism's nominal physiology by recognizing and binding to the pentasaccharide moiety of G_{M1} located on the cell membrane, which in turn causes severe dehydration, cramps and diarrhea.¹⁰³ The G_{M1} glycolipid is comprised of a pentasaccharide moiety (hydrophilic head) and a ceramide tail (sphingosine and stearic acid). Figure 25 is a schematic drawing of lipid bilayer electrophoresis of G_{M1} , the glycolipid will move towards the positive electrode since it is negatively charged. In these studies, a 100 mol % lipid matrix bed of DLPC was initially formed, followed by a strip of 5 mol % G_{M1} , 0.1 mol % TR-DHPE and 94.9 mol % POPC. Imaging MS data obtained after electrophoresis followed by freeze drying of G_{M1} dehydrate and arrest further diffusional movement is shown in Figure 26. The initial starting position of G_{M1} was located by generating an ion map of DLPC, areas exhibiting a lack of MS ion signal for DLPC (Figure 26, bottom image) suggests the presence of G_{M1} . The MS specific ion images in Figure 26 at m/z 1544.9 and m/z 1572.9 correspond to $[G_{M1}(18:0/d18:1) - H]^-$ and $[G_{M1}(20:0/d18:1) - H]^-$ or $[G_{M1}(18:0/d20:1) - H]^-$, respectively. The mobility of the glycolipids do not differ in the bilayer, however owing to their differing m/z values it is possible to obtain two MS specific ion images by monitoring the m/z representative of each species. In nature, three different ceramide contents for G_{M1} are observed, the most abundant ceramide tail at 70% is $G_{M1}(18:0/d18:1)$, followed by minor contributions from both $G_{M1}(20:0/d18:1)$ (25%) and $G_{M1}(18:0/d20:1)$ (5%). Interesting to note are the relative abundance values observed in our mass spectrometry experiments for

$[G_{M1}(18:0/d18:1)-H]^-$ to $[G_{M1}(20:0/d18:1)-H]^-$ or $[G_{M1}(18:0/d20:1)-H]^-$ is $\sim 68:32$, these ratios are very similar to the estimated natural abundance values (70:30). The results obtained by mass spectrometry imaging of electrophoretically migrated G_{M1} illustrate the ability to discern spatial information of a non-labeled glycolipid (receptor)—results which are not observed in fluorescent experiments.

The ability to use imaging MS to probe membrane proteins and peptides (both transmembrane and peripheral) in a lipid bilayer can greatly enhance our understanding of peptide/protein processes which occur at the cell membrane. Preliminary peptide experiments consist of constructing a supported lipid bilayer of two strips incorporating a peptide (3 mol % melittin, 96.9 mol % DOPC and 0.1 mol % TR-DHPE) in a 100 mol % POPC lipid matrix bed. Figure 27 illustrates the MS specific ion image at m/z 2845.8 which corresponds to $[\text{melittin} + H]^+$ and a mass spectrum obtained in the melittin regions identified in the bilayer. Two distinct strips of melittin are observed, suggesting that melittin is incorporated within the bilayer. Further studies will be aimed at using imaging MS to probe peptide migration (or lack thereof) in a lipid bilayer after an electric field is applied. Ultimately, lipid bilayer electrophoresis may offer the ability to separate membrane proteins in their native environment, followed by label-free detection using MS. Combining both techniques eliminates the complexity of the cell membrane and the need for fluorophore labels.

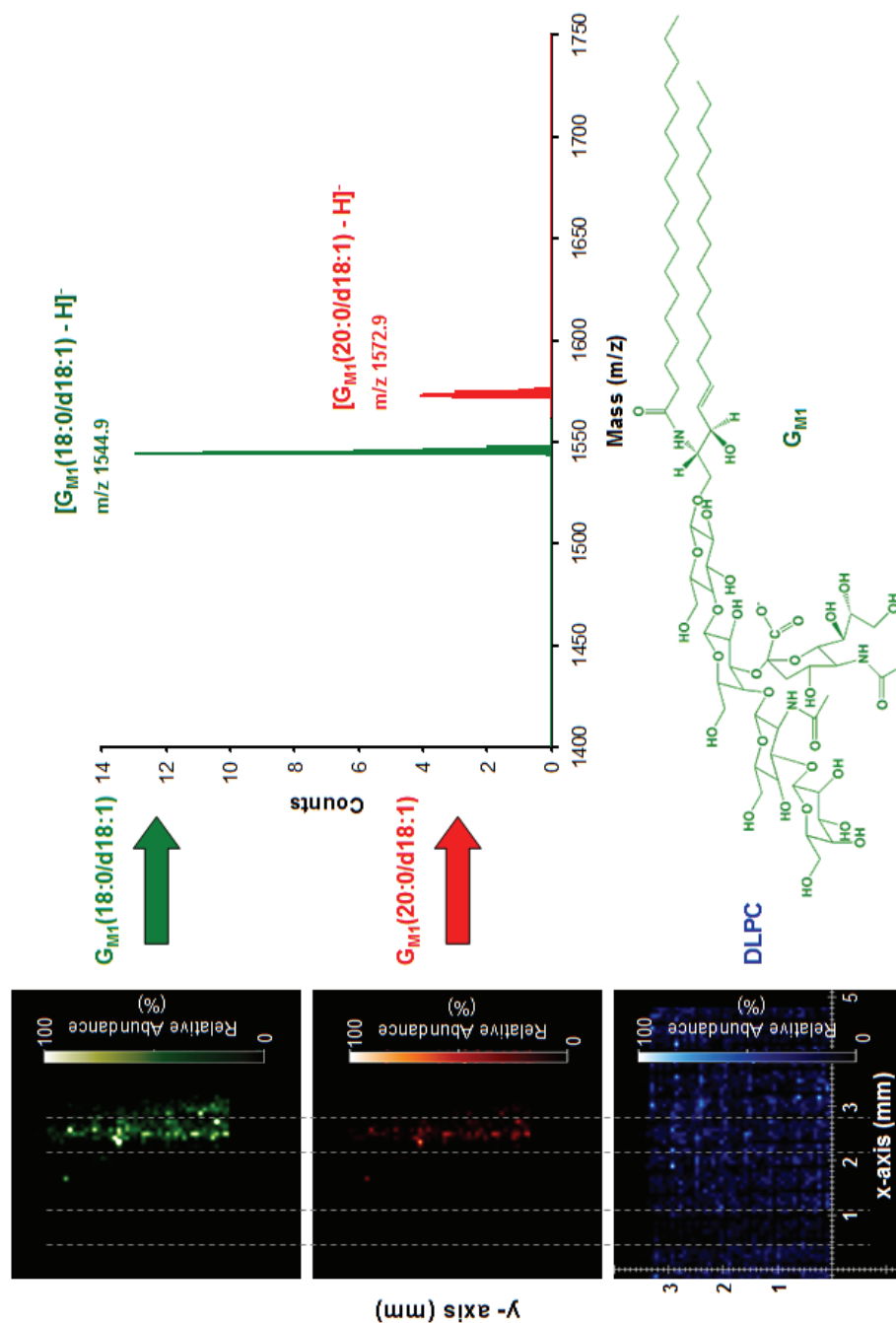


Figure 26. (left) MS ion-specific images for (top) G_{M1} (18:0/d18:1), (middle) G_{M1} (20:0/d18:1) and (bottom) $DLPC$. The MS ion images suggest that both G_{M1} (18:0/d18:1) and G_{M1} (20:0/d18:1) move ~ 1.5 mm away from their original starting position (no $DLPC$ ion signal is observed). (right) MALDI-TOF mass spectrum (negative mode) obtained from the analysis of the lipid bilayer sample in the G_{M1} region. The structure for G_{M1} (18:0/d18:1) is also provided.

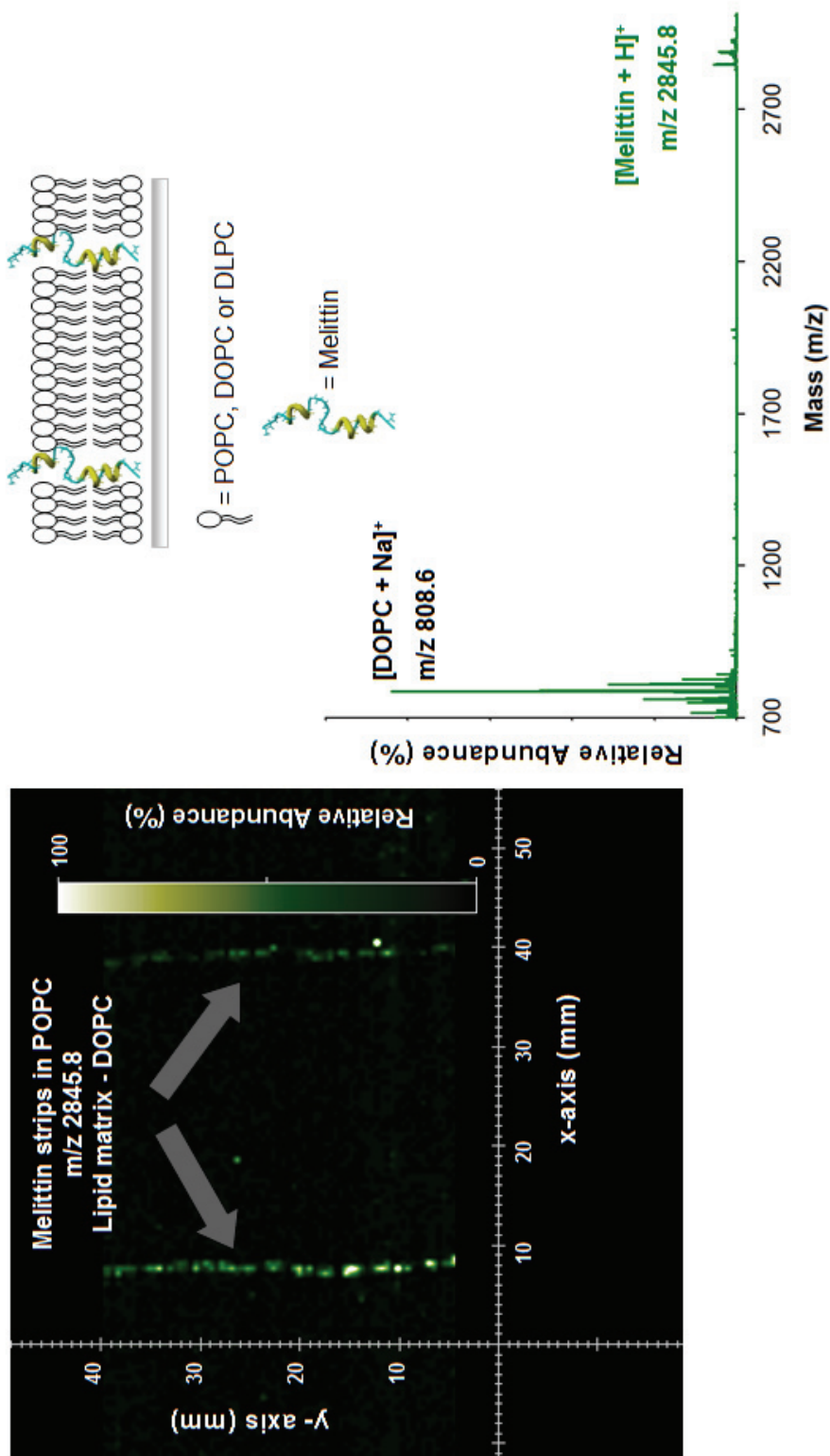


Figure 27. (left) MS ion-specific images for [Melittin + H]⁺ (m/z 2845.8) of two bilayer strips (~100 μm) of 3 mol % melittin formed by vesicle fusion on a bare portion of substrate in a DOPC matrix. [Melittin + H]⁺ is observed in two specific regions in the lipid bilayer. (right) MALDI-TOF mass spectrum obtained from the analysis of the lipid bilayer sample in the melittin strip region.

Conclusion

Proof-of-concept studies are presented which demonstrate mass spectrometry imaging of species that are electrophoretically separated in a lipid bilayer using an electric field. Initial studies characterized the imaging MS technique using fluorescently labeled membrane bound species; later work consists of imaging receptors and peptides in lipid bilayers. Imaging MS offers both label-free and multiple analyte detection in single experiments, these advantages allow the integrity of the membrane component to be conserved (*i.e.*, no label). The ability to use a lipid bilayer as a separation medium followed by mass spectrometry imaging is expected to have an impact on the analysis of cell membranes. Specifically, it may be possible to monitor cell membranes for important biological processes such as the formation and chemical composition of lipid rafts or whole cell membranes.

CHAPTER VI

SILVER NANOPARTICLES AS SELECTIVE IONIZATION PROBES FOR MASS SPECTROMETRY*

Laser desorption/ionization (LDI) using silver nanoparticles (AgNPs) is shown to selectively ionize olefinic compounds, *e.g.*, cholesterol, 1-palmitoyl-2-oleoyl-*sn*-glycero-3-phosphocholine (POPC), and carotenoids. Selective AgNP LDI can be carried out from complex mixtures without the addition of an organic matrix, sample cleanup or prefractionation. Results presented in this report are the first to demonstrate the selective ionization of specific compounds from a complex mixture using metal nanoparticles. The ability to selectively ionize specific chemical species using a sample preparation that introduces minimal chemical noise is especially relevant to imaging MS, where analysis often requires searching for specific analytes, such as steroids (specifically cholesterol) or vitamins, in complex mixtures.

*Parts of this chapter are reprinted with permission from *Analytical Chemistry*, Volume 80, Stacy D. Sherrod, Arnaldo J. Diaz, William K. Russell, Paul S. Cremer and David H. Russell, Silver Nanoparticles as Selective Ionization Probes for Mass Spectrometry, pages 6796–6799, 2008. Copyright [2008] American Chemical Society.

Introduction

Recently, there has been growing interest in using nanomaterials to facilitate laser desorption/ionization (LDI) of a broad range of molecules, owing to their unique physicochemical properties.¹⁰⁴⁻¹¹⁵ LDI using nanoparticles (NPs) differs from matrix assisted laser desorption/ionization (MALDI) in several ways: (i) less complicated mass spectra in the low mass region owing to a decrease in matrix derived chemical noise (matrix ions and adducts),¹¹³ (ii) flexible and relatively simple sample preparation conditions,¹⁰⁵ (iii) a higher tolerance to specific chemical additives, such as those commonly used in biological analysis (*e.g.*, surfactants),¹⁰⁶ (iv) the ability to tailor the chemical properties of NPs using relatively simple derivatization schemes,¹¹² which can be exploited to (v) modify NPs (metal and silicon based) to selectively capture and ionize analytes on the basis of specific chemical properties (*i.e.*, functional groups).^{105,116-120}

Several laboratories have demonstrated that substrate-selective binding strategies can be implemented by treating the modified substrate with a solution containing the analyte of interest, washing the substrate and then applying an organic matrix prior to analysis by mass spectrometry (MS). For example, Vachet and coworkers utilized mixed monolayer-protected gold nanoclusters to selectively extract and concentrate peptides from dilute solutions.¹¹⁷ Shen, Brockman, and Teng prepared monolayers on gold nanomaterials that are modified to interact with specific molecules, *i.e.*, oligohistidine-tagged peptides and proteins,¹²¹ hydrophobic peptides,¹²² and charged biomolecules;¹¹⁸ however, all of these methods require the use of traditional MALDI matrices. On the

other hand, Hua and coworkers have utilized ~160 nm silver nanoparticles to ionize peptides from samples containing large amounts of surfactant,¹⁰⁶ and Lin and coworkers utilized bifunctionalized metal nanoparticles, having both a probe protein and organic matrix component, for solid-phase extraction and ionization of mannose from human plasma samples.¹¹⁶ These studies illustrate the utility for functionalized nanomaterials to capture and sequester specific molecules and/or remove unwanted salts, chemicals, biomolecules and/or polymers from samples prior to MS analysis.

The ability to control the size, composition and electronic properties of nanoparticles provides a means for selective capture and/or ionization of important molecules of a broad range of samples. Previously, we reported that gold nanoparticles can be used to selectively ionize phosphotyrosine over phosphoserine or phosphothreonine containing peptides without the need for an organic matrix or sample cleanup,¹⁰⁵ and we attributed this effect to π -cation interactions between tyrosine and the metal nanoparticle. Here, we exploit the Ag-olefin interaction to selectively ionize specific carotenoids, a sterol and a lipid from complex mixtures in the presence of AgNPs *without additional washing or extraction procedures*. Because many classes of molecules contain olefins (*e.g.*, flavanoids, lipids, vitamins, carotenoids, tocopherols, drugs, etc.), the ability to characterize such compounds is of considerable importance. The Ag-olefin interaction has long been used for chemical analysis. For example, Ag-olefin interactions enhance Ag cationization by electrospray ionization,¹²³⁻¹²⁶ facilitate olefin transport in supported membranes,¹²⁷ as well as separate and quantitate lipids, fatty acids, and triacylglycerols.¹²⁸⁻¹³¹ Moreover, thin silver films have been used to

image cholesterol in thin tissue sections of rat kidneys¹³² and polymorphonuclear leucocytes.^{133, 134}

Experimental Section

Materials. All peptides (P60, P60 phosphorylated, Bradykinin 1-8, [Val⁴] Angiotensin III, Flag, Angiotensin II, Bradykinin, Angiotensin I, Substance P and ACTH (18-39)) were purchased from American Peptide (Sunnyvale, CA) and used without further purification. Cholesterol and 1-palmitoyl-2-oleoyl-*sn*-glycero-3-phosphocholine (POPC) were acquired from Avanti Polar Lipids (Alabaster, AL). Other chemicals/nanoparticles used in these studies were from the following commercial sources: 20 nm and 60 nm silver colloids (Ted Pella, Inc., Redding, CA), 2,5-dihydroxybenzoic acid (DHB) (Aldrich Chemicals, Milwaukee, WI), and silver nitrate (Aldrich Chemical, Milwaukee, WI). Although our previous work illustrates different results can be obtained utilizing 2, 5, and 10 nm gold NPs, we do not observe differences in our data when using 20 nm or 60 nm AgNPs. Freshly squeezed carrot juice was received as a gift from Jamba Juice Company (College Station, TX).

Sample Preparation. The small unilamellar vesicles employed in these studies were composed of POPC and cholesterol.⁹⁷ To prepare these vesicles, the appropriate components (POPC with 5 mol % cholesterol) were first dissolved together in chloroform, dried under a stream of dry nitrogen, and desiccated under vacuum (10^{-3} Torr) for approximately 4 hours. After desiccation, the dried lipids and cholesterol were rehydrated in phosphate buffer saline (PBS) solution (pH 7.4) and subjected to ten

freeze/thaw cycles by alternating between rapid immersion in liquid nitrogen followed by immersion in a 30°C water bath. The small unilamellar vesicle solution was then extruded 5 times through a polycarbonate filter (Whatman) containing 50 nm pores to produce vesicles of uniform size.

Stock solutions of individual peptides were dissolved in deionized water (18 MΩ, Barnstead, Dubuque, IA) at 1 mg/mL. The peptide mixture solution was prepared by mixing peptides together such that each peptide concentration was between 300-700 pmol/μL. The silver-matrix solution (20 mg/mL DHB in 50/50, v/v, ethanol/120μM AgNO₃ with 0.1% TFA) was mixed 10/1/1 (v/v/v), matrix: peptide mixture: vesicle solution, respectively. The AgNP solution (diluted 4/1, v/v, ethanol/NP solution) was mixed 10/1/1 (v/v/v), NPs: peptide mixture: vesicle solution. For the freshly squeezed carrot juice experiments, the AgNPs were spun down for 20 minutes at 7,000 rpm followed by resuspension in methanol. The AgNPs solution (in MeOH) was mixed 10/1 (v/v), NP solution: carrot juice. 1 μL of each sample solution was spotted onto the sample plate and dried *in vacuo*.

LDI and MALDI MS analysis. All MS experiments were performed on a Voyager DE-STR instrument (Applied Biosystems, Foster City, CA) under optimized conditions in reflected mode utilizing a nitrogen laser at 337 nm. Tandem MS experiments were performed using a 4800 Proteomics Analyzer MALDI TOF/TOF (Applied Biosystems, Foster City, CA). Collision-induced dissociation tandem MS spectra were acquired using air as the collision gas (medium pressure, 4.0×10^{-7} Torr) with a 1 kV collision energy.

Results and Discussion

Figure 28 shows a UV-Vis spectrum of the 20 nm silver nanoparticles in H₂O, in which a characteristic surface plasmon resonance (SPR) band is centered at 412 nm. The peak centered on 412 nm is due to the oscillation of the electrons in the conduction band in the silver nanoparticles, suggesting the solution does contain AgNPs.

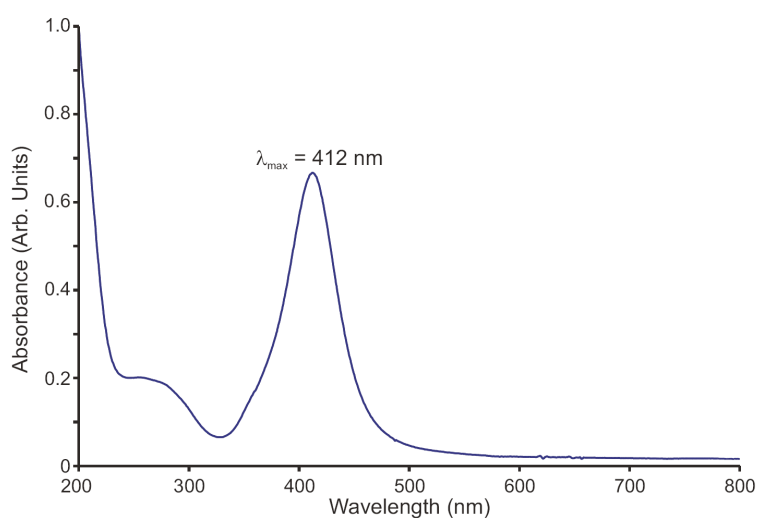


Figure 28. UV-Vis solution-phase absorption spectrum of 20nm AgNPs. The surface plasmon band is centered around 412 nm.

The preference for silver binding to olefins is governed by the number, position, and configuration of the double bonds in the target molecule.^{128, 135} The Dewar model describes the Ag^+ -olefin interaction in terms of a σ bond between the free s-orbital of Ag^+ and the olefinic π -orbital and likewise a π -bond is formed by the interaction of the filled d -orbitals of the silver ion and the vacant antibonding π -orbitals of the carbon-carbon double bond. The extent of interaction between overlapping orbitals affects the strength of the Ag^+ -olefin interaction; therefore, steric factors have a pronounced effect on the strength of interaction. For example, (i) less substituted double bonds tend to form more stable complexes with Ag^+ , (ii) *cis* conformations will form more stable complexes than *trans*, (iii) longer hydrocarbon alkene chains are less stable than shorter chains, and (iv) delocalization of electron density, *i.e.*, aromaticity, weakens the interaction.¹³⁶

The data contained in Figure 29 illustrate selective ionization of cholesterol and the lipid, POPC, using 20 nm AgNPs. The sample consists of a mixture of ten peptides, POPC and cholesterol (see Table 3), which was analyzed by LDI MS using a mixed matrix composed of DHB and silver nitrate (Figure 29 A) and only AgNPs (Figure 29B). The MALDI mass spectrum contains ion signals corresponding to all 12 species present in the mixture.

Note that the only cholesterol ion observed in the MALDI spectrum involves a neutral loss of water, specifically $[\text{cholesterol} - \text{H}_2\text{O} + \text{H}]^+$ ion (m/z 369.3), and the intact species $[\text{cholesterol} + \text{Ag}]^+$ is not observed. Conversely, the mass spectrum of the same 12 component mixture ionized using AgNPs contains ion signals corresponding to silver clusters (Ag_2^+ and Ag_3^+ , m/z 213.8 and 320.7, respectively), $[\text{cholesterol} + \text{Ag}]^+$ (m/z 493.3) and $[\text{POPC} + \text{Ag}]^+$ (m/z 866.8). Note also that $[\text{M} + \text{Na}]^+$ ions are not observed in the mass spectrum for AgNPs, even though there is a high salt concentration (~ 60 mM). LDI spectra of samples that are not treated with AgNP or organic matrix contain no discernable signal above background. Although Hua *et. al.* reported that LDI using ~ 160 nm AgNPs facilitates ionization of peptides, we do not observe ion signals for peptides using 20 nm or 60 nm AgNPs.¹⁰⁶ Quite possibly these differences in peptide ionization efficiencies from AgNP can be attributed to nanoparticle size effects. For example, we previously reported nanoparticle size dependent ion yields for peptides using AuNPs, and we have found that the presence of various salts (especially oxyanions), trace amounts of organics (various alcohols, glycerol, and surfactants), as well as particle size strongly influence LDI ion yields.^{105, 137}

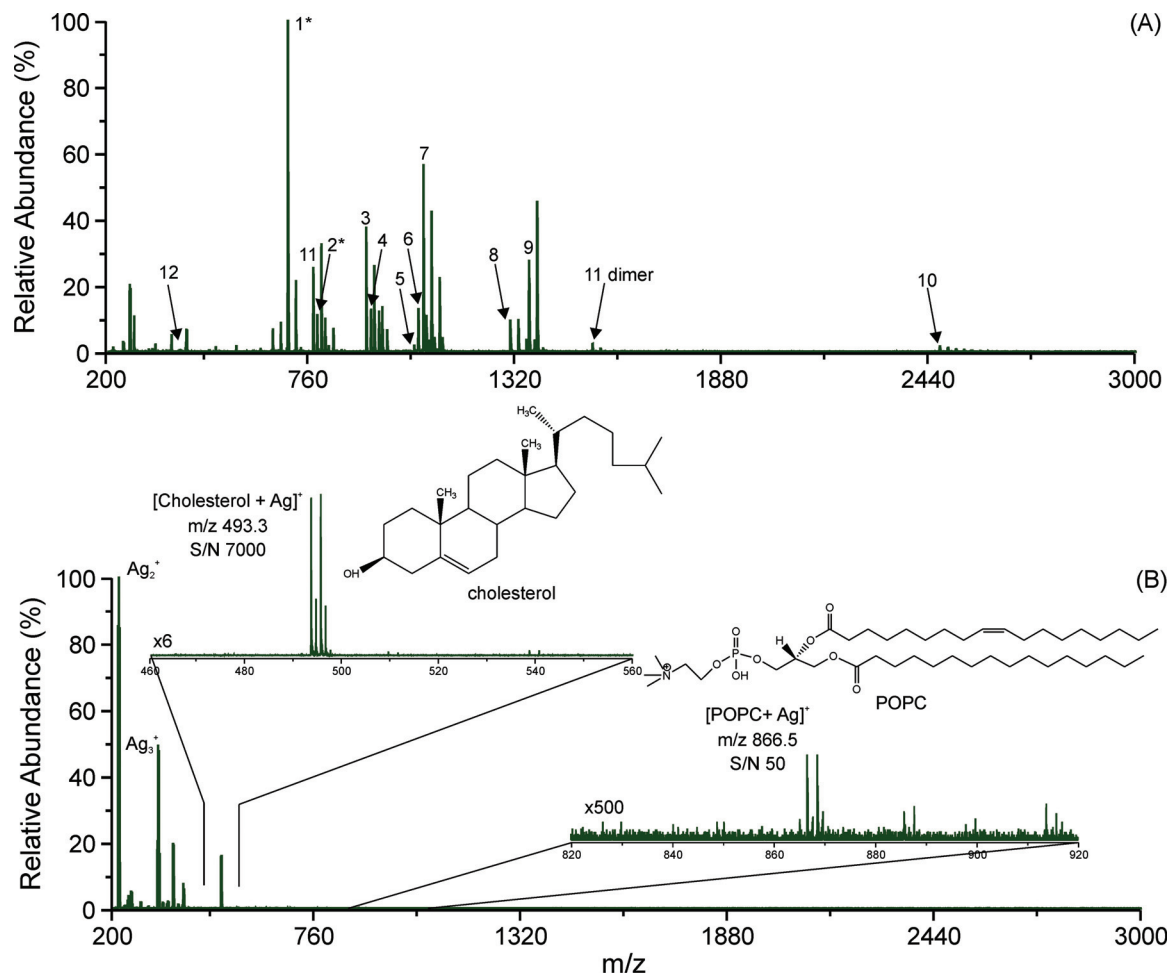


Figure 29. MALDI time-of-flight mass spectra of the 12 component mixture obtained using (A) DHB with 120 μM AgNO_3 and (B) 20nm AgNPs. The $[\text{M} + \text{H}]^+$ or $[\text{M} + \text{Na}]^+$ (denoted by a “*”) ions of each peptide is numbered in the spectrum and identified in Table 3. A high abundance of $[\text{M} + \text{Na}]^+$ ions (unlabeled peaks) are observed owing to the PBS buffer used to prepare the small unilamellar vesicles. Structures for both cholesterol and POPC are provided.

We interpret these results as evidence that the addition of the AgNPs facilitates selective ionization of cholesterol and POPC from the 12 component mixture. In addition to demonstrating the preference for silver to complex with olefinic bonds,¹²⁸ the data suggest a preference for forming $[M + Ag]^+$ ions of cholesterol over POPC (as indicated by the high relative abundance and signal to noise values of the cholesterol signal compared to that of POPC, see Figure 29). This observation is consistent with the Dewar model. That is, the ring restricted double bond in cholesterol is likely more accessible than is the double bond of POPC, which is surrounded by freely rotating long hydrocarbon chains. Table 3 summarizes the ion signals observed in the spectra contained in Figure 29, and the observed m/z signals of the species detected in the sample mixtures which utilized both the silver doped MALDI matrix and AgNPs.

Table 3. List of peptides, lipid and sterol in the 12 component mixture.

List of peptides, lipid and sterol in the 12 component mixture.				
Peptide(p)/Lipid(l)/Sterol(s)	peptide sequence/ chemical composition	matrix obsd m/z	AgNPs obsd m/z	amount spotted on plate (pmol)
1 P60* (p)	Ac-IYGEF-NH ₂ ^{a,b}	690.7	----	62.3
2 P60 phosphorylated* (p)	Ac-IpYGEF-NH ₂ ^{a,b}	770.8	----	55.6
3 Bradykinin 1-8 (p)	RPPGFSPF	904.0	----	46.1
4 [Val ⁴] Angiotensin III (p)	RVYVHPF	917.1	----	45.4
5 Flag (p)	DYKDDDDK	1013.0	----	41.1
6 Angiotensin II (p)	DRVYIHPF	1046.5	----	39.8
7 Bradykinin (p)	RPPGFSPFR	1060.6	----	39.3
8 Angiotensin I (p)	DRVYIHPFHL	1296.7	----	32.1
9 Substance P (p)	RPKPQQFFGLM-NH ₂ ^b	1347.7	----	30.9
10 ACTH (18-39) (p)	RPVKYPNGAEDSAEAFPLEF	2465.7	----	16.9
11 16:0-18:1 Phosphocholine (l)	C ₄₂ H ₈₃ NO ₈ P	760.6	[M+Ag] ⁺ 866.5	274.2
12 Cholesterol (s)	C ₂₇ H ₄₆ O	[M-H ₂ O+H] ⁺ 369.4	[M+Ag] ⁺ 493.3	12.9
^a Ac = Acetylated ^b NH ₂ = Amidated * = only [M+Na] ⁺ species observed				

Selective ionization of olefins using AgNPs is also illustrated by analysis of freshly squeezed carrot juice (Figure 30). Although carrot juice is a complex mixture composed of vitamins, minerals, terpenoids, lipids, carbohydrates, sugars, proteins, carotenoids, and amino acids,¹³⁸ the AgNP LDI spectrum contains relatively few ion signals, whereas the MALDI mass spectrum is congested (Figure 30). In the region of interest, only two signals are observed in the AgNP LDI spectrum, these signals correspond to a carotenoid and a carotenoid precursor, specifically $[\beta\text{-carotene} + \text{Ag}]^+$ and $[\text{phytoene} + \text{Ag}]^+$, m/z 643.3 and 651.4, respectively. These assignments were validated using collision induced dissociation (MS/MS) of the parent ions. Specifically the characteristic fragment ion $[\beta\text{-carotene} - 92 + \text{Ag}]^+$ was observed for β -carotene and two predominate fragment ions, $[\text{C}_5\text{H}_9 + \text{Ag}]^+$ and $[\text{C}_{10}\text{H}_{17} + \text{Ag}]^+$, were observed for the phytoene ion (Figure 30, inset).^{139, 140} The Ag^+ affinity towards olefinic bonds is further supported by results obtained for pure samples of amphotericin B (m/z 1030.4), folic acid (m/z 548.0), and β -carotene (m/z 643.3) (Figure 31). The ion signals observed for these analytes consists exclusively of the $[\text{M} + \text{Ag}]^+$ ion.

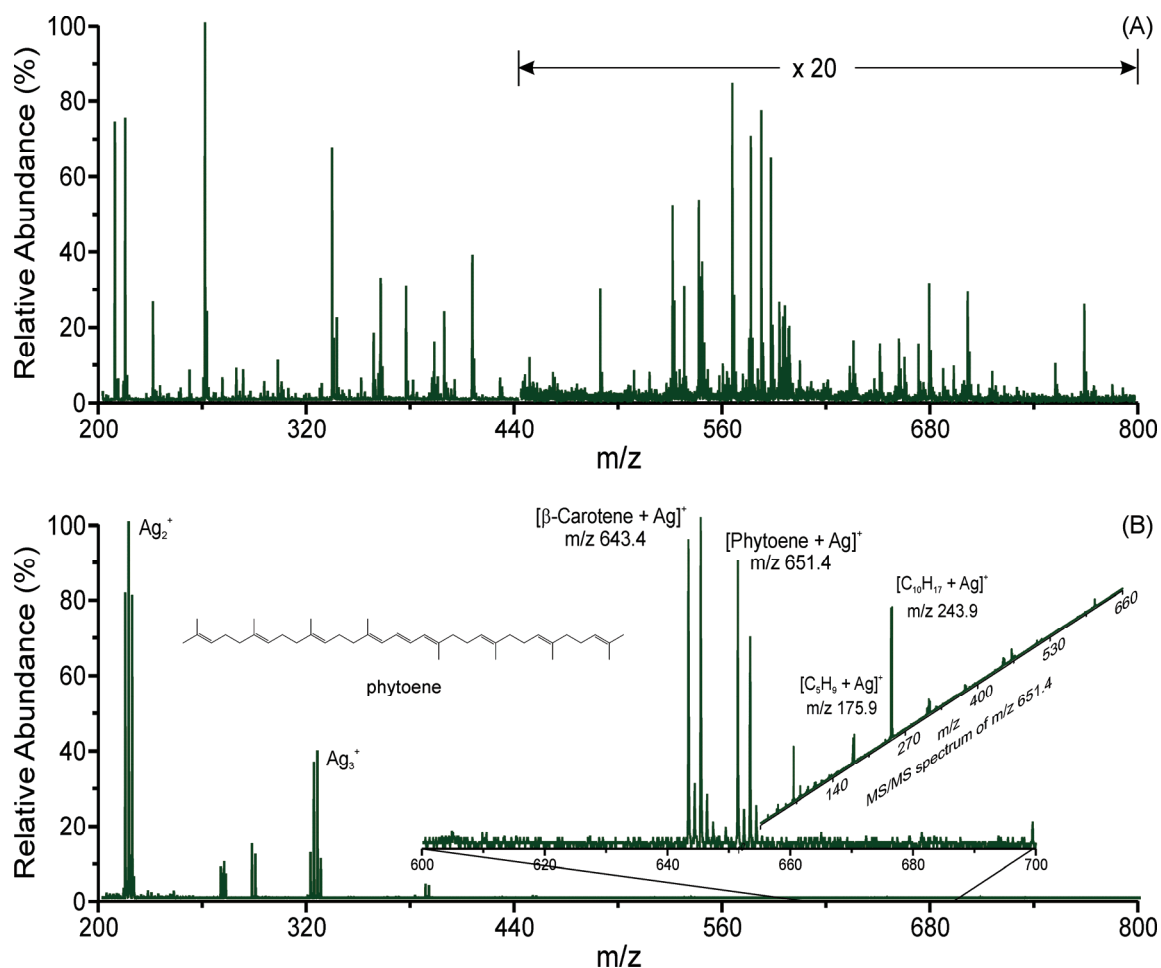


Figure 30. (A) MALDI time-of-flight mass spectrum of freshly squeezed carrot juice obtained using DHB. (B) LDI time-of-flight mass spectrum of freshly squeezed carrot juice obtained using 20 nm AgNPs. $[\text{M} + \text{Ag}]^+$ ions of β -carotene and phytoene are observed in the mass spectrum. The inset contains the tandem MS spectrum for the phytoene ion with the two predominate fragment ions, $[\text{C}_5\text{H}_9 + \text{Ag}]^+$ and $[\text{C}_{10}\text{H}_{17} + \text{Ag}]^+$, labeled in the spectrum. The structure for phytoene is provided.

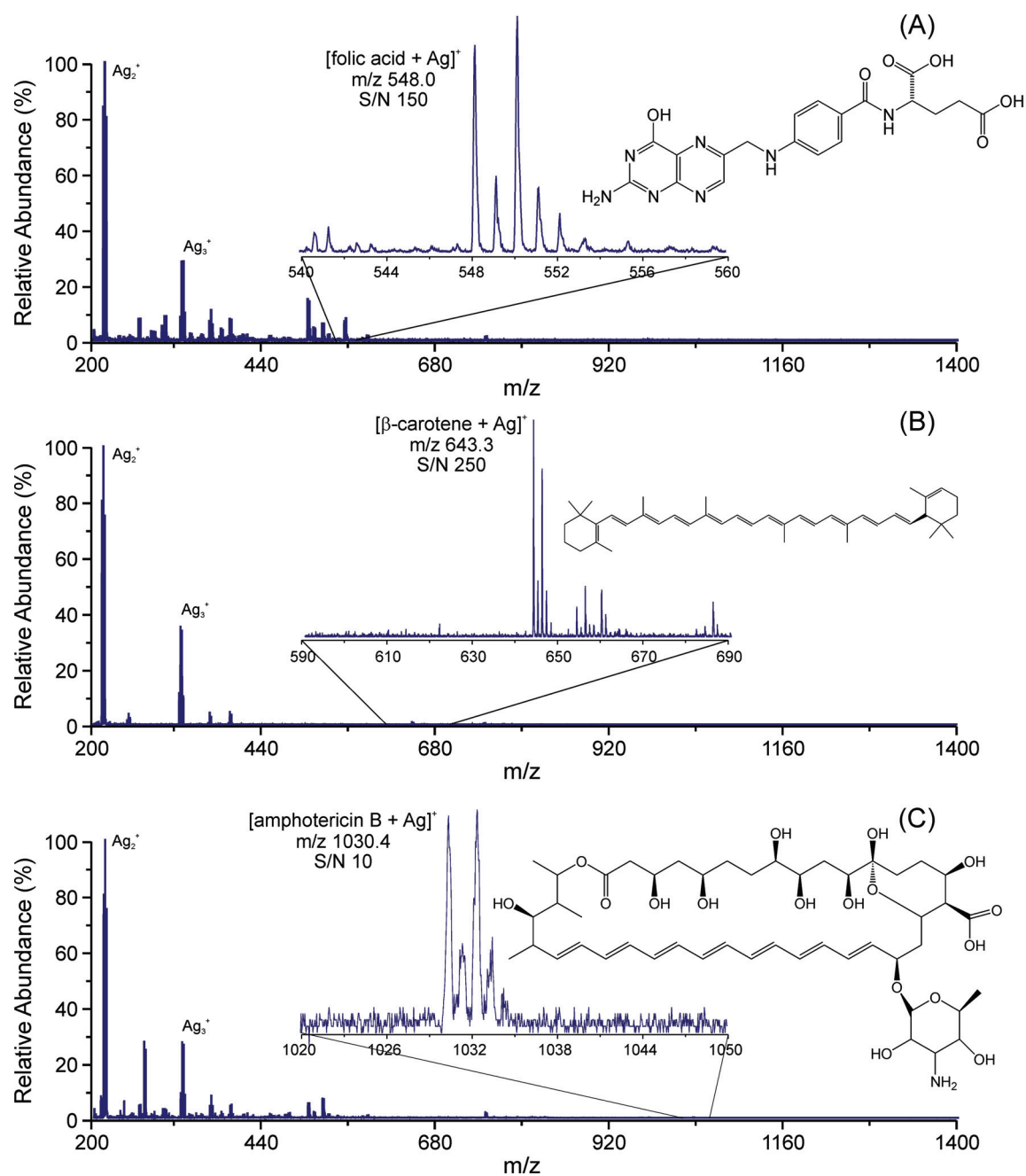


Figure 31. 20 nm AgNP LDI time-of-flight mass spectra of (a) folic acid (b) β -carotene and (c) amphotericin B. The $[\text{M} + \text{Ag}]^+$ ion of each species is observed and the structure for each olefin is provided.

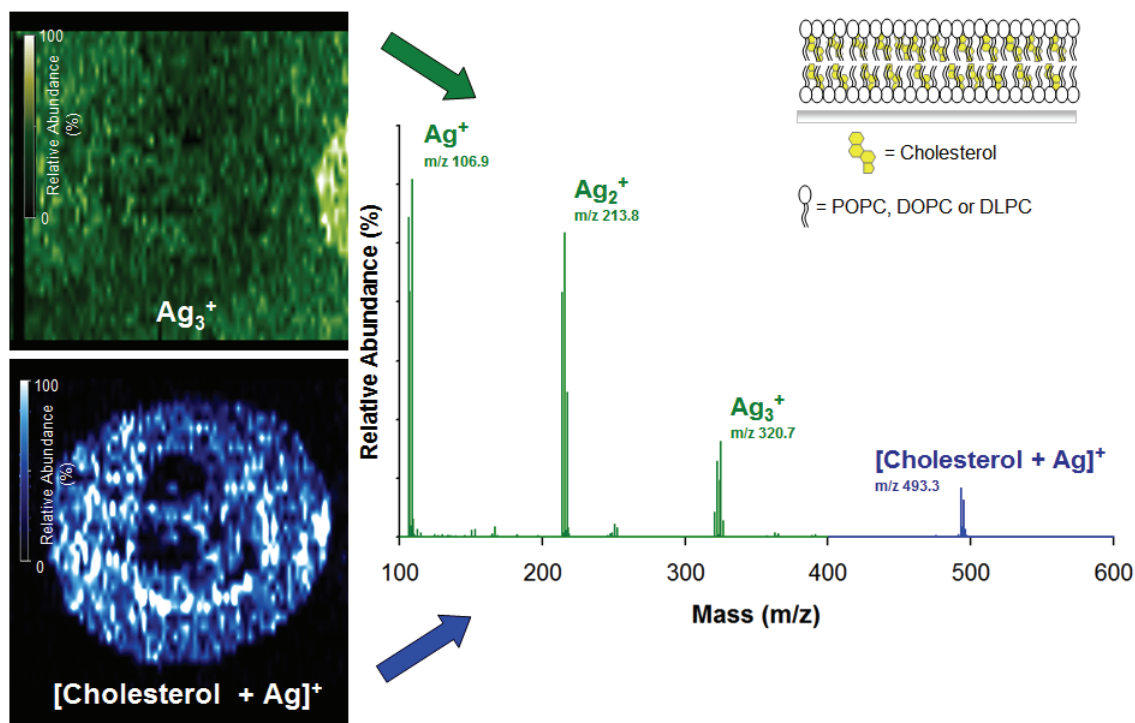


Figure 32. (left) MS ion-specific images for (top) Ag_3^+ (m/z 320.7), and (bottom) $[\text{cholesterol} + \text{Ag}]^+$ (m/z 493.3). The MS ion images illustrate the selective ionization of cholesterol in a lipid bilayer. AgNPs were electrosprayed on a freeze dried lipid bilayer surface containing 5 mol % cholesterol. (right) typical AgNP LDI mass spectrum observed in the cholesterol regions of the sample.

Conclusion

We have successfully utilized 20 nm and 60 nm AgNPs to facilitate the ionization of analytes which contain olefins. To illustrate this point, cholesterol and POPC were selectively ionized from a 12 component mixture, and the data suggest that silver shows preferential binding with cholesterol over POPC. Also, two carotenoids, β -carotene and phytoene, were selectively ionized from a sample of carrot juice using AgNPs. These results demonstrate the ability to use AgNPs to selectively ionize cholesterol, POPC, β -carotene and phytoene from complex mixtures. The ability to selectively ionize specific chemical species using a sample preparation that introduces minimal chemical noise is especially relevant to biomarker detection or imaging MS (see

Figure 32), where analysis often requires searching for low-abundance analytes, such as steroid or vitamin analysis, in complex mixtures. Designing other metal or mixed-metal NPs to observe similar selectivity trends are currently being explored. For example, metals (*i.e.*, Cu(II), Ni(II), Zn(II), Co(II), Fe(III), Ga(III), etc.) that are typically used to separate proteins and peptides could be used for selective ionization.¹⁴¹⁻¹⁴³ Tailoring the chemical composition of NPs towards binding specific chemical species provides many avenues to utilize known chemical interactions for compound specific LDI-MS.

CHAPTER VII

A MULTI-ANODE DETECTION SCHEME FOR INCREASED RESOLUTION AND SENSITIVITY IN TOFMS

State-of-the-art TOFMS detection techniques rely on signal amplification and current integration and/or ion counting detection. Most MS instruments utilize a *single* anode for detection, which simplifies the detector assembly and associated electronics. There are, however, advantages to using several discrete anodes, these include: increased sensitivity, ability to obtain spatial information using position-sensitive detection, and increased mass resolution by effectively aperturing the size of the detector to individual anode dimensions. We have modified a Voyager Elite XL (6.6-meter) MALDI-TOF instrument to incorporate a position-sensitive, multi-anode (8) detection system. This work focuses on results from recent experiments to evaluate the performance of new data acquisition strategies.

Instrumental and Experimental Design

Position sensitive detection studies were carried out using a modified Voyager Elite XL reflectron MALDI-TOF MS shown in Figure 33. Upon ionization of the sample, ions are accelerated to a constant kinetic energy after a short delay time (generally, ns). The ions then enter the field-free drift region where they are separated based on their mass-to-charge (m/z) ratio. The TOF mass analyzer allows m/z separation according to the following equation:

$$v = \sqrt{\frac{2KE}{m/z}} \quad (3)$$

Because all ions are accelerated to the same kinetic energy (KE), the velocity (v) of each ion is inversely proportional to the square root of its m/z . The voltages applied to the sample source are chosen so that ions with the same m/z are focused spatially at the entrance of the reflectron. The reflectron is designed for first-order energy focusing, *i.e.* ions with higher kinetic energies will penetrate deeper into the reflectron before the ions are deflected back towards the detector (see Figure 33). As a result, the more energetic ions will reach the detector at the same time as the slower ions of the same mass.⁵⁶

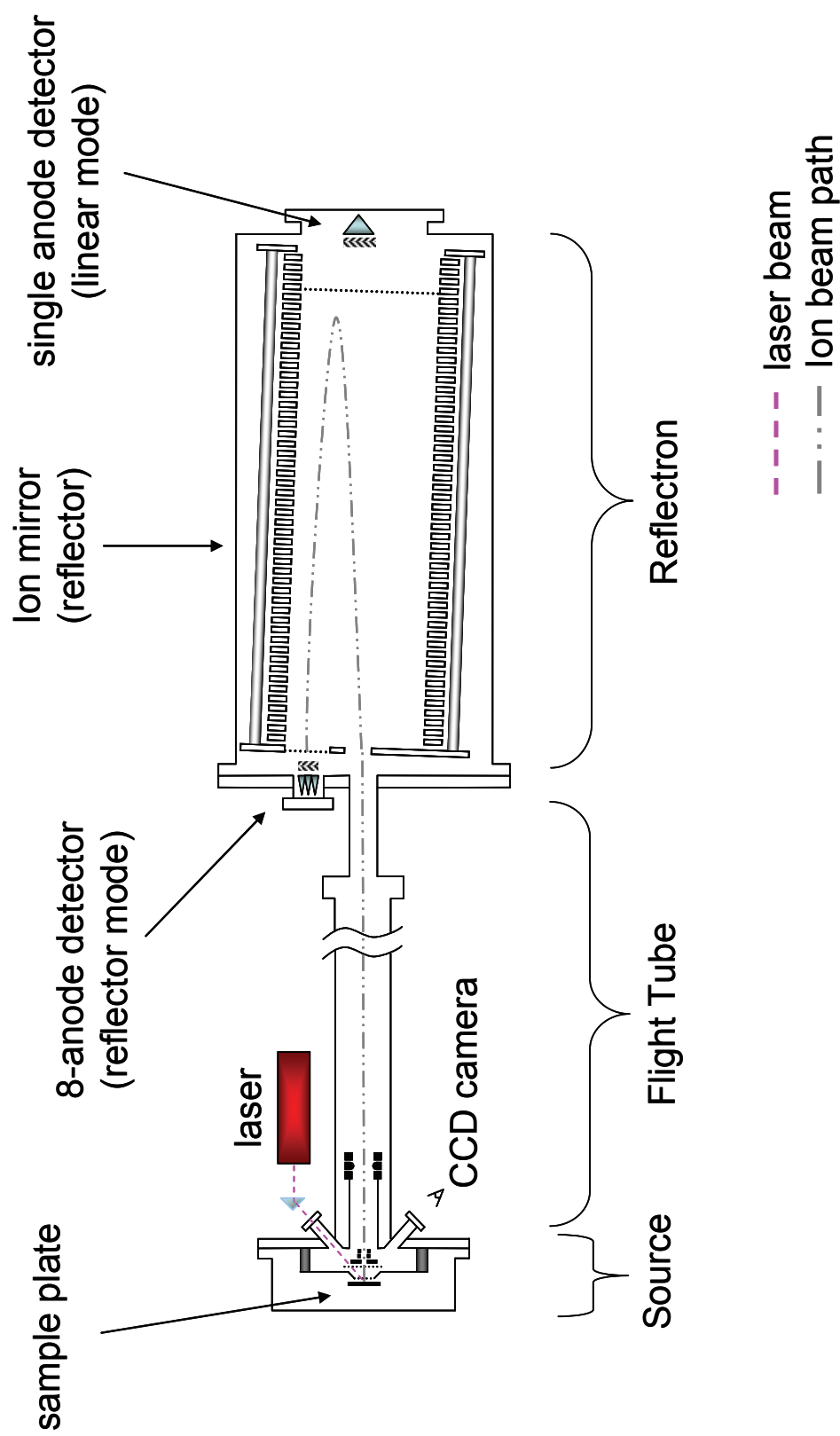


Figure 33. Schematic diagram of instrumentation used for position sensitive detection studies.

Resolution

In TOFMS the resolution of the instrument is defined by:

$$R = \frac{t}{2\Delta t} \quad (4)$$

where t is the analyte TOF and Δt is the peak width at full width half maximum. Research for higher performance MS (increased resolution) is driven by the small mass differences often encountered between peptides/proteins to be resolved from each other. For example, a mixture containing two peptides whose sequence differs by only a single (*e.g.*, lysine and glutamine), the resolution needed to resolve the $[M + H]^+$ ions (corresponding to a mass of 2000.0000 Da and 2000.0364 Da) would be 54,960,¹⁴⁴ which motivates the need to increase mass resolution in TOF experiments. Current commercial instruments offer routine mass resolutions between 15,000 and 20,000, resulting in their inability to resolve the hypothetical peptides. Mass resolution in an TOFMS is limited by several factors,¹⁴⁵ including: (i) sample preparation procedures,¹⁴⁶ (ii) stability of the high voltage power supplies (voltage drift over time), (iv) source and grid extraction parameters,⁵⁶ (v) spatial and velocity spread of the ions arising during ionization,¹⁴⁷ (vi) the base pressure of the instrument, and (vii) trajectory errors formed by initial ion packet locations (mechanical alignment), non-uniform focusing elements (field inhomogeneities) and ion scattering due to the use of grids.¹⁴⁸ The resolution-limiting parameters become more important as higher experimental resolutions are obtained, because small variations in any of these experimental parameters could

possibly limit experimental resolution. Using the known geometry of the instrument, the theoretical resolution limits were calculated, as defined by:

$$R_{es} = \sqrt{R_s^2 + R_v^2} \quad (5)$$

where R_s and R_v are resolution limits due to both spatial and velocity spread of the ions, respectively. Both spatial and velocity resolution limits depend on the type of source and reflectron that is incorporated in the instrument. Figure 34 illustrates a potential energy diagram for the Voyager elite XL instrument which contains a two-stage source and single-stage reflectron. The highest theoretical resolution of the Voyager Elite XL based on (5) is $\sim 75,000$. Source and reflectron configurations important to resolution, include: d_a (2.16 mm), length of the first accelerating region (distance between the MALDI plate and first grid), d_0 (7.2 mm), length of the second region (distance between the first grid and grounded grid), D (3357.46 mm), length of the field free drift region, d_R (857.25 mm), length of the reflectron, v_a (7750 V), voltage applied across the 1st region, v (25,000 V), total voltage applied, δv_0 (literature reported values between 500 m/s – 1000 m/s), ¹⁴⁹ initial velocity distribution, v_n , nominal velocity calculated using (3) (assuming a 5000 Da molecule), and δx (0.1 mm), the change in initial ion position in the source region. (see Appendix B for a detailed calculation)

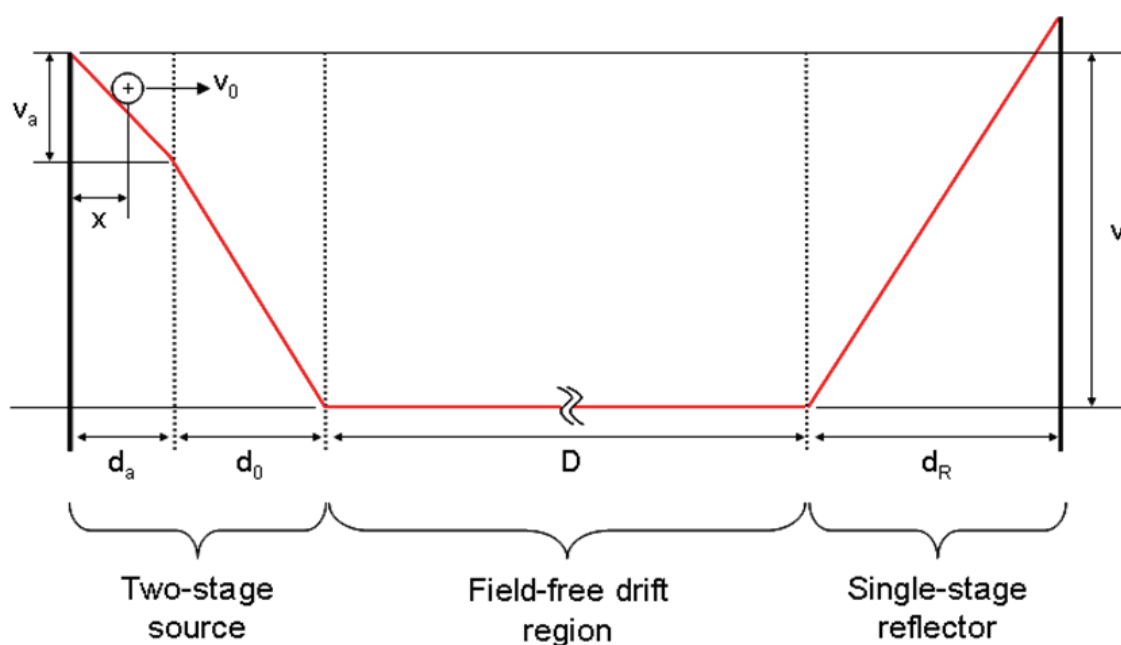


Figure 34. Potential energy diagram for the Voyager elite XL instrument which contains a two-stage source and single-stage reflectron.

Position Sensitive Ion Detection

TOF instruments typically utilize fast response microchannel plate detectors (MCPs) to detect ions in the mass spectrometer. The MCPs are integrated electron multipliers that are usually paired to achieve a desired gain in ion signal. The general scheme involves a charged particle (ion) striking the MCP surface and generating an electron cascade which can be detected with sensitive electronics as the electrons produce a current on a metal anode surface (see Figure 35). This current is directly proportional to the relative abundance of ions that strike the microchannel plates at a given time.

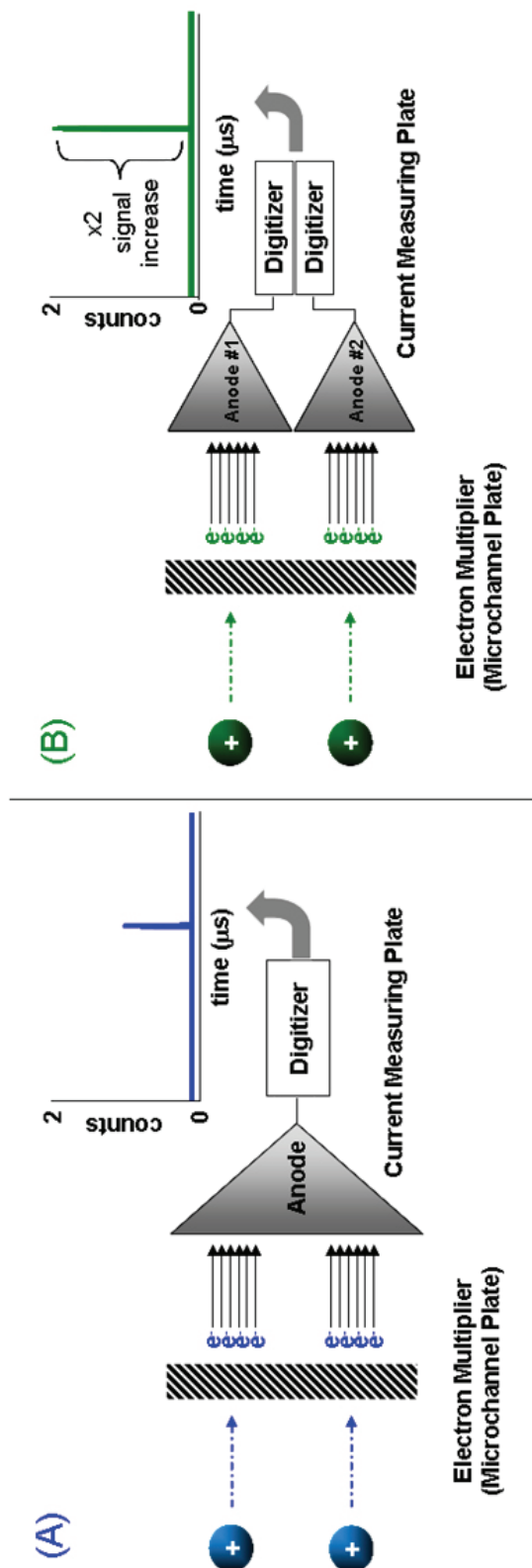


Figure 35. (A) Typical ion detection scheme for TOFMS utilizing a single anode. Each time event is measured either as a hit or no hit (0 or 1), where only one count is observed even when multiple ions strike the detector at the same time. (B) ion detection scheme utilizing two anodes, where multiple (e.g., two) counts can be observed per time event resulting in an maximum measurable amplitude of 2 per measurement event.

Figure 35A shows a simple schematic of ion detection utilizing a single anode in a TOFMS. Most MS instruments utilize a single anode for measuring signal gain, due to the technical simplicity of the detector assembly and associated electronics. However, there are three primary advantages to using multiple discrete anodes (*e.g.*, placed side by side) rather than using a single anode:¹⁵⁰

- 1) Most modern commercial MS instruments incorporate time-to-digital conversion to take advantage of the fast data acquisition capabilities of computers. In digitizing the signal, each time event is measured either as a hit or no hit (0 or 1) and then summed together into larger bins and assembled into a mass spectrum. For detectors using only a single anode, the highest signal amplitude that can be measured per measurement event is 1, but if for example two anodes are used, 1 count can be measured *per anode*, such that the maximum signal amplitude per measurement event is 2 (Figure 35B).¹⁵¹ The detector utilized in this research is a prototype 8-anode detector. Using an 8-anode detector, in pulse counting mode, single counts can be measured per anode, such that the maximum measurable signal amplitude per measurement event is 8, corresponding to the number of anodes (Figure 36A). Thus, at ion currents sufficiently high to cause “detector sag” (*i.e.*, owing to pulse pile-up) an 8x gain in sensitivity could be obtained versus standard single anode detectors.¹⁵²
- 2) Multi-anode detection also provides spatial information. That is, based on the signal amplitude response of each anode, it is possible to determine where the largest number of ions are striking the detector, and tune the instrumental

parameters accordingly to optimize overall instrument performance.¹⁵¹ Adjusting the position of the ion beam on the detector, optimizes the overall signal sensitivity and ultimately enhances the overall resolution by minimizing the undesirable effects of the inhomogeneous field domains which are inherent in all ion optical components.¹⁵³

- 3) Resolution enhancement is afforded by time correcting the ion beam partitioned across the 8 anodes. For example, Figure 37 shows that when analyzing individual mass spectra prior to time correction, it is apparent that different anodes have different centroid times (*i.e.* ions are striking the detector at different times), thereby broadening the summed peak width and reducing resolution. However, after correcting for these time differences the mass spectral resolution and sensitivity are increased. It should be noted that the use of delay line detectors has also been incorporated in TOF experiments whereby this technology also offers both spatial and temporal resolution.¹⁵⁴

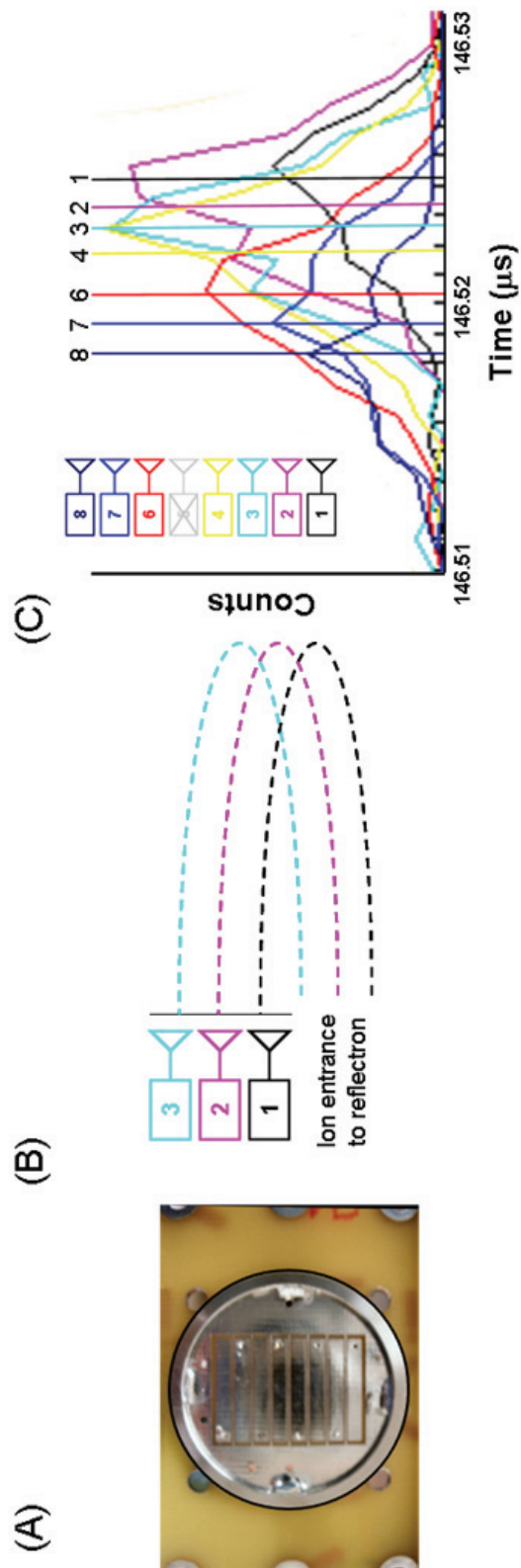


Figure 36. (A) An image of the 8 anode detector used in these studies, where individual anodes have dimensions of 0.566'' x 0.076'' (B) Schematic illustrating distance changes associated with anode placement (only anodes 1, 2 and 3 are depicted) (C) Zoomed in view of the ^{12}C peak of $[\text{DRVYIHPFHL} + \text{H}]^+$, illustrating that there is a time shift between anode peaks.

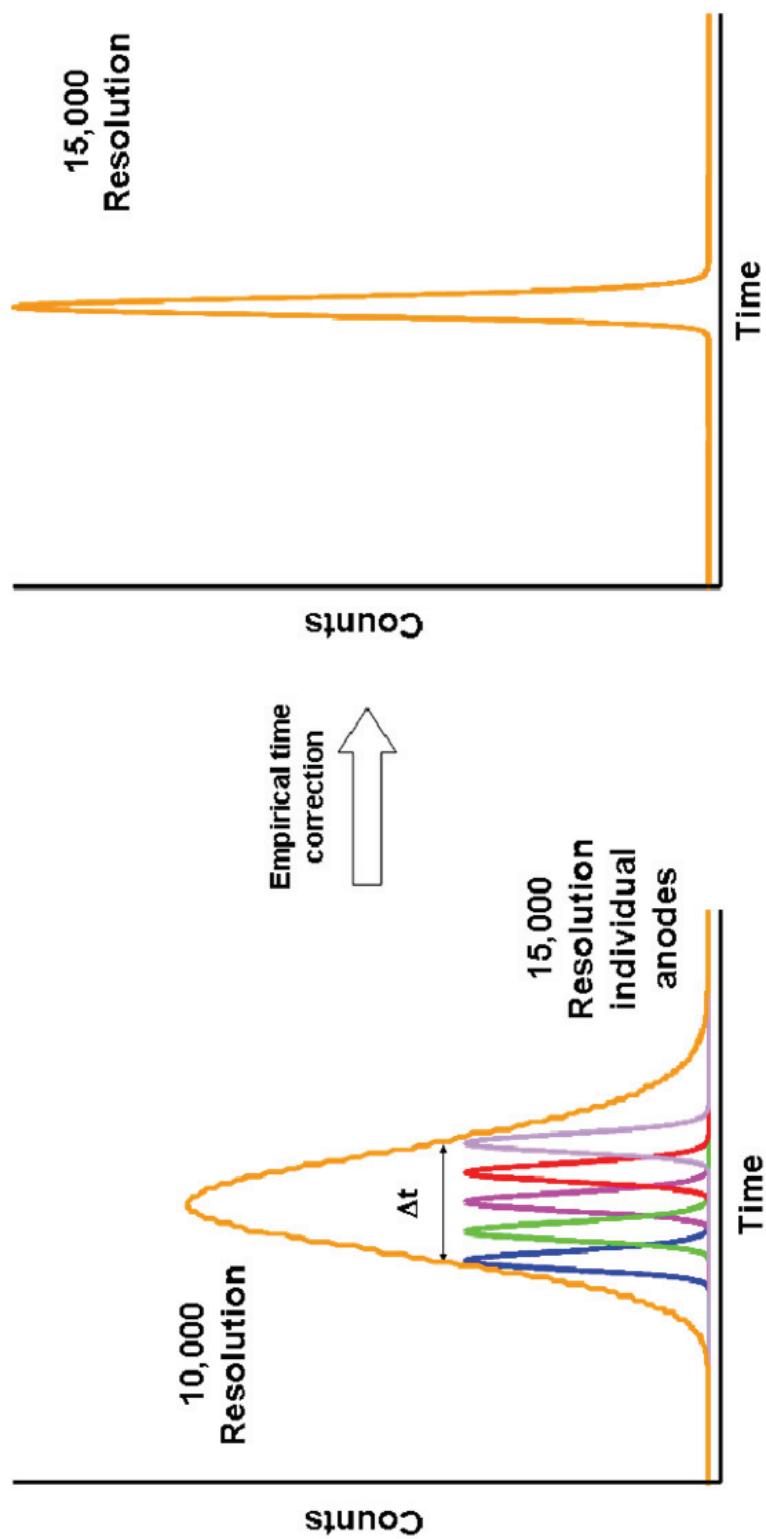


Figure 37. Representation of increased mass spectral resolution and sensitivity after time correction. Individual anodes have a resolution of 15,000, however if individual anodes are summed prior to time correction the resolution is reduced.

Results and Discussion

The practical advantage of utilizing a multi-anode detection scheme is demonstrated with the analysis of a standard peptide, Angiotensin I ($[\text{DRVYIHPFHL} + \text{H}]^+$, m/z 1296.68). Figure 36C is an expansion of the ^{12}C peak for $[\text{DRVYIHPFHL} + \text{H}]^+$ illustrating the time difference between individual anodes. Ions are impinging channel 8 first, followed by 7, 6, 4, 3, 2, and lastly 1. Summing all anodes (channels 1-8) prior to time shift correction results in a resolution of $\sim 10,000$ ($[\text{DRVYIHPFHL} + \text{H}]^+$, Figure 38A). The bin size (TDC resolution) used for this work was 1 ns, and the time-shift correlation was based on the first anode. Each successive anode (peaks from anodes 2-8) is time shifted by one bin and the maximum product (highest correlation) is assumed to be the best time alignment. The biggest shift is 7 ns, or 7 bins. After time-shift correlating channels 2-8 with respect to channel 1, the channels are summed and a best fit curve obtained, resulting in increased resolution ($\sim 13,000$ for $[\text{DRVYIHPFHL} + \text{H}]^+$, see Figure 38B). Routine resolution for individual anodes is $\sim 15,000$ (see Figure 38C) (with a concomitant reduction in signal amplitude proportional to effective anode area). These data accurately demonstrate the increase in resolution and enhancement in ion signal observed using these new data acquisition strategies.

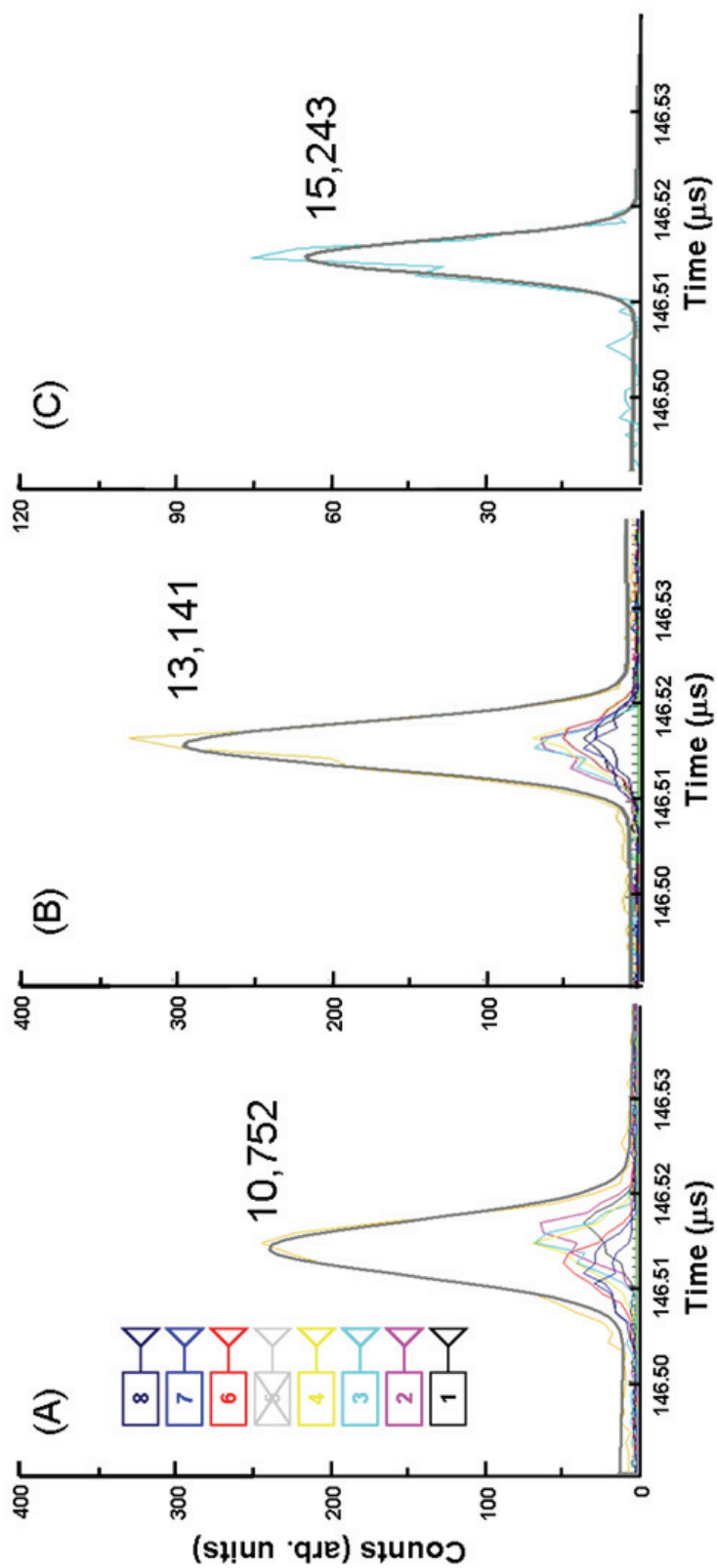


Figure 38. (A) mass spectrum illustrating time shifts across 8 anode position sensitive detector, upon summing each anode a resolution value can be calculated (10,752). (B) illustrates increased resolution by $\sim 2,000$ (13,141) after time shifts are corrected. (C) shows an individual mass spectrum for channel 3 with a resolution of 15,243.

Conclusion

New data acquisition strategies (empirical time correction for multiple anode detection schemes) were used to increase both sensitivity and resolution in a MALDI-TOF MS. The utility of this technique can be applied to many different samples, where high mass spectral resolution allows for increased mass measurement accuracy. This approach is especially useful for imaging mass spectrometry studies where only limited material is available for analysis (*e.g.*, solid-supported lipid bilayers). As previously discussed, the ability to experimentally reach theoretical mass spectral resolution limits are difficult owing to numerous experimental factors (*e.g.*, sample preparation, high voltage stability, extraction parameters, ion scattering, etc.). Future work to increase the mass spectral resolution should be approached by: (i) evaluating the effect of changing the bin size (TDC resolution, up to 130 ps) in terms of increasing the resolution (before and after time correction), (ii) optimizing instrumental parameters for higher experimental TOFMS resolution data (grid voltage, delay time, etc.), and (iii) incorporating other instrumental/experimental parameters, such as gridless ion optics, better sample preparation procedures, higher base vacuum pressures and more stable high voltage supplies to increase resolution.

CHAPTER VIII

CONCLUSIONS

Imaging mass spectrometry utilizing MALDI-TOF MS has demonstrated great potential for the spatial profiling and imaging of molecules (*e.g.*, proteins, peptides, steroids, drugs, lipids) in biologically relevant samples.

Spatially Dynamic Optical System

The incorporation of a spatially dynamic optical system allows for user defined laser spot sizes, decreased analysis times, and the ability to ionize non-congruent areas of interest simultaneously. The optical arrangement for imaging mass spectrometry utilizing MALDI-TOF MS techniques consists of three primary components: i) beam conditioning, which incorporates beam expansion, homogenization and collimation, ii) beam patterning, followed by iii) beam imaging onto the target stage. By using this arrangement, a digital micromirror array is used to quickly (ca. 20 μ s) pattern the MALDI irradiation into regular shapes (*e.g.* round, square, rectangular, etc.) or into complex shapes of variable dimensions. Further, MALDI irradiation can be tailored so that non-congruent targeted spatial regions can be irradiated simultaneously. The utility of this advanced optics technique was applied to the interrogation of peptide microarrays. By interrogating congruent square wells of the microarray, we can rapidly image the array via MS techniques. These experiments are particularly important in developing new tools for the analysis of protein microarrays, which are not dependent on

the incorporation of fluorescent tags unlike that for conventional monitoring and analysis. Novel techniques can also be used for imaging MS analysis of tissue samples, whereby healthy and diseased morphologies can be probed for specific biomarkers by irradiating either single or multiple cells simultaneously. This type of experiment is analogous to an on-line laser-capture microdissection imaging experiment. The effect of changing the spatial MALDI sampling position in imaging MS applications *optically*, rather than *mechanically* introduces an improvement in spatial resolution and provides reduced analysis times.

Sample Preparation Strategies and Methodologies

The sample preparation strategy incorporating both intact protein and peptide mass fingerprinting information for imaging MS experiments allows for high confidence-level analyte assignments. In addition, the ability to obtain multiple peptide mass fingerprinting data sets (owing to the ability to digest analytes using multiple different proteases) allows higher amino acid sequence coverage to be acquired. Combining both high amino acid sequence coverage with fragmentation data improves the confidence level of protein assignments.

The imaging mass spectrometry lipid bilayer studies demonstrate the ability to perform mass spectrometry imaging of species that are electrophoretically separated in a lipid bilayer. Sample methodologies are characterized using a fluorescently labeled membrane bound species, however further work showed the ability to image migrated receptors and peptides in solid-supported lipid bilayers. This technique offers both label-

free and multiple analyte detection in single experiments, which is extremely important when it is imperative that the integrity of the membrane component is conserved (*i.e.*, no label). The ability to use a lipid bilayer as a separation medium followed by mass spectrometry imaging will have an impact on the analysis of cell membranes. Specifically, it is now possible to monitor cell membranes for important biological processes such as the formation and chemical composition of lipid rafts or whole cell membranes without the addition of extrinsic molecules.

Laser desorption/ionization using silver nanoparticles is shown to selectively ionize olefinic compounds from complex mixtures without additional washing or extraction procedures. Specifically, both cholesterol and POPC are selectively ionized using AgNPs in a complex mixture composed of ten peptides, cholesterol and POPC. The observed differences in relative abundance of cholesterol and POPC signal can be explained by the Dewar model, which describes the Ag^+ -olefin interaction. Briefly, the rigid double bond in cholesterol is likely more accessible than the double bond in POPC, which is surrounded by freely rotating hydrocarbon chains, therefore a higher signal-to-noise value is observed for cholesterol ion signal. A carotenoid and carotenoid precursor is also selectively ionized using AgNPs from freshly squeezed carrot juice. The ability to selectively ionize specific chemical species using a simple sample preparation is especially relevant to biomarker detection, imaging MS or drug candidate research. For example, AgNP imaging MS can be used to study potential drug-protein interactions using microarrays.

Multi-anode Detection

A new data acquisition strategy incorporating a multi-anode detector is integrated into a 6.6-m time of flight mass spectrometer to increase both resolution and sensitivity. The prototype 8-anode detector allows for an increase in sensitivity by increasing the maximum measurable signal amplitude from 1 (single anode detectors) to 8, owing to the ability to obtain a single count for each anode. The multi-anode detector also provides spatial information based on the ability to determine where the ions are striking the detector (anode 1-8). Time shift corrections correlating anodes 2-8 to channel 1 results in an increase in resolution (from 10,000 to 13,000). The utility of this technique can be applied to lipid bilayer studies, where this multi-anode detection scheme is optimized in both mass spectral resolution and sensitivity for low abundant analytes.

REFERENCES

- (1) Van Vaeck, L.; Struyf, H.; Van Roy, W.; Adams, F. *Mass Spectrometry Reviews* **1994**, *13*, 189-208.
- (2) Pacholski, M. L.; Winograd, N. *Chem. Rev.* **1999**, *99*, 2977-3006.
- (3) Castner, D. G. *Nature* **2003**, *422*, 129-130.
- (4) Altelaar, A. F. M.; vanMinnen, J.; Jimenez, C. R.; Heeren, R. M. A.; Piersma, S. R. *Anal. Chem.* **2005**, *77*, 735-741.
- (5) Altelaar, A. F. M.; Klinkert, I.; Jalink, K.; deLange, R. P. J.; Adan, R. A. H.; Heeren, R. M. A.; Piersma, S. R. *Anal. Chem.* **2006**, *78*, 734-742.
- (6) Marcus, A.; Winograd, N. *Anal. Chem.* **2006**, *78*, 141-148.
- (7) Caprioli, R. M.; Farmer, T. B.; Gile, J. *Anal. Chem.* **1997**, *69*, 4751-4760.
- (8) Caprioli, R. M. *Cancer Res* **2005**, *65*, 10642-10645.
- (9) Chaurand, P.; Sanders, M. E.; Jensen, R. A.; Caprioli, R. M. *Am. J. Pathol.* **2004**, *165*, 1057-1068.
- (10) Chaurand, P.; Schwartz, S. A.; Billheimer, D.; Xu, B. J.; Crecelius, A.; Caprioli, R. M. *Anal. Chem.* **2004**, *76*, 1145-1155.
- (11) Cornett, D. S.; Mobley, J. A.; Dias, E. C.; Andersson, M.; Arteaga, C. L.; Sanders, M. E.; Caprioli, R. M. *Mol. Cell. Proteomics* **2006**, *5*, 1975-1983.
- (12) Khatib-Shahidi, S.; Andersson, M.; Herman, J. L.; Gillespie, T. A.; Caprioli, R. M. *Anal. Chem.* **2006**, *78*, 6448-6456.

- (13) Amann, J. M.; Chaurand, P.; Gonzalez, A.; Mobley, J. A.; Massion, P. P.; Carbone, D. P.; Caprioli, R. M. *Clinical Cancer Research* **2006**, *12*, 5142-5150.
- (14) Schwartz, S. A.; Reyzer, M. L.; Caprioli, R. M. *J. Mass Spectrom.* **2003**, *38*, 699-708.
- (15) Novikov, A.; Caroff, M.; Della-Negra, S.; Lebeyec, Y.; Pautrat, M.; Schultz, J. A.; Tempez, A.; Wang, H. Y. J.; Jackson, S. N.; Woods, A. S. *Anal. Chem.* **2004**, *76*, 7288-7293.
- (16) Tempez, A.; Ugarov, M.; Egan, T.; Schultz, J. A.; Novikov, A.; Della-Negra, S.; Lebeyec, Y.; Pautrat, M.; Caroff, M.; Smentkowski, V. S.; Wang, H. Y. J.; Jackson, S. N.; Woods, A. S. *J. Proteome Res.* **2005**, *4*, 540-545.
- (17) Scherl, A.; Zimmermann-Ivol, C. G.; Dio, J. D.; Vaezzadeh, A. R.; Binz, P.-A.; Amez-Droz, M.; Cochard, R.; Sanchez, J.-C.; Glückmann, M.; Hochstrasser, D. F. *Rapid Commun. Mass Spectrom.* **2005**, *19*, 605-610.
- (18) Groseclose, M. R.; Andersson, M.; Hardesty, W. M.; Caprioli, R. M. *J. Mass Spectrom.* **2007**, *42*, 254-262.
- (19) Aerni, H. R.; Cornett, D. S.; Caprioli, R. M. *Anal. Chem.* **2006**, *78*, 827-834.
- (20) Hensel, R. R.; King, R. C.; Owens, K. G. *Rapid Commun. Mass Spectrom.* **1997**, *11*, 1785-1793.
- (21) Hankin, J. A.; Barkley, R. M.; Murphy, R. C. *J. Am. Soc. Mass Spectrom.* **2007**, *18*, 1646-1652.
- (22) Puolitaival, S. M.; Burnum, K. E.; Cornett, D. S.; Caprioli, R. M. *J. Am. Soc. Mass Spectrom.* **2008**, *19*, 882-886.

- (23) Garrett, T. J.; Prieto-Conaway, M. C.; Kovtoun, V.; Bui, H.; Izgarian, N.; Stafford, G.; Yost, R. A. *Int. J. Mass Spectrom.* **2007**, *260*, 166-176.
- (24) Baluya, D. L.; Garrett, T. J.; Yost, R. A. *Anal. Chem.* **2007**, *79*, 6862-6867.
- (25) Taira, S.; Sugiura, Y.; Moritake, S.; Shimma, S.; Ichiyanagi, Y.; Setou, M. *Anal. Chem.* **2008**, *80*, 4761-4766.
- (26) Cooks, R. G.; Ouyang, Z.; Takats, Z.; Wiseman, J. M. *Science* **2006**, *311*, 1566-1570.
- (27) Ifa, D. R.; Wiseman, J. M.; Song, Q.; Cooks, R. G. *Int. J. Mass Spectrom.* **2007**, *259*, 8-15.
- (28) Wiseman, J. M.; Ifa, D. R.; Song, Q.; Cooks, R. G. *Angew. Chem., Int. Ed.* **2006**, *45*, 7188-7192.
- (29) Kertesz, V.; VanBerkel, G. J. *Anal. Chem.* **2008**, *80*, 1027-1032.
- (30) VanBerkel, G. J.; Ford, M. J.; Deibel, M. A. *Anal. Chem.* **2005**, *77*, 1207-1215.
- (31) VanBerkel, G. J.; Kertesz, V. *Anal. Chem.* **2006**, *78*, 6283-6283.
- (32) Ford, M. J.; Deibel, M. A.; Tomkins, B. A.; VanBerkel, G. J. *Anal. Chem.* **2005**, *77*, 4385-4389.
- (33) Kertesz, V.; Ford, M. J.; VanBerkel, G. J. *Anal. Chem.* **2005**, *77*, 7183-7189.
- (34) Van Berkel, G. J.; Sanchez, A. D.; Quirke, J. M. E. *Anal. Chem.* **2002**, *74*, 6216-6223.
- (35) Nemes, P.; Barton, A. A.; Li, Y.; Vertes, A. *Anal. Chem.* **2008**, *80*, 4575-4582.
- (36) Dreisewerd, K.; Draude, F.; Kruppe, S.; Rohlfing, A.; Berkenkamp, S.; Pohlentz, G. *Anal. Chem.* **2007**, *79*, 4514-4520.

- (37) Li, Y.; Shrestha, B.; Vertes, A. *Anal. Chem.* **2007**, *79*, 523-532.
- (38) Henzel, W. J.; Watanabe, C.; Stults, J. T. *J. Am. Soc. Mass Spectrom.* **2003**, *14*, 931-942.
- (39) Müller, M.; Gras, R.; Appel, R. D.; Bienvenut, W. V.; Hochstrasser, D. F. *J. Am. Soc. Mass Spectrom.* **2002**, *13*, 221-231.
- (40) Vaezzadeh, A. R.; Simicevic, J.; Chauvet, A.; François, P.; Zimmermann-Ivol, C. G.; Lescuyer, P.; Deshusses, J. P. M.; Hochstrasser, D. F. *Rapid Commun. Mass Spectrom.* **2008**, *22*, 2667-2676.
- (41) Jackson, S. N.; Ugarov, M.; Egan, T.; Post, J. D.; Langlais, D.; Schultz, J. A.; Woods, A. S. *J. Mass Spectrom.* **2007**, *42*, 1093-1098.
- (42) McLean, J. A.; Ridenour, W. B.; Caprioli, R. M. *J. Mass Spectrom.* **2007**, *42*, 1099-1105.
- (43) Ruotolo, B. T.; Gillig, K. J.; Stone, E. G.; Russell, D. H. *Journal of Chromatography B* **2002**, *782*, 385-392.
- (44) Stone, E. G.; Gillig, K. J.; Ruotolo, B. T.; Russell, D. H. *Int. J. Mass Spectrom.* **2001**, *212*, 519-533.
- (45) Sun, W.; May, J. C.; Russell, D. H. *Int. J. Mass Spectrom.* **2007**, *259*, 79-86.
- (46) Cornett, D. S.; Frappier, S. L.; Caprioli, R. M. *Anal. Chem.* **2008**, *80*, 5648-5653.
- (47) Smith, W. J., Ed. *Practical Optical System Layout and Use of Stock Lenses*; McGraw-Hill Companies, Inc.: New York, 1997.
- (48) Spengler, B.; Hubert, M. *J. Am. Soc. Mass Spectrom.* **2002**, *13*, 735-748.

- (49) Kossakovski, D. A.; O'Connor, S. D.; Widmer, M.; Baldeschwieler, J. D.; Beauchamp, J. L. *Ultramicroscopy* **1998**, *71*, 111-115.
- (50) Betzig, E.; Trautman, J. K.; Harris, T. D.; Weiner, J. S.; Kostelak, R. L. *Science* **1991**, *251*, 1468-1470.
- (51) Caprioli, R. M.; Farmer, T. B.; Gile, J. *Anal. Chem.* **1997**, *69*, 4751-4760.
- (52) Garden, R. W.; Sweedler, J. V. *Anal. Chem.* **2000**, *72*, 30-36.
- (53) Luxembourg, S. L.; Mize, T. H.; McDonnell, L. A.; Heeren, R. M. A. *Anal. Chem.* **2004**, *76*, 5339-5344.
- (54) Jurchen, J. C.; Rubakhin, S. S.; Sweedler, J. V. *J. Am. Soc. Mass Spectrom.* **2005**, *16*, 1654-1659.
- (55) Monroe, E. B.; Jurchen, J. C.; Koszczuk, B. A.; Losh, J. L.; Rubakhin, S. S.; Sweedler, J. V. *Anal. Chem.* **2006**, *78*, 6826-6832.
- (56) Vestal, M.; Juhasz, P. *J. Am. Soc. Mass Spectrom.* **1998**, *9*, 892-911.
- (57) Norris, J. L.; Cornett, D. S.; Mobley, J. A.; Andersson, M.; Seeley, E. H.; Chaurand, P.; Caprioli, R. M. *Int. J. Mass Spectrom.* **2007**, *260*, 212-221.
- (58) Washburn, M. P.; Wolters, D.; Yates, J. R. *Nat Biotech* **2001**, *19*, 242-247.
- (59) Kelleher, N. L.; Lin, H. Y.; Valaskovic, G. A.; Aaserud, D. J.; Fridriksson, E. K.; McLafferty, F. W. *J. Am. Chem. Soc.* **1999**, *121*, 806-812.
- (60) Russell, W. K.; Park, Z. Y.; Russell, D. H. *Anal. Chem.* **2001**, *73*, 2682-2685.
- (61) Pacholski, M. L.; Winograd, N. *Chem. Rev.* **1999**, *99*, 2977-3006.
- (62) Castaing, R.; Slodzian, G. *J. Microsc.* **1962**, *1*, 395-410

- (63) Van Vaeck, L.; Struyf, H.; Van Roy, W.; Adams, F. *Mass Spectrom. Rev.* **1994**, *13*, 209-232.
- (64) Li, L.; Garden, R. W.; Sweedler, J. V. *Trends Biotechnol.* **2000**, *18*, 151-160.
- (65) Yanagisawa, K.; Shyr, Y.; Xu, B. J.; Massion, P. P.; Larsen, P. H.; White, B. C.; Roberts, J. R.; Edgerton, M.; Gonzalez, A.; Nadaf, S.; Moore, J. H.; Caprioli, R. M.; Carbone, D. P. *Lancet* **2003**, *362*, 433-439.
- (66) Chaurand, P.; Caprioli, R. M. *Electrophoresis* **2002**, *23*, 3125-3135.
- (67) Rohner, T. C.; Staab, D.; Stoeckli, M. *Mech. Ageing Dev.* **2005**, *126*, 177-185.
- (68) Chaurand, P.; Schwartz, S. A.; Caprioli, R. M. *Curr. Opin. Chem. Biol.* **2002**, *6*, 676-681.
- (69) Chaurand, P.; Schwartz, S. A.; Billheimer, D.; Xu, B. J.; Crecelius, A.; Caprioli, R. M. *Anal. Chem.* **2004**, *76*, 1145-1155.
- (70) Altelaar, A. F. M.; vanMinnen, J.; Jimenez, C. R.; Heeren, R. M. A.; Piersma, S. R. *Anal. Chem.* **2005**, *77*, 735-741.
- (71) Marcus, A.; Winograd, N. *Anal. Chem.* **2006**, *78*, 141-148.
- (72) Altelaar, A. F. M.; Klinkert, I.; Jalink, K.; deLange, R. P. J.; Adan, R. A. H.; Heeren, R. M. A.; Piersma, S. R. *Anal. Chem.* **2006**, *78*, 734-742.
- (73) Caprioli, R. M. *Cancer Res.* **2005**, *65*, 10642-10645.
- (74) Stockle, R.; Setz, P.; Deckert, V.; Lippert, T.; Wokaun, A.; Zenobi, R. *Anal. Chem.* **2001**, *73*, 1399-1402.

- (75) McDonnell, L. A.; Piersma, S. R.; Altelaar, M. A. F.; Mize, T. H.; Luxembourg, S. L.; Verhaert, P. D. E. M.; van Minnen, J.; Heeren, R. M. A. *J. Mass Spectrom.* **2005**, *40*, 160-168.
- (76) Knochenmuss, R. *J. Mass Spectrom.* **2002**, *37*, 867-877.
- (77) Dreisewerd, K.; Schurenberg, M.; Karas, M.; Hillenkamp, F. *Int. J. Mass Spectrom. Ion Processes* **1995**, *141*, 127-148.
- (78) McLean, J. A.; Russell, D. H. Advanced Optics for Rapidly Patterned Laser Profiles in Analytical Mass Spectrometry; U.S. Patent No. 2007: 7,282,706.
- (79) McLean, J. A.; Russell, D. H.; Egan, T. F.; Ugarov, M. V.; Schultz, J. A. Multiplex Data Acquisition Modes for Ion Mobility-Mass Spectrometry; U.S. Patent No. 2008: 7,388,197.
- (80) Dudley, D.; Duncan, W.; Slaughter, J. *White Paper*, DLP Products New Applications, Texas Instruments, Inc. Plano, TX, Oct. 2000.
- (81) Wagner, E. P.; Smith, B. W.; Madden, S.; Winefordner, J. D.; Mignardi, M. *Appl. Spectrosc.* **1995**, *49*, 1715-1719.
- (82) DeVerse, R. A.; Hammaker, R. M.; Fateley, W. G. *Vib. Spectrosc.* **1999**, *19*, 177-186.
- (83) Fateley, W. G.; Hammaker, R. M.; DeVerse, R. A. *J. Mol. Struct.* **2000**, *550-551*, 117-122.
- (84) DeVerse, R. A.; Hammaker, R. M.; Fateley, W. G. *Appl. Spectrosc.* **2000**, *54*, 1751-1758.

- (85) Singh-Gasson, S.; Green, R. D.; Yue, Y.; Nelson, C.; Blattner, F.; Sussman, M. R.; Cerrina, F. *Nat. Biotechnol.* **1999**, *17*, 974-978.
- (86) Schena, M. *Microarray Analysis*, first ed.; John Wiley & Sons: Hoboken, New Jersey, 2003.
- (87) Wenzel, R. J.; Prather, K. A. *Rapid Commun. Mass Spectrom.* **2004**, *18*, 1525-1533.
- (88) McLean, J. A.; Minnich, M. G.; Montaser, A.; Su, J.; Lai, W. *Anal. Chem.* **2000**, *72*, 4796-4804.
- (89) Lundstrom, K. *Cell. Mol. Life Sci.* **2006**, *63*, 2597-2607.
- (90) HaiAn Zheng ; Ju Zhao; Wanyun Sheng; Xie, X.-Q. *Biopolymers* **2006**, *83*, 46-61.
- (91) Galli Marxer, C.; Kraft, M. L.; Weber, P. K.; Hutcheon, I. D.; Boxer, S. G. *Biophys. J.* **2005**, *88*, 2965-2975.
- (92) Kraft, M. L.; Weber, P. K.; Longo, M. L.; Hutcheon, I. D.; Boxer, S. G. *Science* **2006**, *313*, 1948-1951.
- (93) McQuaw, C. M.; Zheng, L.; Ewing, A. G.; Winograd, N. *Langmuir* **2007**, *23*, 5645-5650.
- (94) Zheng, L.; McQuaw, C. M.; Ewing, A. G.; Winograd, N. *J. Am. Chem. Soc.* **2007**, *129*, 15730-15731.
- (95) Ostrowski, S. G.; Kurczy, M. E.; Roddy, T. P.; Winograd, N.; Ewing, A. G. *Anal. Chem.* **2007**, *79*, 3554-3560.
- (96) Prinz, C.; Malm, J.; Hook, F.; Sjoval, P. *Langmuir* **2007**, *23*, 8035-8041.

- (97) Barenholz, Y.; Gibbes, D.; Litman, B. J.; Goll, J.; Thompson, T. E.; Carlson, F. *D. Biochemistry* **1977**, *16*, 2806-2810.
- (98) Yang, T.; Jung, S. y.; Mao, H.; Cremer, P. S. *Anal. Chem.* **2001**, *73*, 165-169.
- (99) Boxer, S. G. *Curr. Opin. Chem. Biol.* **2000**, *4*, 704-709.
- (100) Axelrod, D.; Koppel, D. E.; Schlessinger, J.; Elson, E.; Webb, W. W. *Biophys. J.* **1976**, *16*, 1055-1069.
- (101) Daniel, S.; Diaz, A. J.; Martinez, K. M.; Bench, B. J.; Albertorio, F.; Cremer, P. *S. J. Am. Chem. Soc.* **2007**, *129*, 8072-8073.
- (102) Johansson, B. *Surf. Interface Anal.* **2006**, *38*, 1401-1412.
- (103) Spangler, B. D. *FEMS Microbiol. Rev.* **1992**, *56*, 622-647.
- (104) Tanaka, K.; Waki, H.; Ido, Y.; Akita, S.; Yoshida, Y.; Yoshida, T.; Matsuo, T. *Rapid Commun. Mass Spectrom.* **1988**, *2*, 151-153.
- (105) McLean, J. A.; Stumpo, K. A.; Russell, D. H. *J. Am. Chem. Soc.* **2005**, *127*, 5304-5305.
- (106) Hua, L.; Chen, J.; Ge, L.; Tan, S. N. *J. Nanopart. Res.* **2007**, *9*, 1133-1138.
- (107) Chen, Y.; Vertes, A. *Anal. Chem.* **2006**, *78*, 5835-5844.
- (108) Go, E. P.; Apon, J. V.; Luo, G.; Saghatelian, A.; Daniels, R. H.; Sahi, V.; Dubrow, R.; Cravatt, B. F.; Vertes, A.; Siuzdak, G. *Anal. Chem.* **2005**, *77*, 1641-1646.
- (109) Vertes, A. In *Laser Ablation and Its Applications*; Phipps, C. R., Ed.; Springer: New York, 2007, pp 505-528.

- (110) Xu, S.; Li, Y.; Zou, H.; Qiu, J.; Guo, Z.; Guo, B. *Anal. Chem.* **2003**, *75*, 6191-6195.
- (111) Finkel, N. H.; Prevo, B. G.; Velez, O. D.; He, L. *Anal. Chem.* **2005**, *77*, 1088-1095.
- (112) Castellana, E. T.; Russell, D. H. *Nanoletters* **2007**, *7*, 3023-3025.
- (113) Wen, X.; Dagan, S.; Wysocki, V. H. *Anal. Chem.* **2007**, *79*, 434-444.
- (114) Northen, T. R.; Yanes, O.; Northen, M. T.; Marrinucci, D.; Uritboonthai, W.; Apon, J.; Golledge, S. L.; Nordstrom, A.; Siuzdak, G. *Nature* **2007**, *449*, 1033-1036.
- (115) Link, S.; El-Sayed, M. A. *Annu. Rev. Phys. Chem.* **2003**, *54*, 331-366.
- (116) Lin, P. C.; Tseng, M. C.; Su, A. K.; Chen, Y. J.; Lin, C. C. *Anal. Chem.* **2007**, *79*, 3401-3408.
- (117) Vanderpuije, B. N. Y.; Han, G.; Rotello, V. M.; Vachet, R. W. *Anal. Chem.* **2006**, *78*, 5491-5496.
- (118) Teng, C. H.; Ho, K. C.; Lin, Y. S.; Chen, Y. C. *Anal. Chem.* **2004**, *76*, 4337-4342.
- (119) Mengistu, T. Z.; DeSouza, L.; Morin, S. *Chem. Commun.* **2005**, 5659-5661.
- (120) Ning Tang, P. T. S. R. W. *Mass Spectrom. Rev.* **2004**, *23*, 34-44.
- (121) Shen, J.; Ahmed, T.; Vogt, A.; Wang, J.; Severin, J.; Smith, R.; Dorwin, S.; Johnson, R.; Harlan, J.; Holzman, T. *Anal Biochem* **2005**, *345*, 258-269.
- (122) Brockman, A. H.; Dodd, B. S.; Orlando, R. *Anal. Chem.* **1997**, *69*, 4716-4720.
- (123) Zhang, J.; Brodbelt, J. S. *Anal. Chem.* **2005**, *77*, 1761-1770.

- (124) Bayer, E.; Gfrörer, P.; Rentel, C. *Angew. Chem., Int. Ed.* **1999**, 38, 992-995.
- (125) Rentel, C.; Strohschein, S.; Albert, K.; Bayer, E. *Anal. Chem.* **1998**, 70, 4394-4400.
- (126) Talaty, E. R.; Perera, B. A.; Gallardo, A. L.; Barr, J. M.; Van Stipdonk, M. J. *J. Phys. Chem. A* **2001**, 105, 8059-8068.
- (127) Kang, Y. S.; Kang, S. W.; Kim, H.; Kim, J. H.; Won, J.; Kim, C. K.; Char, K. *Advanced Materials* **2007**, 19, 475-479.
- (128) Morris, L. J. *J. Lipid Res.* **1966**, 7, 717-732.
- (129) Guha, O. K.; Janak, J. *J. Chromatogr., A* **1972**, 68, 325-343.
- (130) Nikolova-Damyanova, B. In *Advances in Lipid Methodology - One*; Christie, W. W., Ed.; Oily Press: Ayr, Scotland, 1992, pp 181-237.
- (131) Nikolova-Damyanova, B.; Momchilova, S. *J. Liq. Chromatogr. Relat. Technol.* **2001**, 24, 1447 - 1466.
- (132) Nygren, H.; Malmberg, P.; Kriegeskotte, C.; Arlinghaus, H. F. *FEBS Lett.* **2004**, 566, 291-293.
- (133) Nygren, H.; Malmberg, P. *J. Microsc.* **2004**, 215, 156-161.
- (134) Sjövall, P.; Lausmaa, J.; Nygren, H.; Carlsson, L.; Malmberg, P. *Anal. Chem.* **2003**, 75, 3429-3434.
- (135) Mingos, D. M. P. *J. Organomet. Chem.* **2001**, 635, 1-8.
- (136) Stair, P. C. *J. Am. Chem. Soc.* **1982**, 104, 4044-4052.
- (137) Stumpo, K.; Russell, D. H. *J. Phys. Chem. C* **2008**, submitted.
- (138) United States Department of Agriculture, www.usda.gov (accessed 03/2008).

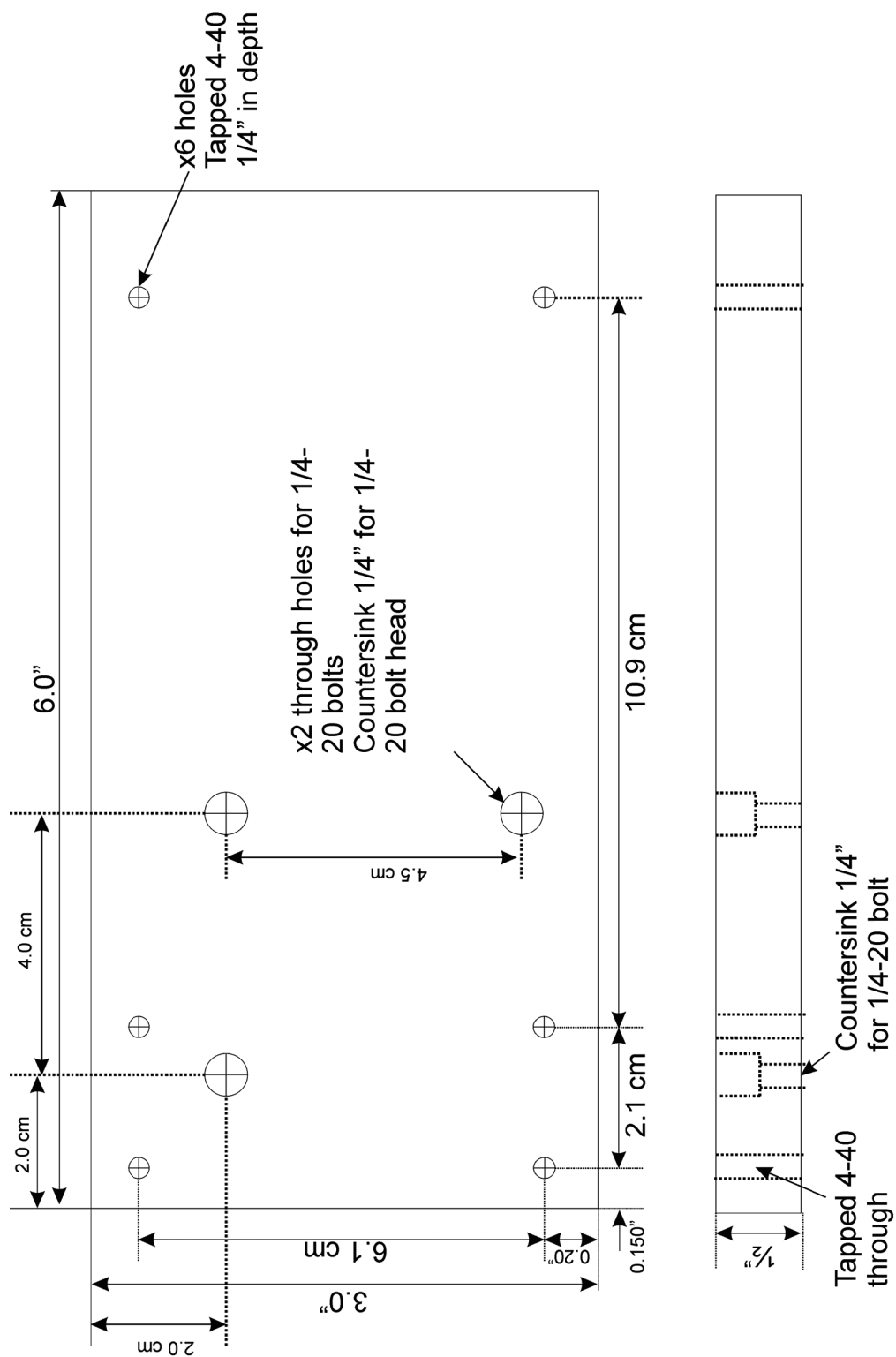
- (139) Enzell, C. R.; Appleton, R. A.; Wahlberg, I. In *Biochemical Applications of Mass Spectrometry*; Waller, G. R., Ed.; Wiley-Interscience: New York, 1972, pp 351-385.
- (140) van Breeman, R. B. *Current Protocols in Food Analytical Chemistry* **2001**, F2.4.1 - F2.4.13.
- (141) Gaberc-Porekar, V.; Menart, V. *J. Biochem. Biophys. Methods* **2001**, *49*, 335-360.
- (142) Posewitz, M. C.; Tempst, P. *Anal. Chem.* **1999**, *71*, 2883-2892.
- (143) Chaga, G. S. *J. Biochem. Biophys. Methods* **2001**, *49*, 313-334.
- (144) Marshall, A. G.; Hendrickson, C. L.; Shi, S. D.-H. *Anal. Chem.* **2002**, *74*, 252A-259A.
- (145) Barbacci, D. C.; Edmondson, R. D.; Russell, D. H. *Int. J. Mass Spectrom. Ion Processes* **1997**, *165-166*, 221-235.
- (146) Koomen, J. M.; Russell, W. K.; Hettick, J. M.; Russell, D. H. *Anal. Chem.* **2000**, *72*, 3860-3866.
- (147) Russell, D. H.; Edmondson, R. D. *J. Mass Spectrom.* **1997**, *32*, 263-276.
- (148) Bhowmick, A.; Carvalho, W. C. J.; Korgaonkar, A. V.; Yakhmi, J. V.; Sahni, V. *C. International Journal of Modern Physics B* **2005**, *19*, 2621-2626.
- (149) Beavis, R. C.; Chait, B. T. *Chem. Phys. Lett.* **1991**, *181*, 479-484.
- (150) Fuhrer, K.; Gonin, M.; Gillig, K. J.; Egan, T.; McCully, M. I.; Schultz, J. A. Time-of-flight mass spectrometer instruments for monitoring fast processes; U.S. Patent No. 2004: 6,683,299.

- (151) Barbacci, D. C.; Russell, D. H.; Schultz, J. A.; Holocek, J.; Ulrich, S.; Burton, W.; Van Stipdonk, M. *J. Am. Soc. Mass Spectrom.* **1998**, *9*, 1328-1333.
- (152) Koppenaal, D.; Barinaga, C.; Denton, M. B.; Sperline, R. P.; Hieftje, G. M.; Schilling, G. D.; Andrade, F. J.; Barnes, J. H. *Anal. Chem.* **2005**, *77*, 418A-427A.
- (153) Bergmann, T.; Martin, T. P.; Schaber, H. *Rev. Sci. Instrum.* **1989**, *60*, 347-349.
- (154) Oelsner, A.; Schmidt, O.; Schicketanz, M.; Klais, M.; Schonhense, G.; Mergel, V.; Jagutzki, O.; Schmidt-Bocking, H. *Rev. Sci. Instrum.* **2001**, *72*, 3968-3974.

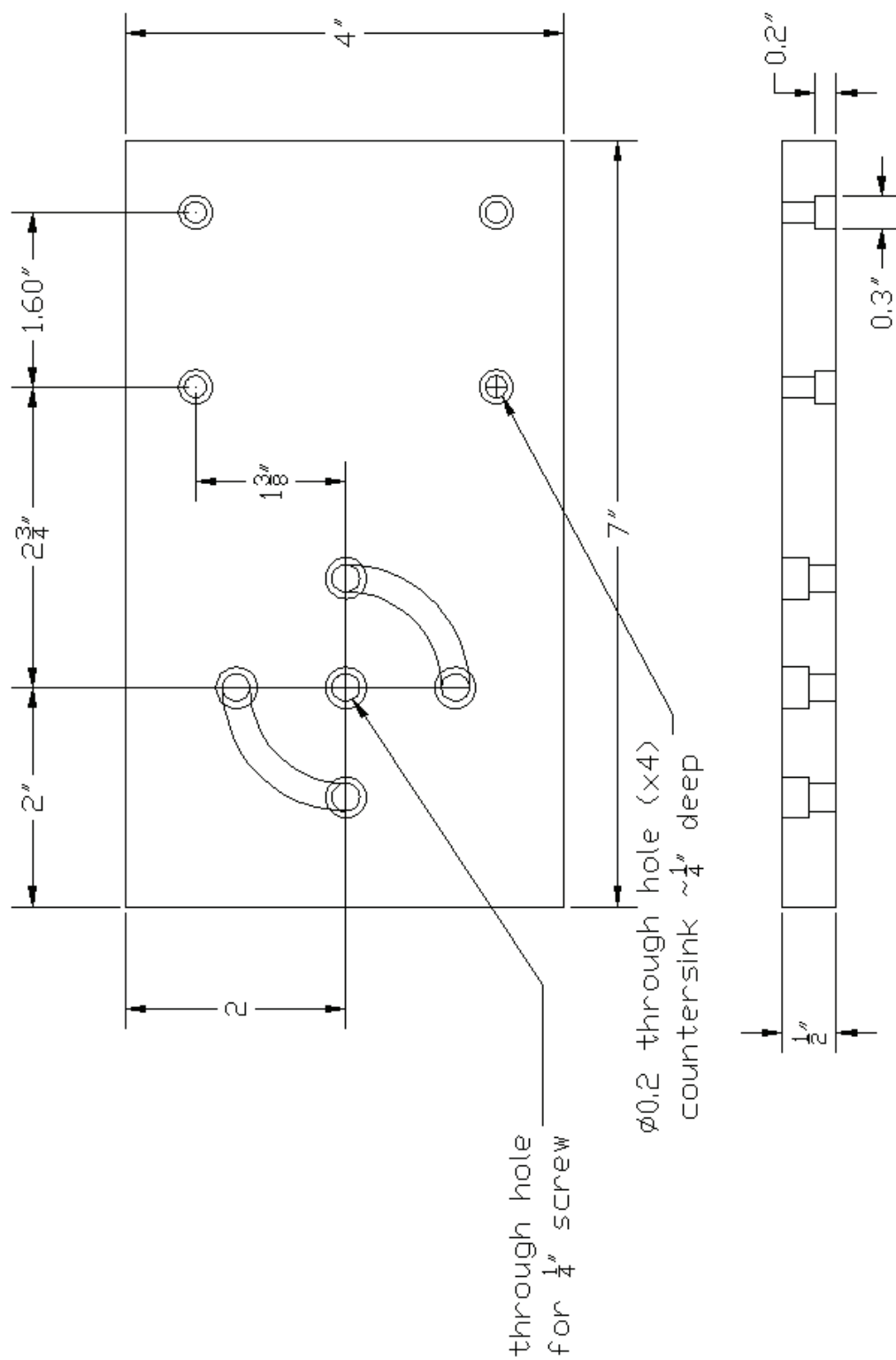
APPENDIX A

LASER OPTIC DRAWINGS

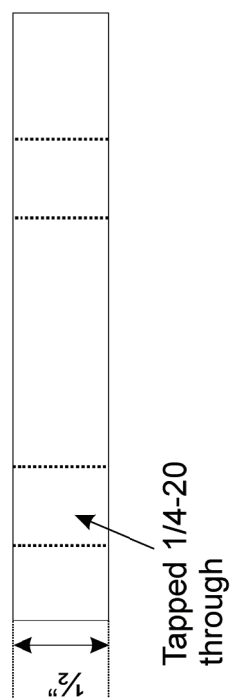
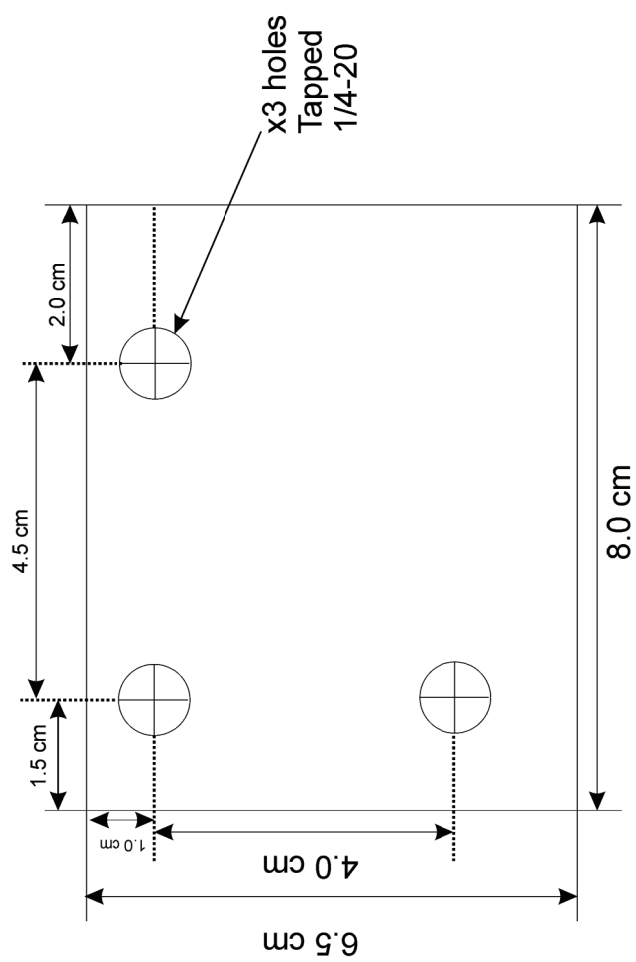
DRAWING	Page
Back Plate for Digital Micromirror Array	125
Digital Micromirror Array Mount	126
Tilt Mount for Digital Micromirror Array	127
Homogenizer Array Mount	128
Homogenizer Mount Caps	129
Homogenizer Assembled Drawing	130
Homogenizer Array Spacer	131
Single Lens System	132



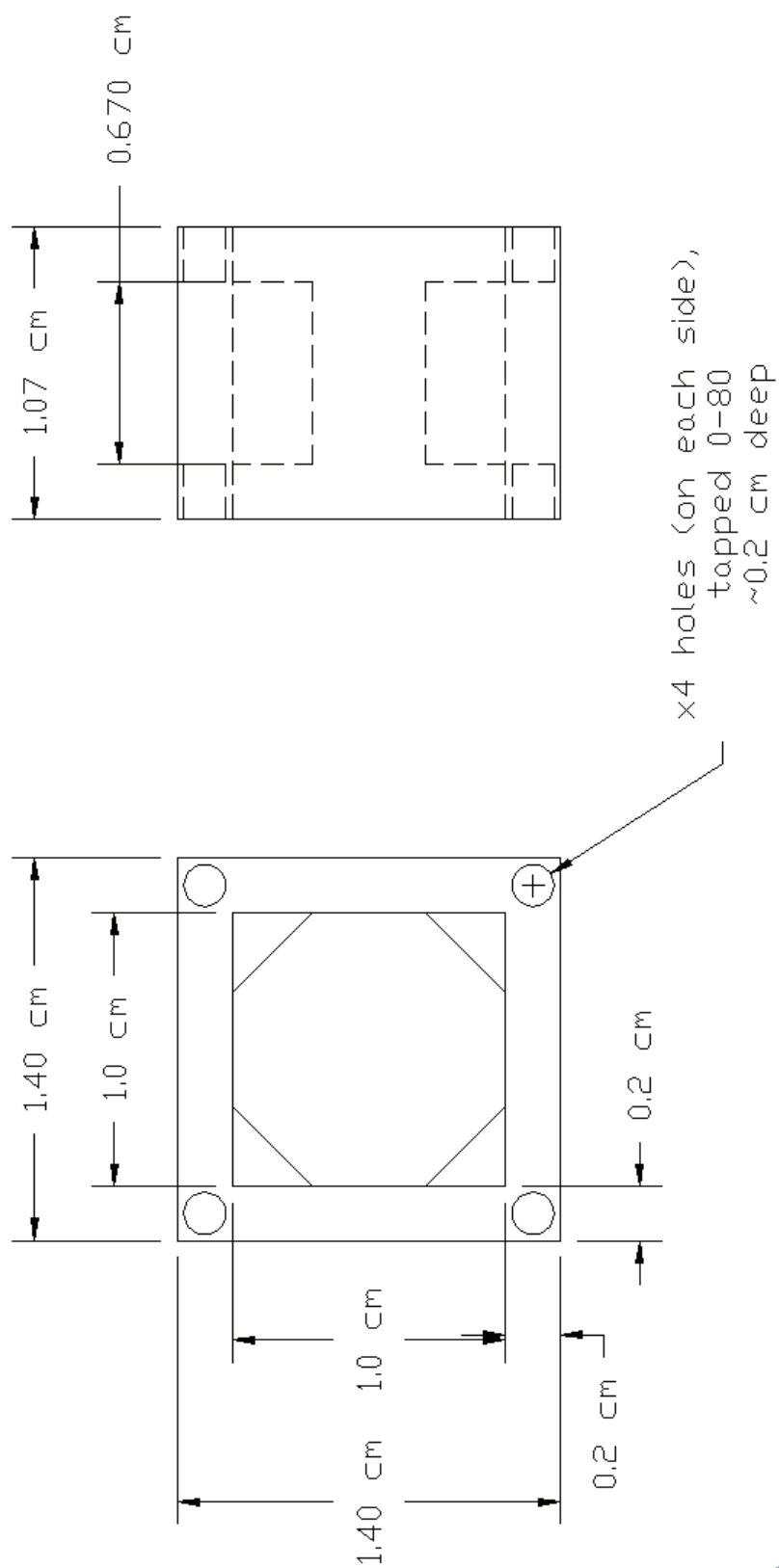
Back Plate for Digital Micromirror Array



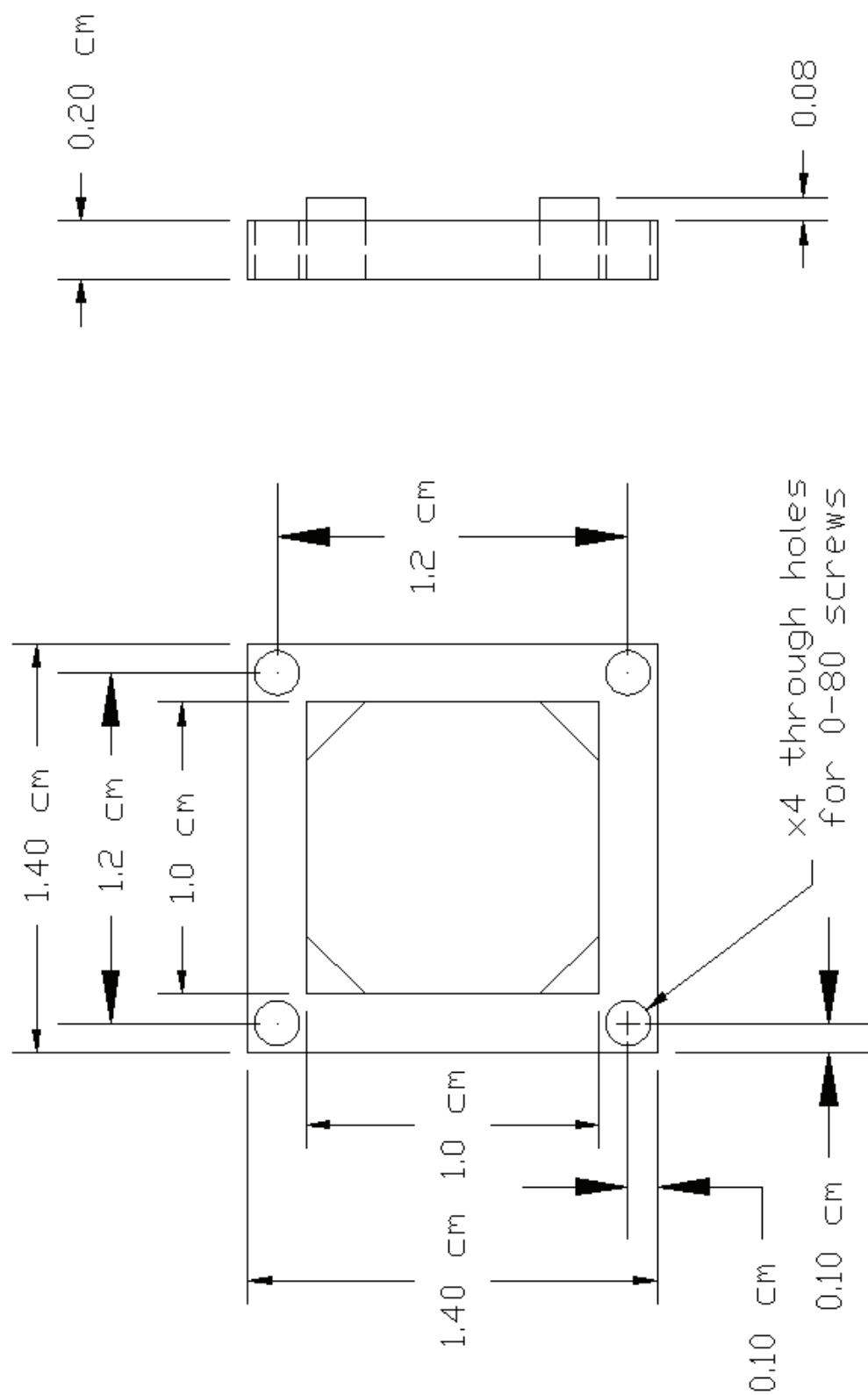
Digital Micromirror Array Mount



Tilt Mount for Digital Micromirror Array

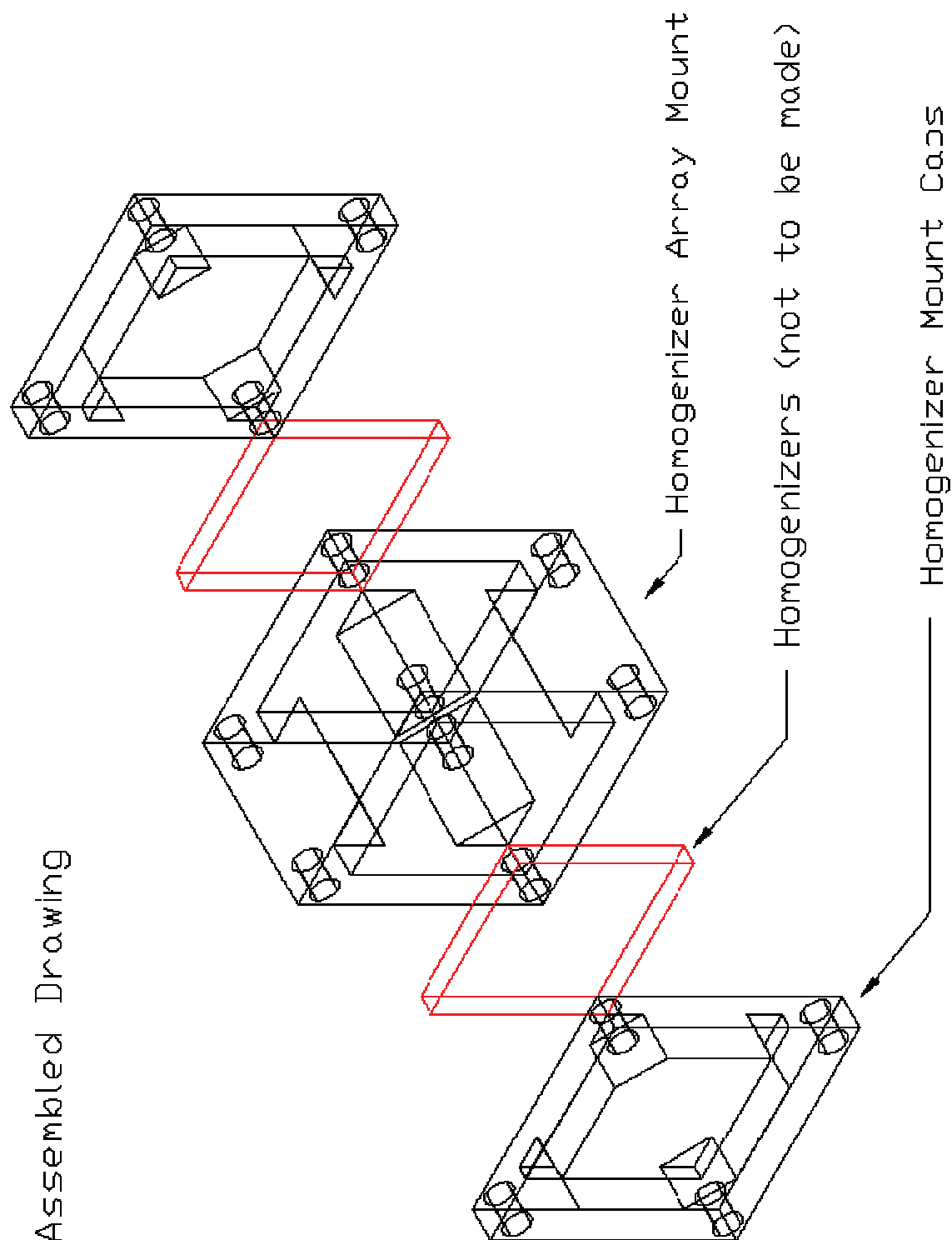


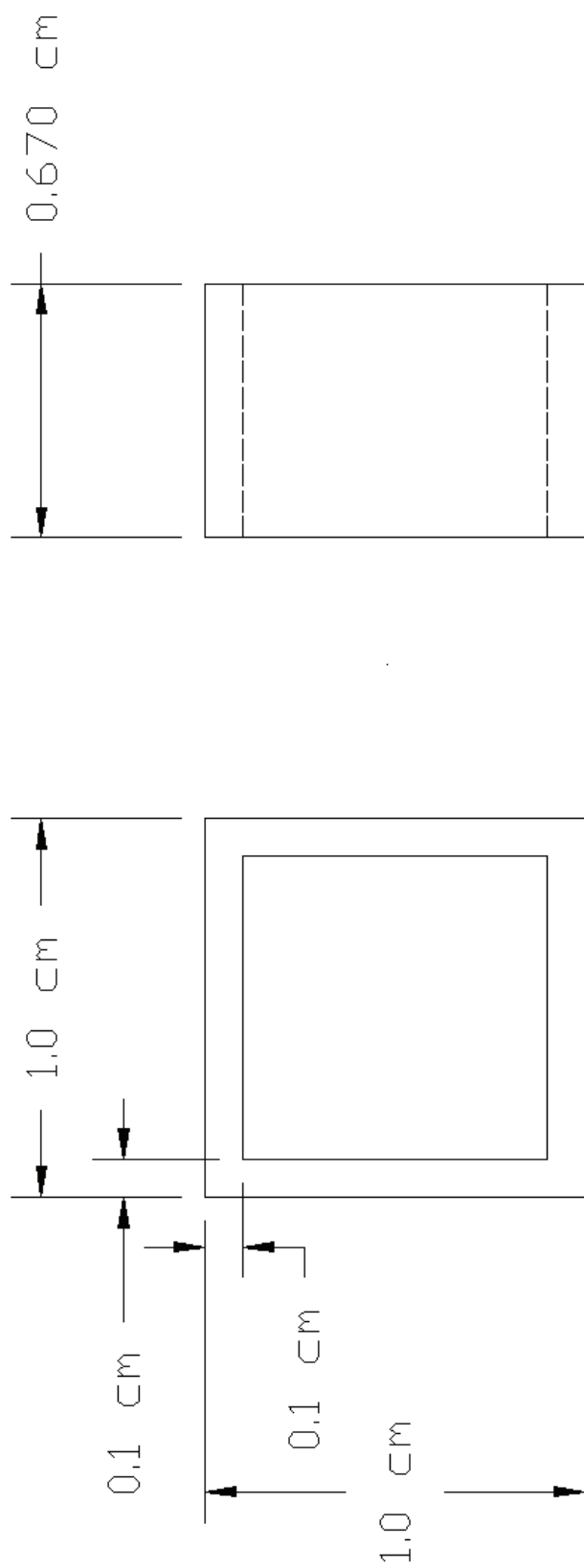
Homogenizer Array Mount



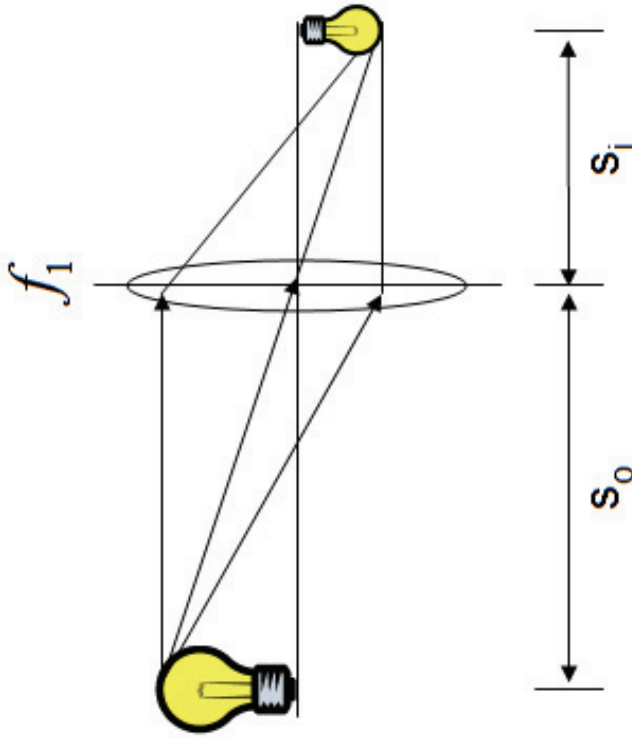
Homogenizer Mount Caps

Assembled Drawing





Homogenizer Array Spacer



Single Lens System

$$\frac{1}{s_o} + \frac{1}{s_i} = \frac{1}{f}$$

f = focal length

$$M_T = -\frac{s_i}{s_o}$$

M_T = total magnification

APPENDIX B

VOYAGER XL ELITE RESOLUTION CALCULATIONS

$$\begin{aligned}
 d_a &:= 2.16 \text{ mm} & v_a &:= 7750 \text{ V} & \delta v_o &:= 500 \frac{\text{m}}{\text{s}} \\
 d_0 &:= 7.2 \text{ mm} & v &:= 25000 \text{ V} & v_n &:= 27758 \frac{\text{m}}{\text{s}} \\
 d_R &:= 857.25 \text{ mm} & y &:= \frac{v}{v_a} & \delta x &:= .1 \text{ mm} \\
 D &:= 3357.46 \text{ mm}
 \end{aligned}$$

$$y = 3.226$$

d_a - length of 1st accelerating region

d_0 - length of 2nd region

d_R - length of reflectron

D - length of field free drift region

v_a - voltage applied across 1st region

v - total voltage

y - voltage ratio

δv_o - width of initial velocity distribution

v_n - nominal velocity (calculated using

$KE = 1/2mv^2$) know, KE ("v") and mass
(5000 Da molecule)

δx - change in initial ion position

F values - dimensionless coefficients and explicit expressions for specific instrument geometry
take into account instrument geometry and operating voltages

$$f_0 := 1 + \frac{4 \cdot (d_R)}{D} + \frac{2 \cdot d_a \cdot y^{\frac{1}{2}}}{D} + \frac{2d_0}{D} \cdot \frac{y}{y-1} \cdot \left[1 - \left(\frac{1}{y^{\frac{1}{2}}} \right) \right]$$

$$f_0 = 2.026$$

$$f_1 := \frac{\frac{1 - \frac{4 \cdot d_R}{D}}{y} - \frac{2d_a \cdot y^{\frac{1}{2}}}{D} - \left(\frac{2d_0}{D} \right) \cdot \left(\frac{y}{y-1} \right) \left[\left(\frac{1}{y} \right) - \left(\frac{1}{y^{\frac{1}{2}}} \right) \right]}{2}$$

$$f_1 = -3.691 \times 10^{-3}$$

$$f_2 := \frac{\frac{3 - \frac{4 \cdot d_R}{D}}{y^2} - \left(\frac{2d_a \cdot y^{\frac{1}{2}}}{D} \right) - \left(\frac{2d_0}{D} \right) \cdot \left(\frac{y}{y-1} \right) \left[\left(\frac{1}{y^2} \right) - \left(\frac{1}{y^{\frac{1}{2}}} \right) \right]}{8}$$

$$f_2 = 0.024$$

$$f_3 := \frac{\frac{5 - \frac{4 \cdot d_R}{D}}{y^3} - \frac{2 \cdot d_a \cdot y^{\frac{1}{2}}}{D} - \left(\frac{2 \cdot d_0}{D} \right) \cdot \left(\frac{y}{y-1} \right) \cdot \left[\left(\frac{1}{y^3} \right) - \left(\frac{1}{y^{\frac{1}{2}}} \right) \right]}{16}$$

$$f_3 = 7.468 \times 10^{-3}$$

R_{s3} = spatial resolution limit

R_{v2} = velocity resolution limit

$$R_{s3} := 2 \cdot \left(\frac{f_3}{f_0} \right) \cdot \left(\frac{\delta x}{d_a} \right)^3$$

$$R_{s3} = 7.314 \times 10^{-7} \quad R_{s3}^{-1} = 1.367 \times 10^6$$

$$R_{v2} := \frac{2 \left(\frac{\delta v_o}{v_n} \right)^2 \left[f_2 \cdot \left(\frac{2d_a \cdot y}{f_l \cdot D} \right)^2 - f_l \cdot y \right]}{f_0}$$

$$R_{v2} = 1.347 \times 10^{-5} \quad R_{v2}^{-1} = 7.426 \times 10^4$$

R_{es} = Resolution limit based on both spatial and velocity spread

$$R_{es} := \left(R_{s3}^2 + R_{v2}^2 \right)^{\frac{1}{2}}$$

$$R_{es} = 1.349 \times 10^{-5} \quad R_{es}^{-1} = 7.416 \times 10^4$$

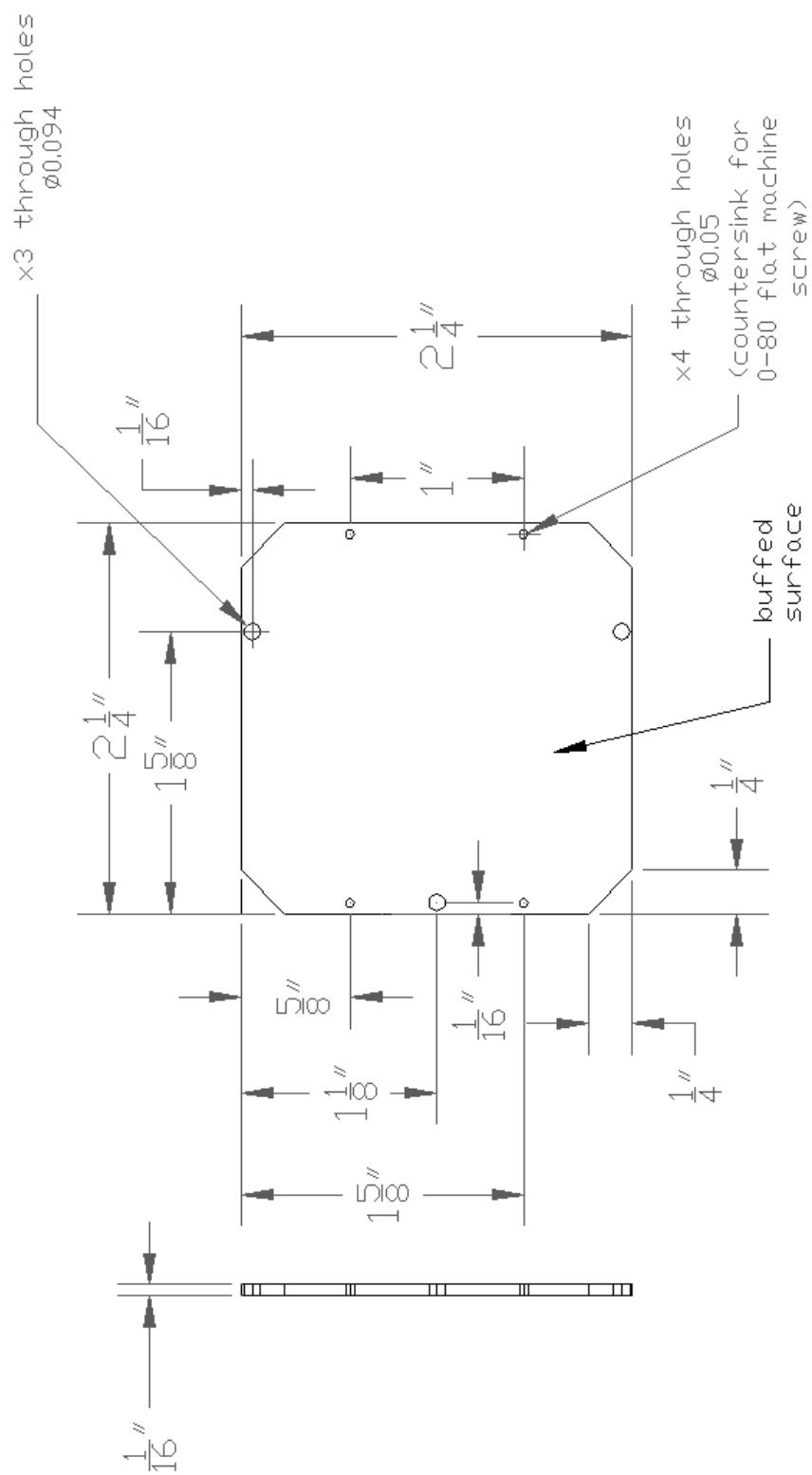
$$R_{es2} := \frac{1}{\left(R_{s3}^2 + R_{v2}^2 \right)^{\frac{1}{2}}}$$

$$R_{es2} = 7.416 \times 10^4$$

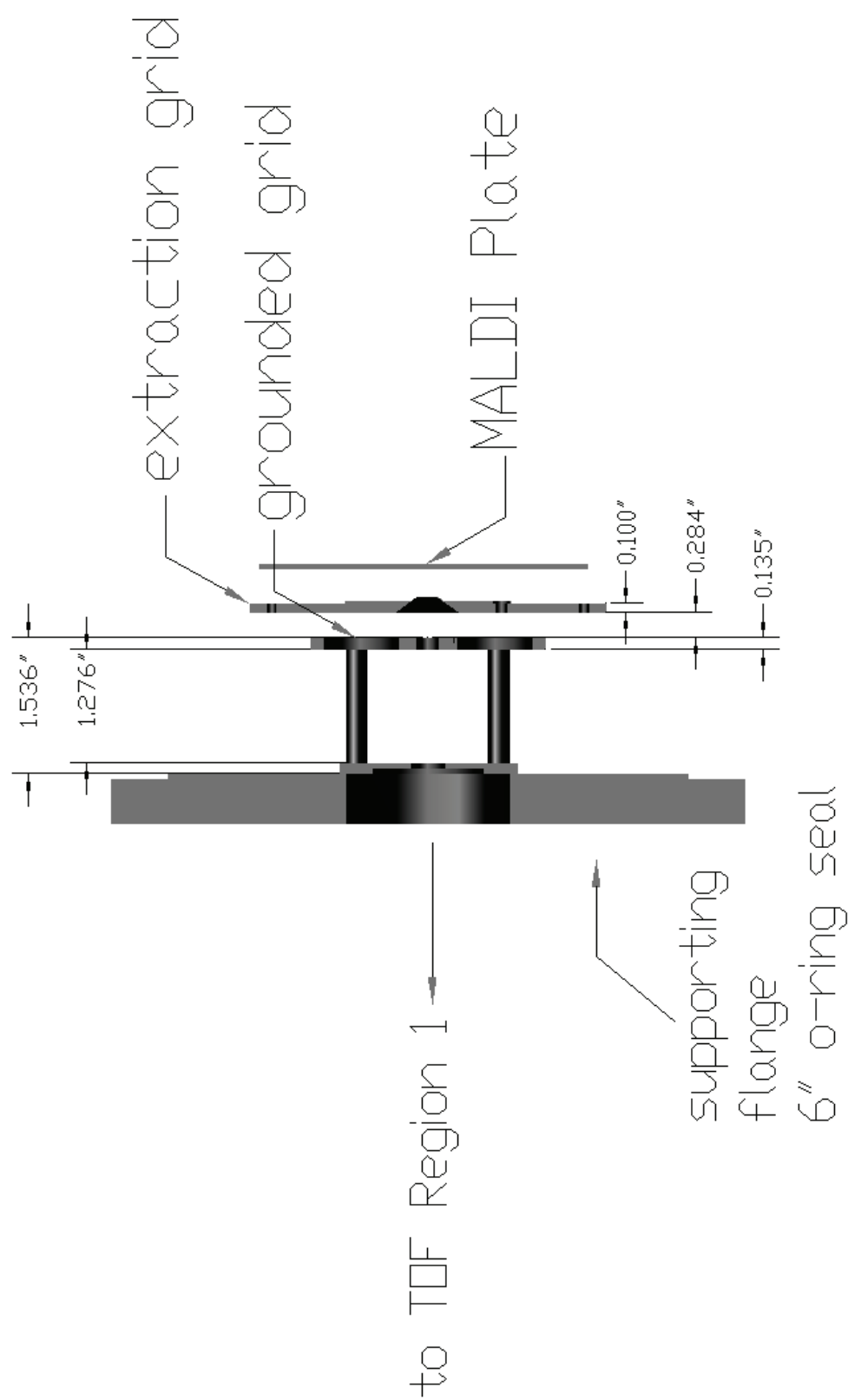
APPENDIX C

CURRENT VOYAGER ELITE XL INSTRUMENT CONFIGURATION

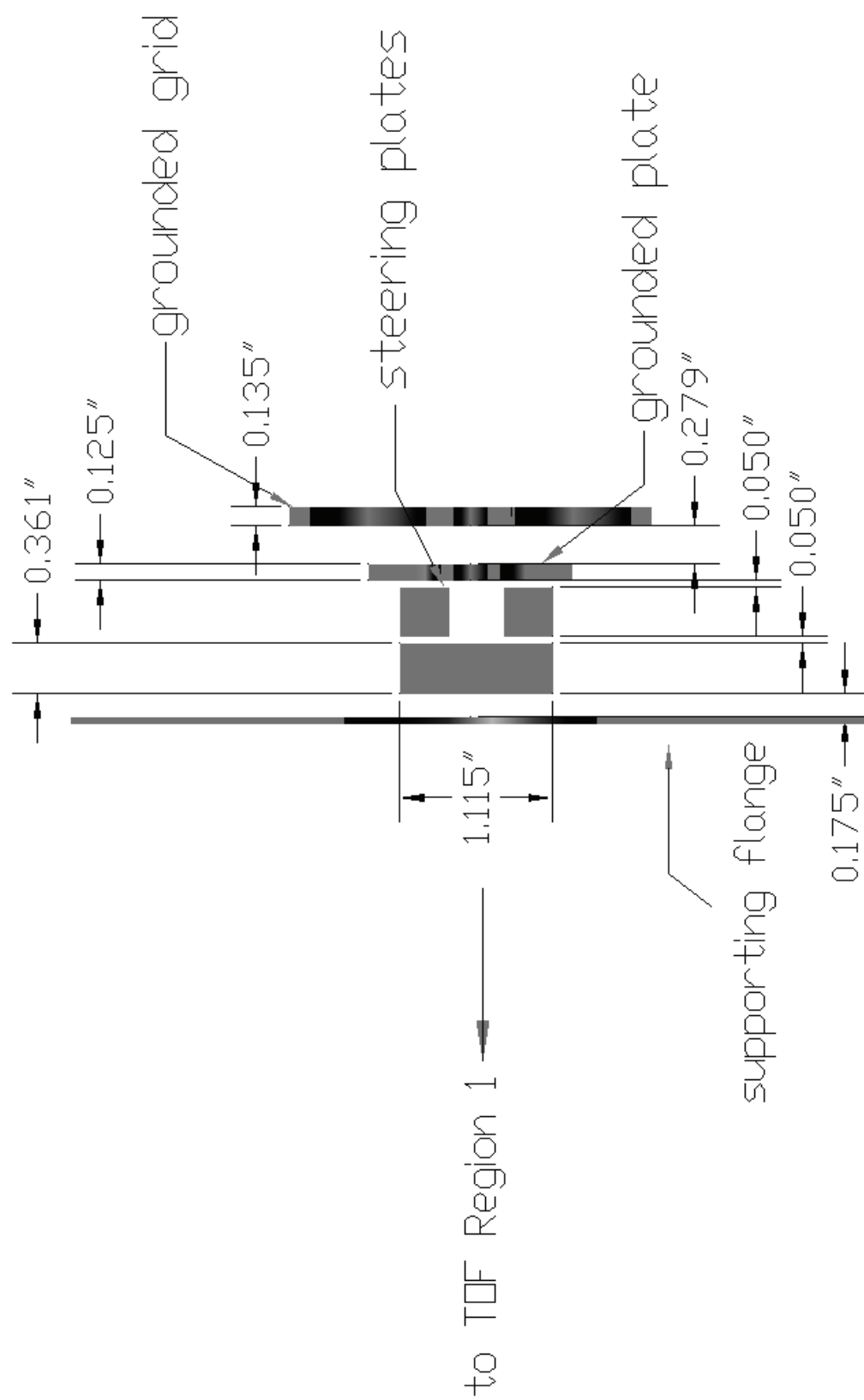
DRAWING	Page
MALDI Plate	137
Source Region Ion Optics	138
Ion Steering Lens Assembly	139
Einzel Lens Assembly	140
Time-Of-Flight	141
Reflectron.....	145
Reflectron Detector Grid Plate.....	147
2" eV part (Kimball Physics)	148
Reflectron Detector Mount Plate.....	149
Assembled Instrument.....	150



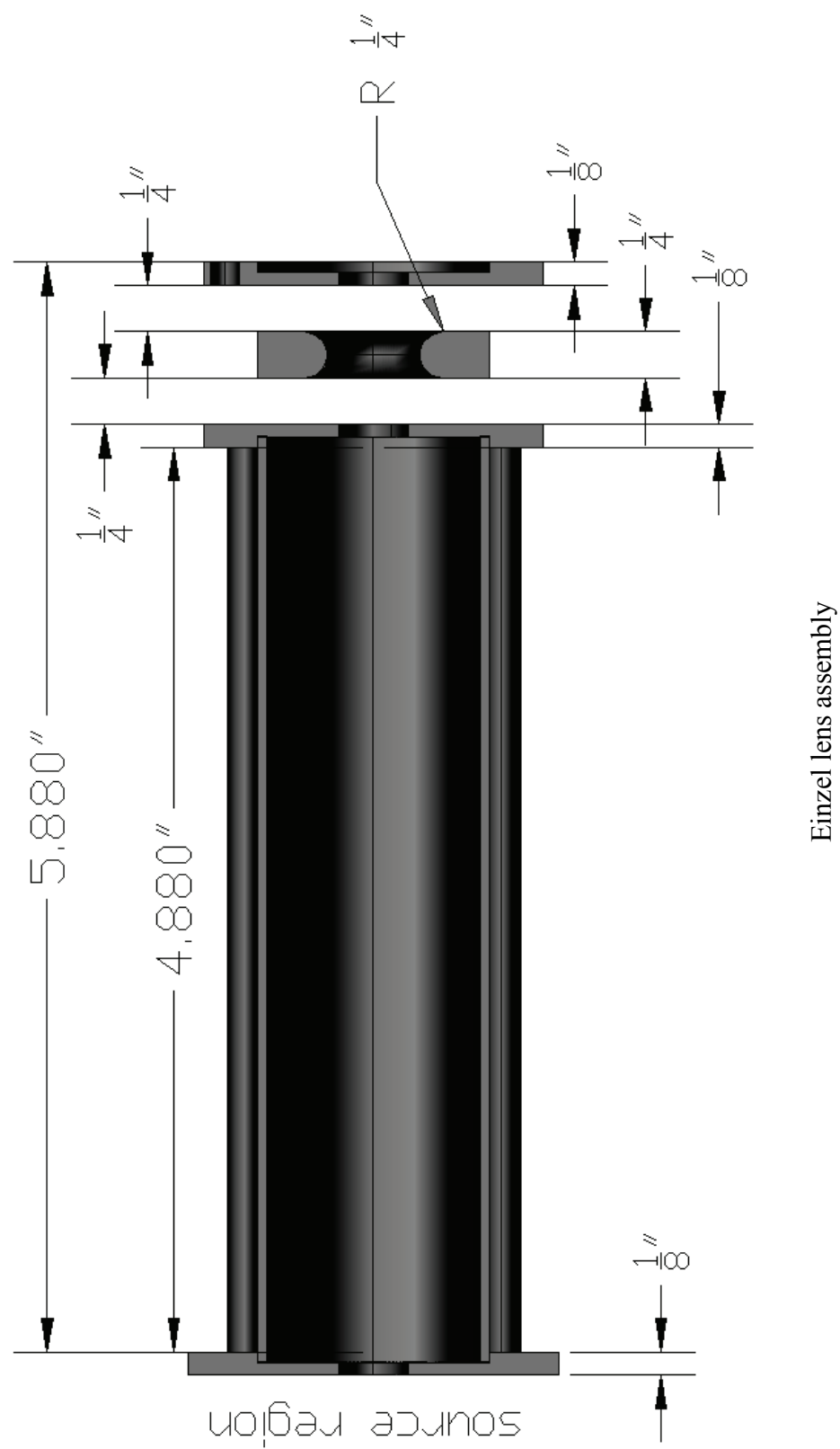
MALDI plate (Applied Biosystem Instruments – Voyager Elite XL, Voyager STR, Benchtop linear, and 4700 Proteomics Analyzer)



Source Region Ion Optics

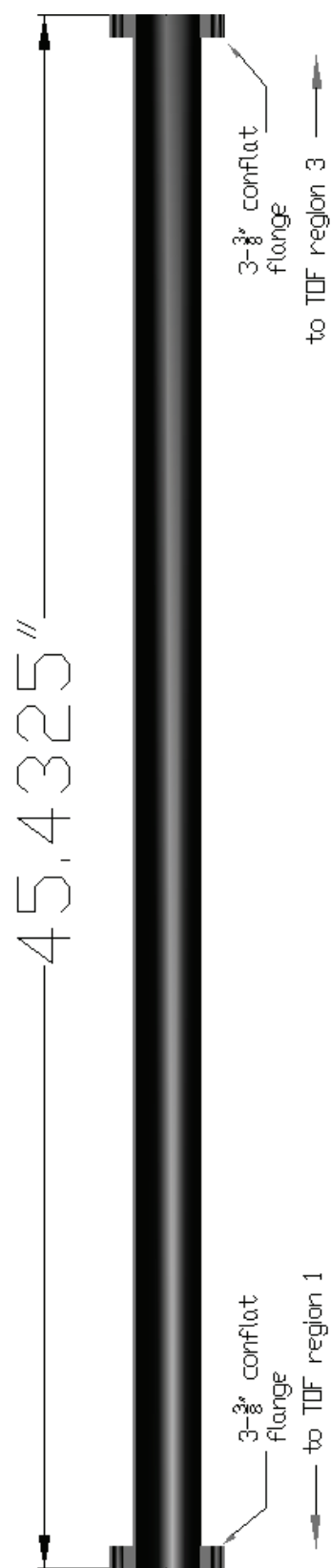


Ion Steering Lens Assembly

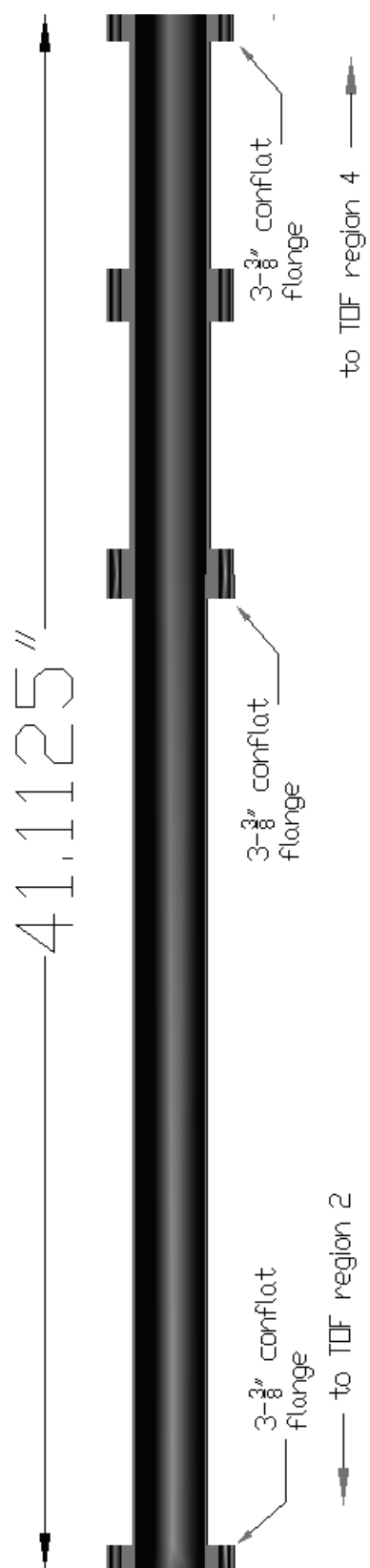




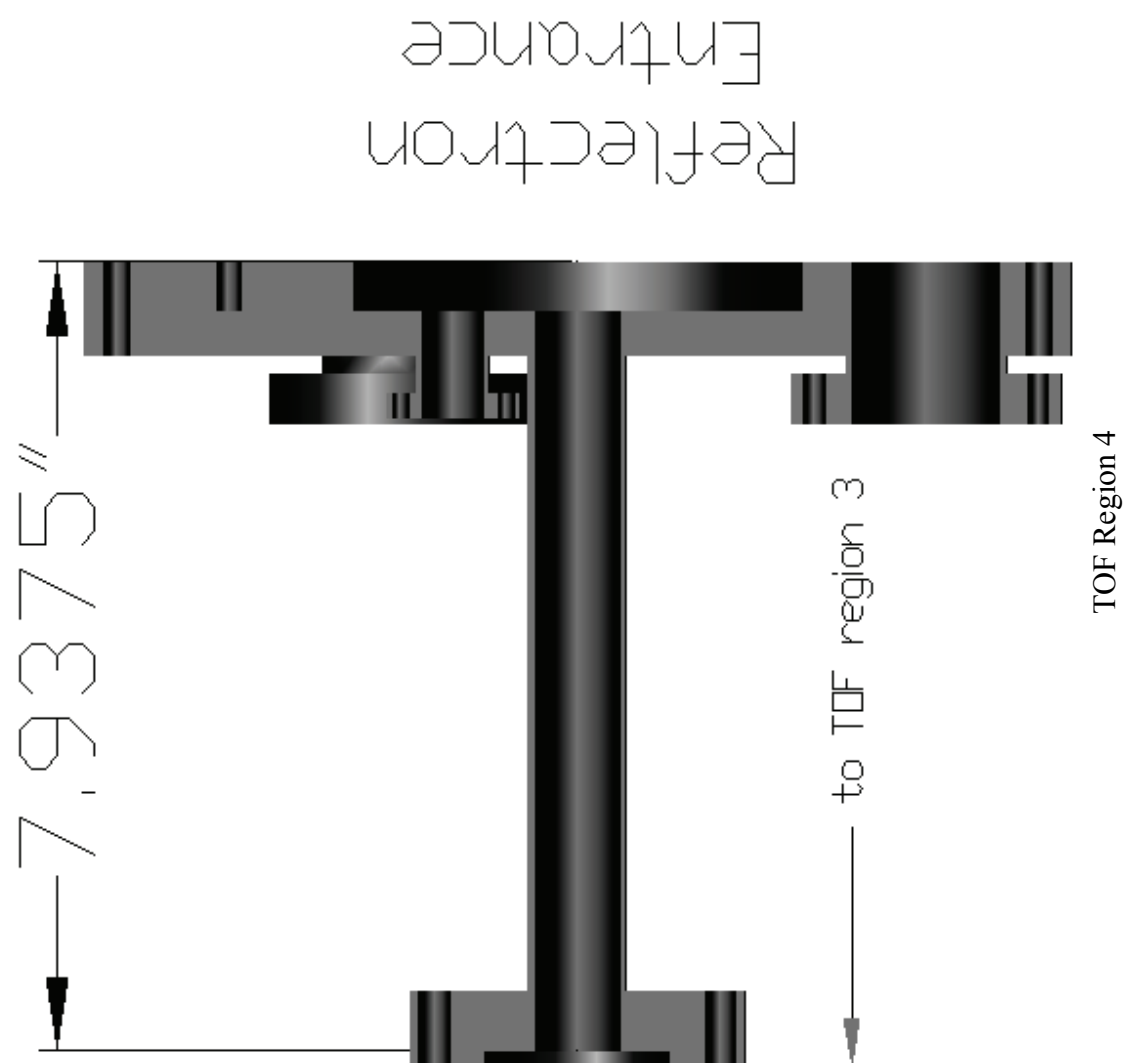
TOF Region 1

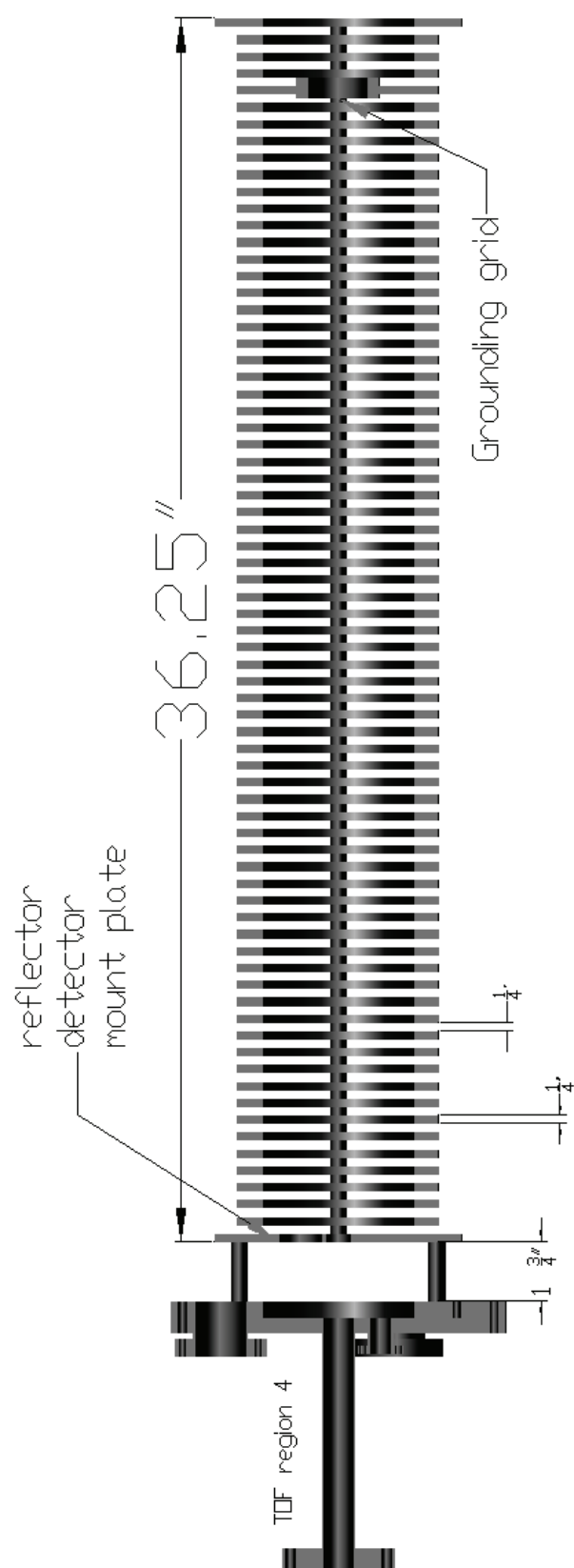


TOF Region 2

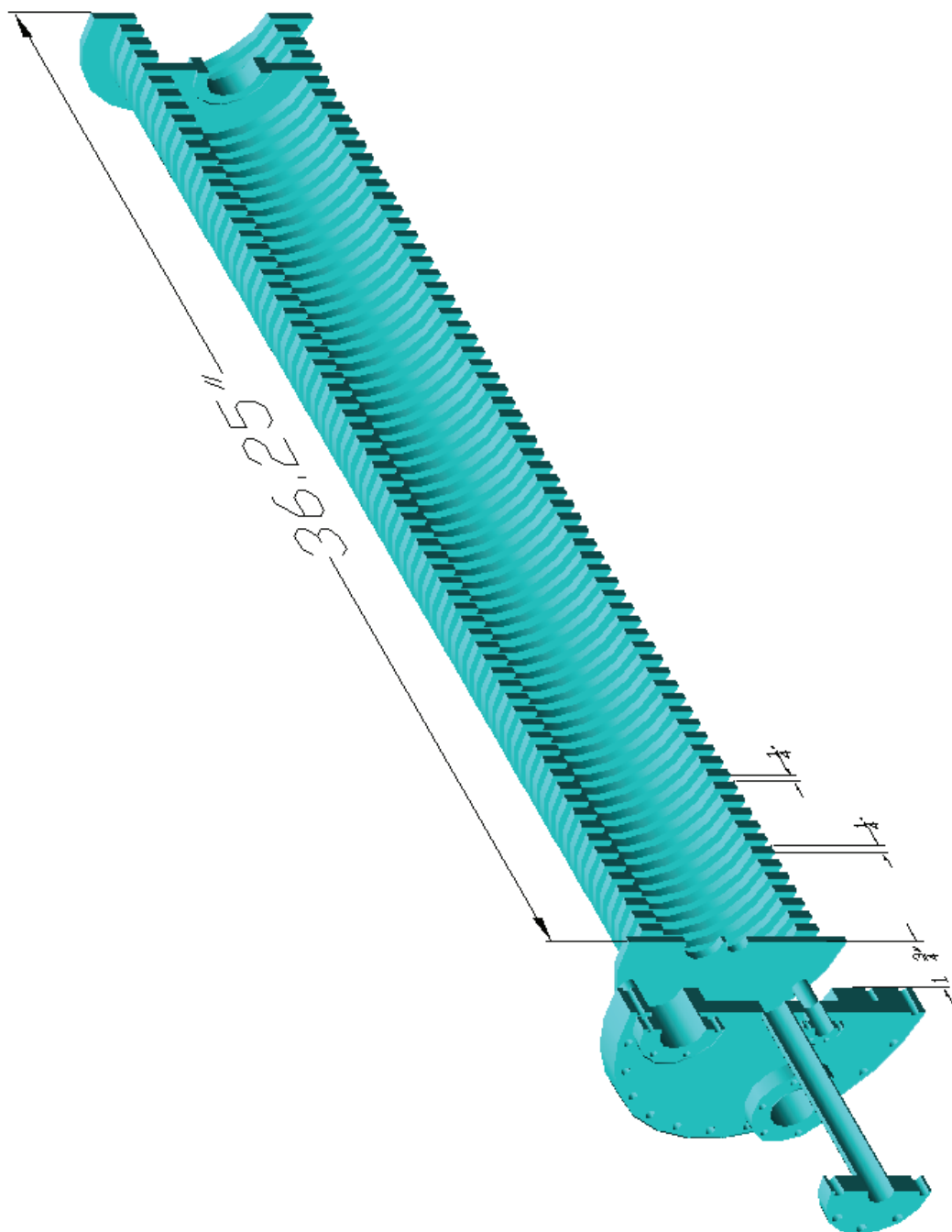


TOF Region 3

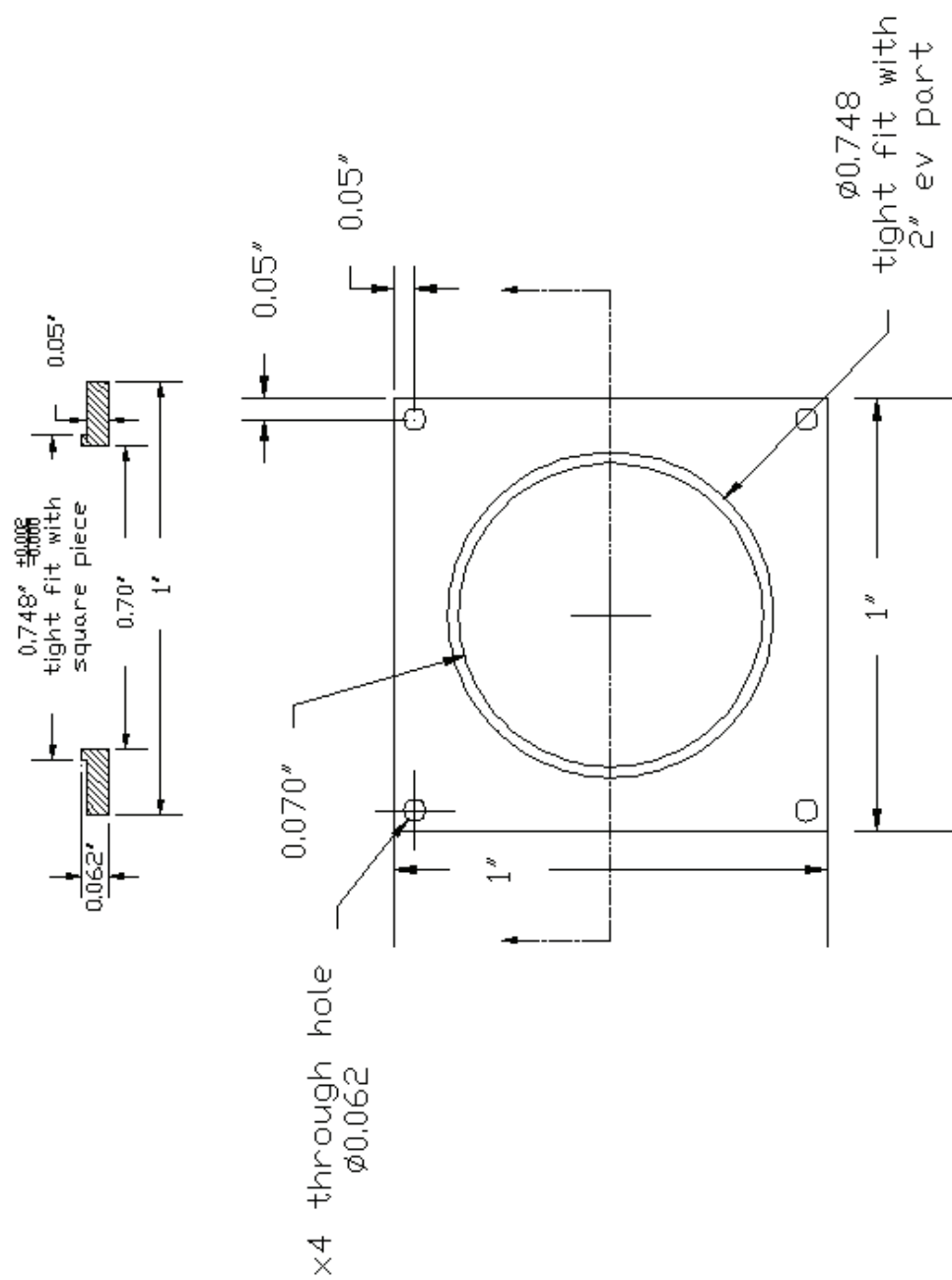




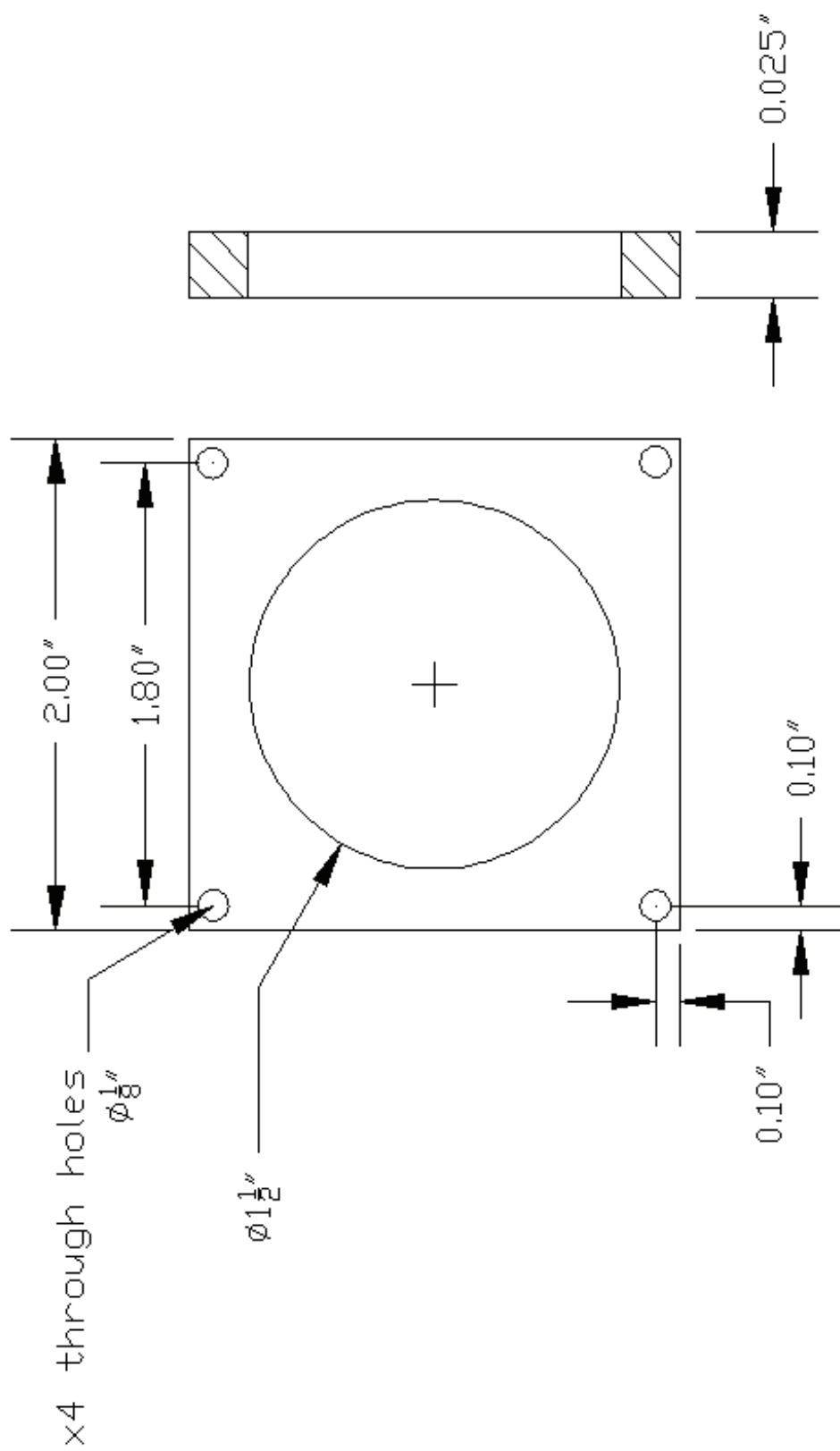
Reflectron



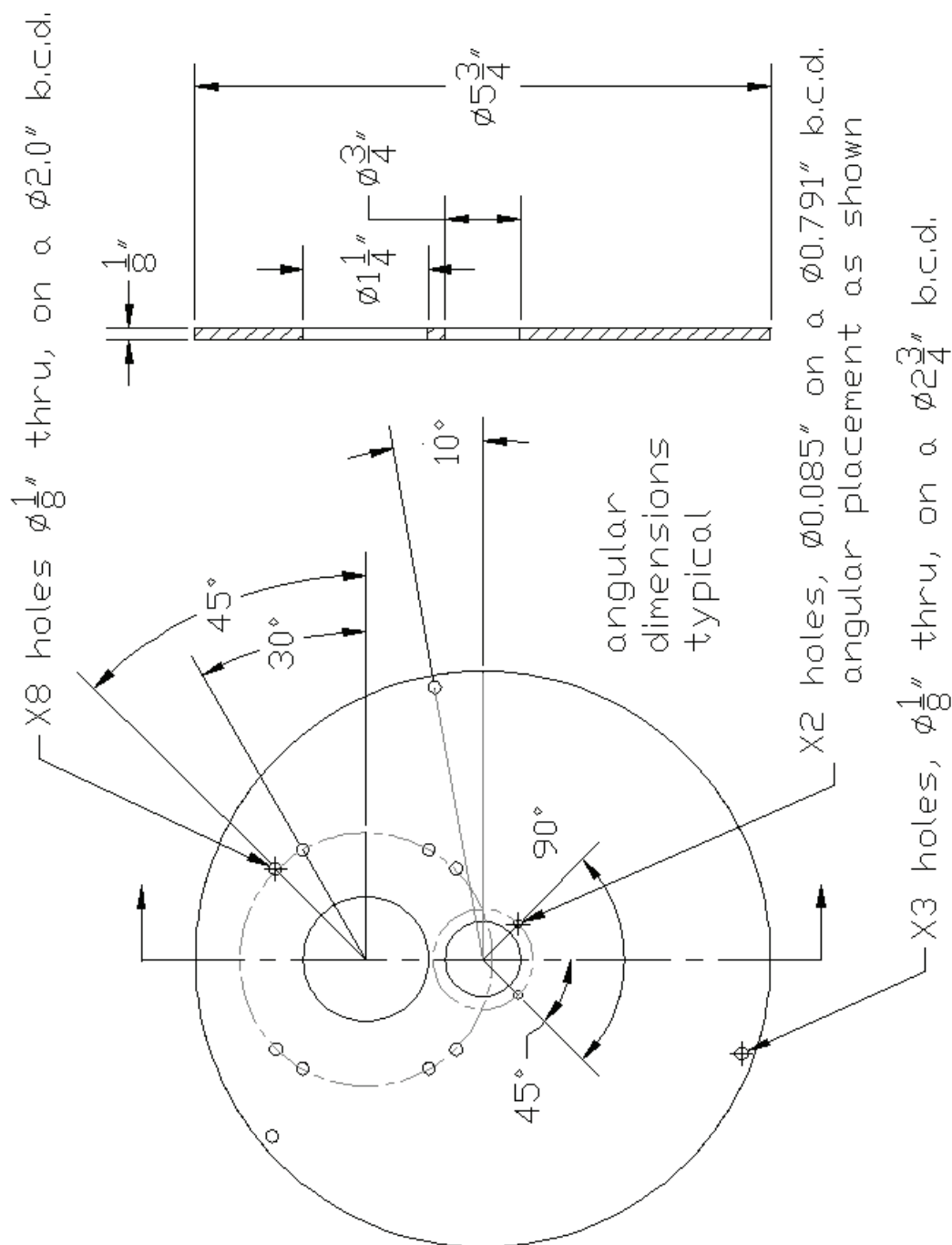
Reflectron (conceptual cutaway view)



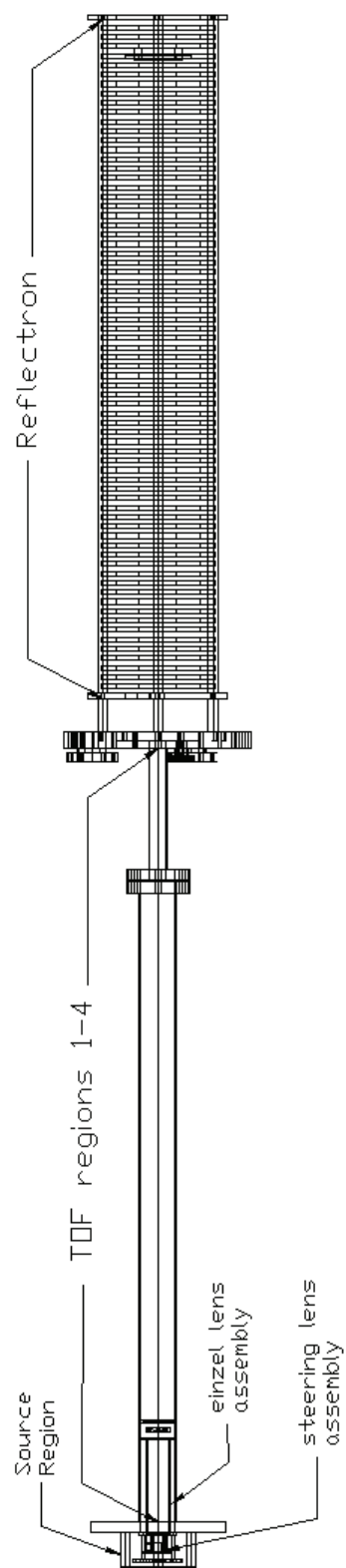
Reflectron Detector Grid Plate



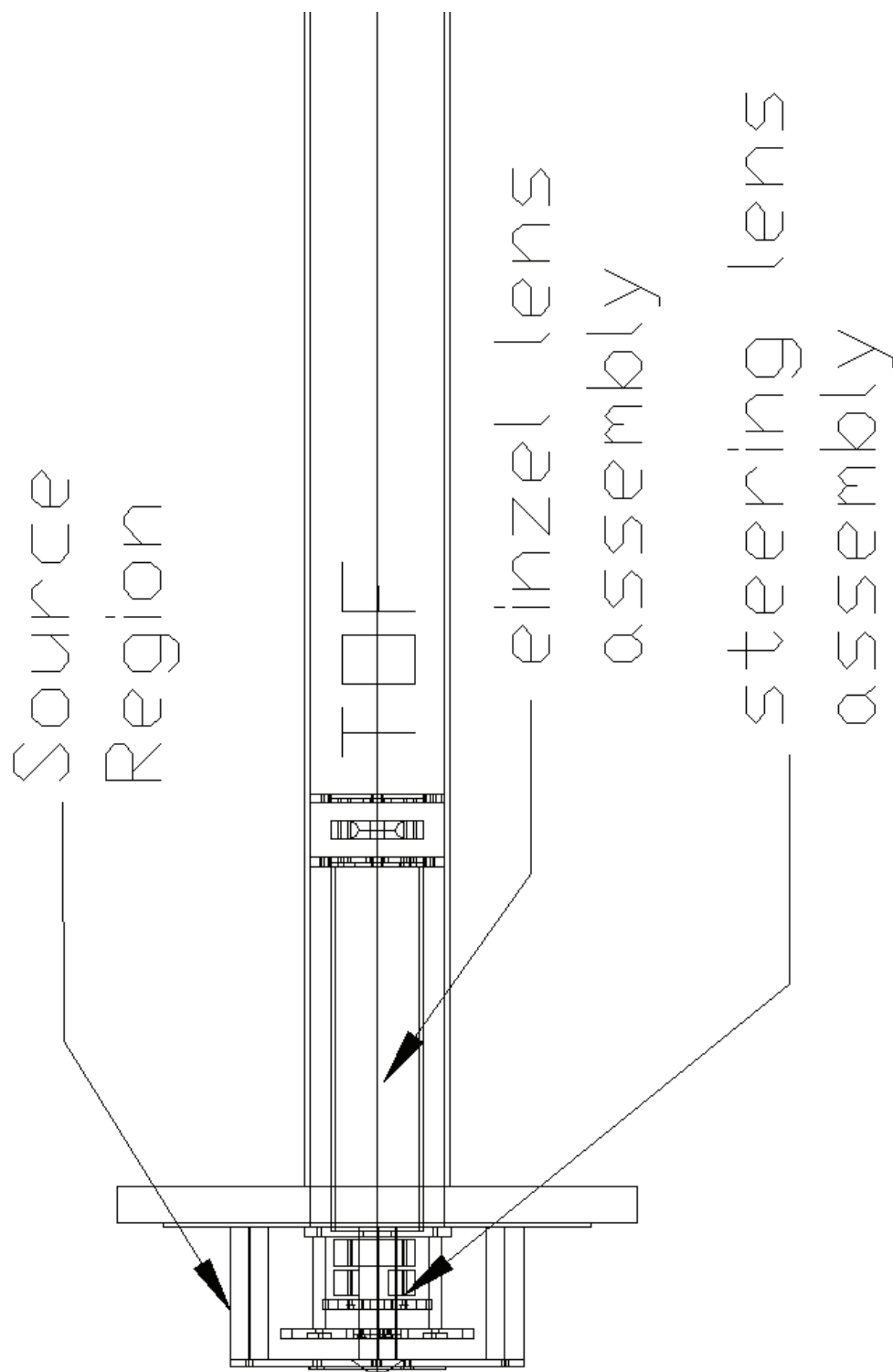
2" eV part (Kimball Physics)



Reflectron Detector Mount Plate



Assembled Voyager Elite XL Drawing



Assembled Voyager Elite XL Drawing
(zoomed in view of source and optics)

VITA

Stacy Dawn Sherrod

Department of Chemistry
Texas A&M University, MS 3255
College Station, TX 77843-3255
979-862-7159

EDUCATION

Ph.D. in Chemistry, December 2008, Magna Cum Laude 3.82/4.00
Department of Chemistry, Texas A&M University, College Station, Texas
Research Director: Professor David H. Russell

B.S. in Chemistry, May 2003, Magna Cum Laude 3.83/4.00
Department of Chemistry, Sam Houston State University, Huntsville, Texas

AWARDS AND HONORS

2008	Sharon Dabney Memorial Scholarship Recipient (Outstanding graduate student award displaying excellence academically and through service to the Department of Chemistry at Texas A&M University)
2007	Richard A. Schaeffer Memorial Fund Travel Award Recipient
2005	Phi Lambda Upsilon National Honor Society
2004	Ford Foundation Diversity Fellowship Awardee (Honorable Mention)

SELECTED PUBLICATIONS

Sherrod, S. D.; Castellana, E. T.; McLean, J. A.; Russell, D. H. *Int. J. Mass Spectrom. Ion Physics* **2007**, 262, 256-262.

Sherrod, S. D.; Diaz, A. J.; Russell, W. K.; Cremer, P. S.; Russell, D. H. *Anal. Chem.* **2008**, 80, 6796-6799.

Castellana, E. T.; Sherrod, S. D.; Russell, D. H. *Journal of the Association for Laboratory Automation*, accepted **2008**.